Insights into Acute Muscle Strain Injury Obtained with In Vivo Imaging and Finite Element Modeling

---

A Dissertation
Presented to
the faculty of the School of Engineering and Applied Science
University of Virginia

---

in partial fulfillment
of the requirements for the degree
Doctor of Philosophy
(Mechanical & Aerospace Engineering)

by

Niccolo Fiorentino

May

2013

APPROVAL SHEET

The dissertation
is submitted in partial fulfillment of the requirements
for the degree of
Doctor of Philosophy

Niccolo Fiorentino

AUTHOR

The dissertation has been read and approved by the examining committee:

Silvia Blemker

Advisor

Richard Kent

Hilary Bart-Smith

Frederick Epstein

Darryl Thelen

Accepted for the School of Engineering and Applied Science:

Dean, School of Engineering and Applied Science

May
2013

Abstract

Acute muscle strain injury is a prevalent and significant problem for professional, collegiate and recreational athletes, particularly in sports that involve high-speed running. Acute muscle strain injury is characterized by the sudden onset of intense pain caused by tearing of muscle fibers. Injury requires weeks to months away from sport, and previous injury increases the chance of future injury. Despite the established frequency and consequences of strain injury, decades of scientific inquiry have provided relatively little insight into the factors that cause tissue injury and what makes an individual more susceptible to injury. The goals of this work were to use *in vivo* imaging for measuring local tissue strains during dynamic knee joint motion and to use finite element modeling for predicting local tissue strain while running at high speeds.

The hamstring muscles in the posterior thigh suffer injury most often, because the hamstring muscles simultaneously lengthen and actively generate force during the late swing phase of running gait. Of the three hamstrings muscles, the biceps femoris long head (BFlh) is injured most frequently. We imaged the BFlh of a group of healthy subjects without a history of injury. Static MR images were used to measure the width of the proximal aponeurosis, which is where muscle fibers originate and muscle tissue is frequently injured. Dynamic MR images acquired during dynamic knee extension provided spatially varying 1^{st} principal strain measurements. We found that local tissue strain was higher when the BFlh was actively generating force and lengthening versus passively lengthening, which suggests that high-localized strain is the acute strain injury mechanism. In addition, we found that local tissue strain was higher for subjects with a

relatively narrower proximal aponeurosis, demonstrating that musculotendon dimensions can influence an individual's strain injury susceptibility.

To study the BFlh while running at high speeds, a series of finite element (FE) models were constructed based on the musculotendon dimensions of track and field athletes at the University of Virginia. In addition, to verify model predictions with *in vivo* measurements, a FE model was generated based on the group of healthy subjects in the previous study, and simulations were performed of active and passive lengthening. Simulations of sprinting were based on the output of forward dynamic simulations, which provided muscle activation and muscle-tendon length change during the swing phase of sprinting. Muscle activation and muscle-tendon length change were applied to the muscle and distal end of BFlh FE mesh, respectively. Model simulations of increasing sprinting speed (70%, 85% and 100% of maximum speed) showed that local muscle tissue strain increases at faster sprinting speeds, which provides an explanation for why muscles are injured more often during high-speed sports. To assess the influence of musculotendon variability on strain injury susceptibility during sprinting, additional model simulations varied the proximal aponeurosis width, muscle width and proximal aponeurosis length over a physiological range. Simulation results showed that the structures' dimensions influence local muscle tissue strain magnitude during sprinting.

By measuring local tissue strain during active lengthening and predicting strain while sprinting, the results of this dissertation make significant contributions to our understanding of acute strain injury. Insights into the acute strain injury mechanism and the factors that contribute to strain injury susceptibility have the potential to help the development of training and rehabilitation programs aimed at reducing injury incidence.

Acknowledgments

I have many people to acknowledge and thank for helping me along the demanding and long journey throughout graduate school. Without them I would not have enjoyed the successes that I did.

First I must express my sincerest appreciation for the efforts of my advisor, Silvia Blemker, who taught me so much and made me the scientist I am today. She showed me how to tackle challenging research questions with vigor and produce beautiful results. She has shown me how to turn roadblocks into successes, and I am forever grateful for her unwavering support and patience throughout the years.

I met Silvia after a visit she took to the NIH, where I was working for Elliot McVeigh. I send many thanks to Elliot for inviting Silvia back to the NIH for more experiments. I also thank him for being one of the greatest scientists and coolest people I have ever met. While I'm thanking PIs from my past, I must thank BJ Fregly for exposing me to biomechanics and how much fun it can be to study. Without his dedication to teaching and tutelage, I would not have eventually made my way into the multi-scale muscle mechanics lab at UVa.

I also have many to thank in the M3 lab who have been a great source of inspiration over the years. I thank Mike Rehorn for the many productive discussions we shared over the years and for having a good time in the lab no matter how late we were there. I also thank Bahar Sharafi for her willingness to tutor me in computational modeling and for cajoling me to take biomechanics breaks throughout the day. Thank you to Geoff Handsfield as well for our many long discussions about biomechanics and for sharing his knowledge about, well, everything. I'm also grateful to Shawn Russell for

our shared addiction to coffee breaks and to Hon Fai Choi for being the only one who's more rigorous in his scientific approach than me. I also thank the relative newcomers to the M3, Katie Pellend and Josh "party boy" Inouye, for the fun breaks from lab work and for pushing the envelope of my knowledge of computational modeling.

I am grateful to many others at UVA who have contributed to my successes over the years. I extend many thanks to Fred Epstein for providing the DENSE imaging sequence and to Xiadong Zhong for spending so much of his time training me on the MR scanner. I also acknowledge the image analysis assistance provided by Scott Acton and Drew Gilliam, who was always extremely fast at incorporating changes to the DENSEanalysis software. I appreciate the efforts of our collaborators in the athletic training department, most notably Natalie Kramer, Collin Herb and Jay Hertel, who were instrumental in recruiting track and field athletes, collecting torque data, and getting the athletes to actually show up for MR experiments.

Our collaborators at the University of Wisconsin-Madison are deserving of much praise as well, especially Darryl Thelen. Darryl has been like a second advisor to me, providing constructive feedback at every step and talking biomechanics with me whenever I asked. I am also grateful for the input of Amy Silder (a.k.a. Dr. Amy), who was my partner in crime for a few years and gave me lots of good advice while walking her turtle. I'm also grateful for the data that Liz Chumanov provided on the athletes at UW-Madison, without which the simulations of sprinting would not be possible.

I'd also like to express my thanks for the efforts of the researchers in the Mechanical & Aerospace department. Hilary Bart-Smith and Richard Kent have always been willing to discuss my research with me and share their immense knowledge of

mechanics and biomechanics. I am also indebted to our friends at the CAB, especially Jeff Crandall, who went out of his way to introduce me to a potential post-doc opportunity. While I am mentioning friends at the CAB, I have to thank my friend Joe Ash, who's been the best roommate I've ever had. He's been one of my best friends, and I'll always be thankful for the fun memories we've shared throughout the years.

I also want to thank all my friends in Charlottesville for being there for me, giving me fun distractions from lab work and providing kind words of sympathy when I needed them. I am especially grateful for Allison Spain, who has been the best partner I could have ever hoped for over the last year-ish. I don't think I could have finished this dissertation without her. She has been a constant source of hope, and, without question, the best partner I have ever known.

My family is deserving of many thanks as well. I thank my sister and brother, Angela and Anthony, whose successes and words of encouragement have helped me persevere. I thank my father who instilled in me the drive and value of hard work that has gotten me to where I am today. I thank my mother who has been the motivation behind my affinity for science since I was a child. Her unending love and support has allowed me to accomplish so much over the years. She has been and always will be my inspiration, and I owe her infinitely for making me the man I am today.

I conclude by acknowledging the funding sources that provided the means for the work in this dissertation: NIH R01 AR056201, Mechanical & Aerospace Engineering Department, National Science Foundation Graduate Research Fellowship and Achievement Rewards for College Scientists.

Table of Contents

Figures

Tables

Abbreviations & Symbols

α	Muscle activation
φ	Along-fiber shear
ϕ	Cross-fiber shear
Φ	Strain energy density function
λ	Along-fiber stretch
λ^*	Along-fiber stretch at which the stress-strain becomes linear
λofl	Along-fiber stretch corresponding to optimal fiber length
σ_{max}	Peak isometric stress
Ao	Exponential shear modulus
AP	Anterior-posterior
BFlh	Biceps femoris long head
C	Right Cauchy-Green strain tensor
DENSE	Displacement Encoding with Stimulated Echoes
E	Lagrangian strain tensor
F	Deformation gradient
I	Identity tensor
FC	Foot contact
FE	Finite element
Gφ	Along-fiber shear modulus
Gaf	Along-fiber shear modulus
Gϕ	Cross-fiber shear modulus

Gcf	Cross-fiber shear modulus
J	Volumetric strain
ke	Encoding frequency
K	Bulk modulus
ML	Medial-lateral
MR	Magnetic Resonance
MTJ	Myotendinous junction
MS	Mid-swing
MTU	Muscle-tendon unit
Navg	Number of averages
NSAID	Non-steriodal anti-inflammatory drugs
P1	Along-fiber extension multiplicative modulus
P2	Along-fiber extension exponential modulus
RICE	Rest, ice, compression and elevation
ROI	Region of interest
S	2^{nd} Piola-Kirchhoff stress tensor
SD	Standard deviation
TE	Echo time
TR	Repetition time
W	Strain energy density function
Wvol	Volumetric contribution to the strain energy density function
Wdev	Deviatoric contribution to the strain energy density function
W_λ	Strain energy due to along-fiber stretch

Chapter 1 Introduction

Strains and sprains have been found to be the most frequent sports-related injury diagnosis in the United States (Conn et al., 2003), with muscle strain injuries accounting for up to 30% of sports medicine practice (Garrett, 1996). Cost estimates due to acute strain injury have been as high as £75 million for a single English Premier League soccer season and approximately 1.2% of the total salary cap in Australian Rules Football (Woods et al., 2002). Strain injuries remain a pervasive problem at the professional (Elliott et al., 2011), collegiate (Marshall et al., 2007) and recreational (Hootman et al., 2002) levels. Strain injuries are particularly common in sports that involve high-speed running, such as track and field (Bennell and Crossley, 1996), rugby (Brooks et al., 2005), soccer (Ekstrand et al., 2009) and football (Feeley et al., 2008). Acute strain injury is characterized by the tearing of muscle fibers (Jarvinen et al., 2005), which leads to severe pain and subsequent long periods of reduced activity and time away from sport (Brooks et al., 2006). Furthermore, acute strain injury is not only a common problem for athletes but also a persistent one, given that previous injury is the most reliable predictor of future injury (Foreman et al., 2006). Despite the established prevelance, severity and persistence of acute strain injury in sports, factors that contribute to injury and predispose an individual to injury remain poorly understood.

Previous research has focused on associating hamstring strain injury and performance on a functional test, such as hamstring strength (Orchard et al., 1997), quadriceps-to-hamstrings strength ratio (Croisier et al., 2008), flexibility (Bennell et al., 1999) and neuromuscular control (Cameron et al., 2003). Non-strength measures, such as age (Verrall et al., 2001), ethnic origin (Woods et al., 2004), inadequate warmup

(Worrell, 1994), and fatigue (Croisier, 2004), have been suggested as injury predictors as well. Associating injury with functional and non-functional measures has produced mixed results at best, though one factor has garnered consistent support in the literature as a predictor of future injury—previous injury (Foreman et al., 2006). Moreover, high re-injury rates are excaberated by the fact that re-injuries are frequently more severe and require more time away from sport than the initial injury (Brooks et al., 2006). The added risk after inital injury and the increased time away from sport intensify the need to understand what makes an individual more susceptible to acute strain injury, because strain injury is likely a confluence of factors—functional and non-functional—instead of a stand-alone cause (Bahr and Holme, 2003).

Animal models of strain injury have provided a basis for our understanding of acute strain injury in humans. Experiments in animal tissue have shown that muscle is most susceptible to injury during eccentric contractions, when the muscle is active and lengthening (Garrett et al., 1987; Lieber et al., 1991), and that the amount of strain experienced by muscle is proportional to the extent of injury (Brooks and Faulkner, 2001; Lieber and Friden, 1993). While animal models have provided a foundation for our understanding of muscle strain injury, it is difficult to relate experiments on the length scale of animal models to the *in vivo* behavior of a human's muscle-tendon unit. Moreover, because strain measurements are generally made at the whole fiber, fascicle or muscle-tendon unit level, strain measurements in animal experiments lack the spatial resolution to investigate regions of high-localized strain.

In humans, previous research has consistently shown that athletes suffer acute strain injuries in their hamstrings muscles, which are located on the back of the thigh. Of

the three hamstring muscles, the biceps femoris long (BFlh) muscle suffers injury most often (De Smet and Best, 2000; Koulouris and Connell, 2003; Verrall et al., 2003). Hamstring strain injury is known to commonly recur after returning to competition, with re-injury rates reported as high as 31% within one year (Orchard and Best, 2002). Injury typically occurs at the myotendinous junction (MTJ) (Noonan and Garrett, 1992), where fibers originate or insert along the muscle's aponeurosis or tendon. In the oft-injured BFlh, magnetic resonance (MR) studies have confirmed that injury is most often observed along the proximal MTJ (Askling et al., 2007; Silder et al., 2008). Moreover, in agreement with animal models, injury in humans has been observed during eccentric contraction of the BFlh muscle (Heiderscheit et al., 2005; Schache et al., 2009), which occurs as a result of the hamstring muscles functioning to slow the lower leg down during the second half of the swing phase of high-speed running.

Even though the location (proximal myotendinous junction), timing (late swing phase of running gait) and circumstances (eccentric contraction) of hamstring strain injury have been established, many important questions remain regarding the causation and contributory factors to strain injury. For example, why is the BFlh muscle injured during eccentric contraction? Why does running at high speeds make the BFlh muscle more susceptible to injury? What about the BFlh muscle makes it so susceptible to injury? Answering these questions will make significant contributions to our understanding of acute strain injury, and the results presented within this dissertation will likely have a long-term impact in reducing the number of acute strain injuries.

1.1 Focus of the dissertation

The focus of the research presented in this dissertation is to investigate the contributory factors to strain injury using advanced MRI experimentation and FE model simulations. Dynamic MR and FE modeling techniques were developed to study the tissue-level behavior of muscle and test hypotheses regarding strain injury in human subjects. Imaging and modeling methods were used to investigate the local effects of muscle activation and whether anatomical factors have an influence on strain injury susceptibility. To test the hypotheses that muscle activation and musculotendon architecture can influence local muscle tissue strains, a group of healthy subjects were imaged during dynamic knee motion to measure strains *in vivo*. Strains were compared *i*) during active lengthening and during passive motion and *ii*) for subjects with a narrow proximal aponeurosis width to those with a wide aponeurosis.

Finite element model simulations were used to study the behavior of the BFlh during sprinting, because the amount of muscle-tendon length change and muscle activation encountered during high-speed sports cannot be studied with dynamic MR imaging. The musculotendon dimensions of UVa track and field athletes were measured on high-resolution MR images and were used to generate FE meshes. Finite element simulation boundary conditions were derived from forward dynamic simulations of sprinting. Simulations of sprinting were performed at increasing speed, including 70%, 85% and 100% of maximum speed, to investigate why injuries occur while running at high-speeds. In addition, a series of FE meshes with varying musculotendon dimensions were generated for the BFlh to explore the roles that architecture and physiological variability play in injury susceptibility.

1.2 Significance of this research

Recent advances in MRI technology have provided a means to reach insights into *in vivo* muscle anatomy, structure and function that were previously unattainable with noninvasive methodologies. Assessment of musculoskeletal anatomy was generally made with cadavers (An et al., 2010; Kellis et al., 2010; Ward et al., 2009; Woodley and Mercer, 2005), which, unfortunately, generally represent an older and atrophied population. With MRI, however, we can noninvasively answer clinically relevant questions about a wide range of populations, including those that are young and athletic. In the research presented here, we measured local muscle tissue strain during dynamic knee motion in a healthy population, which has rarely been done in skeletal muscle and even less so in the BFlh muscle. In addition, we used high-resolution *in vivo* MR imaging to measure BFlh musculotendon dimensions, which, up to this point, has only been reported for cadavers or on a very limited basis *in vivo*. To gain insights into the deformation of muscle tissue when *in vivo* imaging is not yet possible, we ran FE model simulations during the swing phase of sprinting gait, when the BFlh suffers injury most often. The simulations presented in this dissertation are the first to describe local tissue deformation in the oft-injured BFlh during sprinting, and the results begin to uncover why muscle suffers injury during high-speed running and what architectural characteristics make the BFlh so susceptible to injury.

Current injury prevention programs, diagnostic practices, rehabilitation strategies and return-to-sport criteria are based on empirical or anecdotal data and lack a strong scientific basis (Heiderscheit et al., 2010). With a better understanding of the anatomical and functional factors that increase strain injury susceptibility, coaches, team doctors and

trainers will be better equipped to identify athletes at-risk for a strain injury and select them for specialized training. Moreover, by knowing more about what contributes to an acute strain injury, physicians can make more informed diagnoses and design treatment protocols that are appropriate for the sustained injury. Lastly, given that injury alters the dimension of injured muscle-tendon units (Silder et al., 2008), understanding the effects of musculotendon variability during sprinting will provide clinicians with a better basis for prescribing rehabilitation programs and help clinicians judge when an athlete is ready to return to sport without unnecessarily risking re-injury.

In addition to the clinical significance of the research presented in this dissertation, the results of this work will have significant scientific contributions to our knowledge of muscle behavior. We will add to the understanding of muscle function by publishing tissue displacement and strain results from measurements made *in vivo* and noninvasively (Fiorentino et al., 2012). Moreover, decades of research in strain injury used animal models of injury and speculated the applications to human function, whereas the results presented here are exclusively for human subjects. Imaging data also serve as *in vivo* inputs into computational models, whose output contributes to the understanding of the connections between musculotendon morphology and strain injury susceptibility. Furthermore, while we study the BFlh because it is injured most often, the insights gained from our imaging results and model simulations are applicable to every muscle in the body. In general, the combination of advanced *in vivo* imaging and computational modeling techniques yields new and exciting insights into the causation and influential factors of strain injury susceptibility.

1.3 Overview of the dissertation

The following five chapters contain the pertinent background in the field of acute strain injury, the *in vivo* imaging experiments and computational model simulations in the BFlh, and a synthesis of the work with a look forward to future experiments and model simulations. Chapter 2 lays out the background for studying acute muscle strain injury, including pertinent previous research in the field, imaging methods to study muscle injury *in vivo*, and finite element modeling of musculoskeletal tissue. Chapters 3 through 5 are self-contained manuscripts. Chapter 3 describes the method for measuring local muscle tissue strains in the BFlh and reports comparisons between active and passive lengthening and between varying musculotendon dimensions. This work has been published in the Journal of Biomechanics (Fiorentino et al., 2012). Chapter 4 describes the process for finite element model simulations of sprinting at increasing speeds. This work was submitted to the Journal of Medicine and Science in Sports and Exercise (Fiorentino and Blemker, 2013). Chapter 5 reports the variability in BFlh musculotendon dimensions for track and field athletes and demonstrates the importance of the BFlh's architecture on strain injury susceptibility. This work will be submitted to the Journal of Biomechanics prior to the end of the spring semester. In conclusion, Chapter 6 synthesizes the results in Chapters 3 through 5, discusses the contributions of the work presented in this dissertation and points to future experiments and model simulations that have been motivated by the results presented here.

Chapter 2 Background

2.1. Acute muscle strain injury and injury susceptibility

Acute strain injury is a prevalent problem in sports that involve high-speed running (Clanton and Coupe, 1998). Injury has been shown to occur late in the swing phase of running just before foot contact (Heiderscheit et al., 2005; Schache et al., 2009). During the second half of the swing phase of running, the hamstrings muscles are lengthening due to knee extension and actively generating force to slow the lower limb down before the foot strikes the ground (Chumanov et al., 2007). Because animal models have shown that lengthening contractions induce injury more often than concentric or isometric contractions (Lieber et al., 1991), the hamstring muscles are thought to be predisposed to injury compared to other muscle groups in the body (Clanton and Coupe, 1998).

Animal models of injury have also established a strong connection between the amount of strain experienced by muscle and the extent of injury (Brooks and Faulkner, 2001; Lieber and Friden, 1993; Noonan et al., 1994). As a matter of fact, an *in situ* animal study of the rabbit tibialis anterior measured the maximum local tissue strains at the site of failure (Best et al., 1995). Animal models have also shown that a muscle-tendon unit's architecture influences its strain injury susceptibility (Garrett et al., 1988). In humans, imaging studies have confirmed that injury occurs most often in the biceps femoris long head muscle (BFlh) (De Smet and Best, 2000; Verrall et al., 2003), one of the three bi-articular hamstring muscles, and that injury typically occurs in muscle tissue adjacent to the BFlh's proximal aponeurosis (i.e., the BFlh's proximal myotendinous junction) (Figure 2.1) (Askling et al., 2007; Silder et al., 2008).

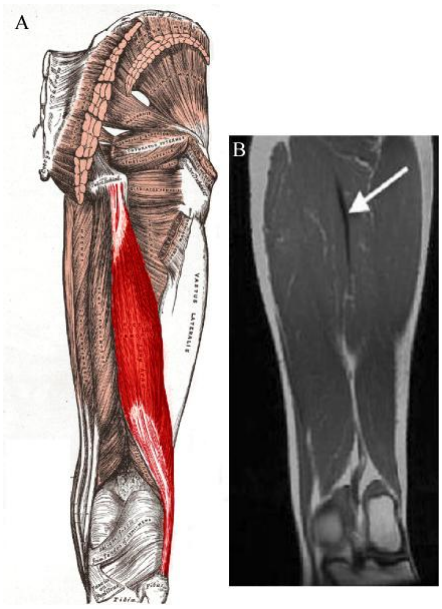

Figure 2.1. BFlh anatomy and MR image of injury

A schematic of the posterior thigh shows the relative position of the BFlh, highlighted in red (A). The BFlh's fibers originate on the proximal aponeurosis, which is located medially and deep relative to the distal aponeurosis. Injury is typically observed at the myotendinous junction adjacent to the proximal aponeurosis, as indicated by the arrow pointing to the region of low intensity scar tissue in the coronal MR image (B) (MR image from Silder et al., 2008).

The biceps femoris long head is a biarticular muscle that originates deep on the ischial tuberosity at the hip and inserts superficially on the fibular head at the knee (Figure 2.1A). Muscle fibers originate on the thicker rope-like proximal aponeurosis, which lies on the medial (deep) side of the muscle, and insert on the broader fan-shaped distal aponeurosis, which lies on the lateral (superficial) side of the muscle (Woodley and Mercer, 2005). The BFlh is generally innervated by a single nervous supply, the sciatic or tibial nerve; however, the number of branches innervating the muscle was found to vary in a cadaveric study of the hamstring muscles (Woodley and Mercer, 2005). The primary functions of the BFlh are to flex the knee and extend the hip, which are

performed when the muscle undergoes concentric contraction (shortens while generating force). The BFlh also slows the lower limb down during running, when the muscle contracts eccentrically (lengthens while generating force) during the late swing phase, which is thought to result in acute strain injury (Noonan and Garrett, 1999).

Acute hamstring strain injury is a non-contact injury and is diagnosed by clinical examinations of palpation, range-of-motion, patient history and pain assessment (Hoskins and Pollard, 2005b). Strain injury treatment consists of rest, ice, compression and elevation (RICE) to reduce swelling and edema. Non-steroidal anti-inflammatory drugs (NSAIDs) are often prescribed to reduce inflammation while the individual rests and the injured muscle-tendon unit recovers. Extended periods of inactivity result in muscle atrophy, and rehabilitation programs attempt to rejuvenate an atrophied muscle with strength training. Rehabilitation programs also aim to return tissue extensibility with passive and active stretching; however, the efficacy of these programs remains questionable (Hoskins and Pollard, 2005a). Once an athlete reaches perceived pre-injury strength and stretch levels and is no longer experiencing pain during functional tests, clinicians clear the athlete to return to sport (Mendiguchia and Brughelli, 2011). While pain-free participation and returning to pre-injury levels seem like an adequate set of return-to-sport criteria, more robust measures are required given the high risk of re-injury observed in multiple sports (12-31%) (Croisier, 2004; Woods et al., 2004) and the ambiguity that remains with respect to causes of and contributing factors to injury (Opar et al., 2012).

A recent dynamic MR study of previously injured subjects found that measured tissue strain during eccentric contraction is higher near the site of previous injury

compared to the same region in subjects without a history of injury (Silder et al., 2010a). In addition, for both previously injured subjects and subjects without a history of injury, the imaging study found that tissue strains are higher in the region of the muscle near the proximal myotendinous junction, which was the site of injury for injured subjects, when compared to other regions in the muscle. These results, in combination with animal models of acute strain injury that showed strain magnitude correlates with the amount of injury (Best et al., 1995; Brooks and Faulkner, 2001; Garrett et al., 1988; Hasselman et al., 1995; Lieber and Friden, 1993; Noonan et al., 1994), indicate that high localized tissue strain is the injury mechanism in acute strain injury. In the research presented here, we use *in vivo* measurements and model predictions of local muscle tissue strain as an indicator for strain injury susceptibility.

2.2. Predictors of injury, rehabilitation and recurrent injury

Previous research into the potential predictors of strain injury has focused on functional measures, such as muscle strength (Orchard et al., 1997), flexibility (Bennell et al., 1999) and neuromuscular control (Cameron et al., 2003); however, no single functional measurement is universally accepted as a stand-alone risk factor for hamstring strain injury (Bahr and Holme, 2003). Moreover, extrinsic measures have been hypothesized as predictors of injury; for example, age (Verrall et al., 2001), ethnic origin (Woods et al., 2004) and player position (Elliott et al., 2011). Despite the considerable research efforts into predictive factors for acute strain injury, only previous injury has garnered widespread support in the literature as an indicator of strain injury susceptibility (Foreman et al., 2006).

Rehabilitation strategies typically focus on mitigating the direct effects of acute strain injury, which are muscle atrophy due to disuse and decreased tissue extensibility due to scar tissue formation. More recent research suggests a multi-step approach is more appropriate, with rehabilitation consisting of pain management, passive loading, dynamic loading and functional loading (Hunter and Speed, 2007). The effectiveness of this progressive approach has yet to be shown; however, and more experimental evidence is required to establish a scientific basis for treatment and rehabilitation of acute strain injury, as demonstrated by high re-injury rates after athletes return to sport (Croisier, 2004).

Acute strain injury causes a wide range of musculotendon changes that are present directly after injury and for months afterwards (Orchard and Best, 2002). For example, immobilization after injury leads to muscle atrophy and weakness, and remodeling at the site of injury leaves scar tissue in place of damaged muscle (Best et al., 2001). Scar tissue has been shown to persist for many months post-injury and likely after athletes are cleared to return to full competition (Silder et al., 2008). In addition, muscle fiber remodeling alters muscle structure at the site of injury, as was shown with diffusion tensor imaging in the gastrocnemius and soleus muscles (Zaraiskaya et al., 2006). Recent MR experiments of eccentric contraction in the BFlh showed that muscle tissue strains are elevated for subjects with previous injury when compared to uninjured subjects (Silder et al., 2010a), demonstrating that differences in musculotendon dimensions can alter muscle mechanics and increase the likelihood of (re-)injury. In the work presented in this dissertation, we used FE modeling to investigate the effect of musculotendon variability in athletes with and without previous injury on strain injury susceptibility.

2.3. Methods to image muscle morphology, structure and function

Magnetic resonance (MR) imaging has served as a valuable non-invasive tool to study muscle morphology, structure and function *in vivo*. High-resolution MR images are able to show detail at sub-millimeter length scales and easily differentiate between biological tissue types (e.g. muscle, connective tissue, bone and skin). For example, I used a commercially available turbo spin echo sequence to acquire high-resolution (0.5 x 0.5 mm^2 pixel size) images of the BFlh (Figure 2.2). The high-resolution images were used to assess proximal aponeurosis width variability in a set of healthy subjects. In general, T1-weighted imaging sequences are used to image anatomy at a high spatial resolution and provide a useful means to assess muscle and connective tissue dimensions (Blankenbaker and Tuite, 2010).

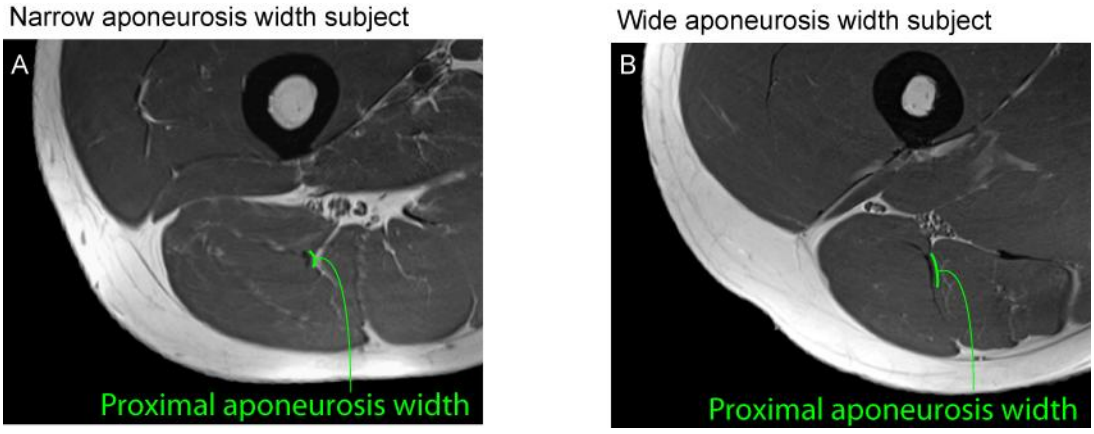

Figure 2.2. Example MR images of variable aponeurosis dimensions

Turbo-spin echo images permit direct visualization and measurement of musculotendon morphological structures, such as the proximal aponeurosis. Example images represent a narrow proximal aponeurosis width subject (A) and a wide aponeurosis width subject (B). Aponeurosis width varied considerably among a healthy subject population (Fiorentino et al., 2012).

Furthermore, Dixon sequences, such as the one used in Chapters 4 and 5, account for the chemical shift artifact between muscle, connective tissue and fat (Dixon, 1984). Dixon sequences acquire separate images when the signal for water and fat are out-of-phase and when water and fat are in-phase. In-phase and out-of-phase images are added to yield an image of water content and subtracted to yield an image of fat content. Water content and fat content images are then added to yield a single image with high spatial resolution and high contract between muscle, connective tissue and fat. These images are similar in appearance to the T1-weighted images in Figure 2.2 but do not suffer from chemical shift artifact.

Muscle fibers are too small to image directly with MRI using current imaging techniques and ensuring human subject safety. Diffusion tensor imaging (DTI) measures the direction of muscle fibers by finding the principal direction of water diffusion (Basser et al., 1994), which are assumed to be collinear (Lansdown et al., 2007; Noseworthy et al., 2010). When combined with muscle and connective tissue segmentations on high-resolution images, DT-based fiber tracking can yield pennation angles (the angle at which fibers connect to the aponeurosis and tendon at the myotendinous junction) and fiber lengths (Damon et al., 2002). The drawback of DTI is the technique's low signal-to-noise ratio and difficulty with fat shift artifact suppression, both of which were observed when attempting to obtain DT images of track and field athletes in the publications from Chapters 4 and 5.

In contrast to static scans for muscle morphology and structure, dynamic imaging measures muscle tissue function during motion. For example, MR-tagging permits direct visualization of tissue motion by acquiring images after planes of undersaturation are

imposed orthogonal to the imaging plane (Zerhouni et al., 1988). While MR-tagging has the advantages of direct visualization of tissue motion and real-time data acquisition (i.e. MR-tagging does not require multiple repetitions to obtain a single series of images), it suffers from a few distinct disadvantages including tag fading during longer acquisitions, linear strain measurements in one direction only (perpendicular to tag lines), and strain measurements at a low spatial resolution (distance between the tag lines).

Advances in MR technology now permit functional measurements, such as velocity (Pelc et al., 1991) and displacement (Aletras et al., 1999), to be encoded directly into the MR signal. For example, cine Displacement ENcoding with Stimulated Echoes (DENSE) measures displacement at a millimeter resolution and for multiple time frames (Kim et al., 2004). At the onset of motion, the cine DENSE sequence applies a displacement encoding gradient that modulates magnetization by a cosine function. The modulation in the image domain creates two distinct echoes in the spatial frequency domain in addition to the usual T1 relaxation signal. After allowing time for motion, an unencoding gradient of equal area to the encoding gradient is applied and the MR signal is acquired as usual. Tissue displacement at a pixel-wise resolution is encoded directly into the phase of first stimulated echo. I used a cine DENSE sequence to measure tissue displacement during dynamic knee extension (Zhong et al., 2009). At each pixel a deformation gradient was found from the relative positions of neighboring pixels, and the deformation gradients were used to find Lagrangian strain tensors (Spottiswoode et al., 2007). Lagrangian strain tensors were diagonalized, and 1st principal strain magnitudes were used to test whether strains were greater during active lengthening than passive lengthening and for subjects with a relatively narrow proximal aponeurosis than a wide.

2.4. Finite element modeling of muscle strain during sprinting

Finite element (FE) models are used in a wide variety of musculoskeletal applications to address hypotheses about joint mechanics (Fernandez and Hunter, 2005), osteoarthritis rehabilitation (Fregly, 2008) and ligament behavior (Pena et al., 2006). We have used FE models to explore questions about strain injury that are not accessible with experimental observation alone (Blemker et al., 2007). For example, how much muscle tissue strain does the BFlh undergo during sprinting? What are the effects of higher muscle activation and larger muscle-tendon length change at faster sprinting speeds? How does variability in musculotendon morphology (e.g. muscle size and aponeuroses dimensions) affect internal muscle tissue strains during sprinting? We addressed these questions with our finite element models by incorporating fine morphological measurements of interest into mesh generation and running simulations with boundary conditions based on sprinting.

Previous modeling studies have used simplified finite element meshes based on geometrical measurements of musculotendon tissue (Rehorn and Blemker, 2010). With simplified models that are not created on a subject-specific basis or based on laborious segmentation of entire structures, a large number of simulations can be performed over a range of physiological measurements to address hypotheses about the effects of musculotendon variability. In addition, FE analysis allows loading and boundary conditions based on experimental observation. For example, activation levels and muscle-tendon lengths can be based on forward dynamic simulations of movement (Thelen and Anderson, 2006), electromyography (EMG) (Silder et al., 2010b), and/or displacement measurements from cine DENSE imaging.

We model muscle and connective tissue as a transversely isotropic, hyperelastic, nearly incompressible materials (Blemker et al., 2005). For a hyperelastic material, stress and strain are related through the 2nd Piola-Kirchhoff stress tensor, the strain energy density function, W, and the right Cauchy-Green deformation tensor, C (equation 2.4.1). The strain energy density function, which determines tissues' deformation in response to imposed boundary conditions, is separated into dilatational (volumetric, W_{vol}) and deviatoric (distortional, W_{dev}) components (equation 2.4.2) (Criscione et al., 2001; Weiss et al., 1996).

$$S = 2\, dW / dC \tag{2.4.1}$$

$$W = W_{vol}(J) + W_{dev}(\alpha, \lambda, \varphi, \phi) \tag{2.4.2}$$

$$W_{vol}(J) = (K/2) \ln(J)^2 \tag{2.4.3}$$

$$W_{dev}(\alpha, \lambda, \varphi, \phi) = W_{\lambda}(\alpha,\lambda) + (G_{\varphi}/Ao)(e^{Ao\varphi^2}-1) + (G_{\phi}/Ao)(e^{Ao\phi^2}-1) \tag{2.4.4}$$

During finite-element simulations, the strain energy density function is minimized; therefore, changes in volume are penalized in the W_{vol} term (equation 2.4.3), where J is volumetric strain and K is the large bulk modulus of the tissue. In equation (2.4.4), W_{λ} represents the strain energy due to muscle activation, α, and along-fiber fiber stretch, λ, and has been described in detail previously (Figure 2.3) (Blemker et al., 2005). Muscle activation scales the known force-length relationship of activated muscle fibers, which is added to the passive contributions to form a total force-length curve (Zajac, 1989). The second and third terms in (2.4.4) represent the contributions from along-fiber and cross-fiber shear strain, respectively, where G_{φ} and G_{ϕ} are along-fiber and cross-fiber shear moduli, Ao is an exponential shear modulus (Sharafi et al., 2011), and φ and ϕ are along-fiber and cross-fiber shear strain.

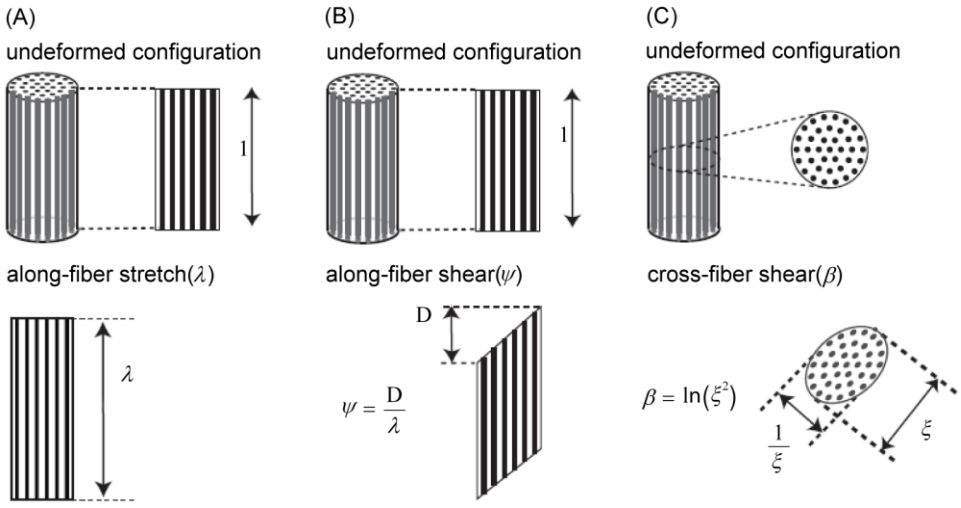

Figure 2.3. Physically-based strain invariants

Schematic representations depict along-fiber stretch, λ (A), along-fiber shear strain, ψ (B) and cross-fiber shear strain, β (C). (from Blemker et al., 2005)

Material parameters for muscle were derived from a recent study that reported stress-strain values of muscle tissue with respect to muscle tissue's fiber (i.e., transvers) axis (Morrow et al., 2010). Connective tissue material parameters were derived from a study in human patellar tendon cadaveric specimens (Chandrashekar et al., 2012). A full description of the sources for material parameters is provided in Chapter 4's *Constitutive model of muscle and connective tissue* section. Also in the methods of Chapter 4, the *Simulations of sprinting* section contains a description of the forward dynamic simulations that are the basis for the boundary conditions used in sprinting simulations. The output of forward dynamic simulations includes muscle activation and muscle-tendon length change, both of which were used as boundary conditions for FE simulations. Chapter 4's methods also describe the way in which we compared simulation predictions of 1st principal strain to experimental measures with dynamic MR imaging.

Chapter 3 Activation and aponeurosis morphology affect in vivo muscle tissue strains near the myotendinous junction

3.1 Abstract

Hamstring strain injury is one of the most common injuries in athletes, particularly for sports that involve high speed running. The aims of this study were to determine whether muscle activation and internal morphology influence *in vivo* muscle behavior and strain injury susceptibility. We measured tissue displacement and strains in the hamstring muscle injured most often, the biceps femoris long head muscle (BFlh), using cine DENSE dynamic magnetic resonance imaging. Strain measurements were used to test whether strain magnitudes are (i) larger during active lengthening than during passive lengthening and (ii) larger for subjects with a relatively narrow proximal aponeurosis than a wide proximal aponeurosis. Displacement color maps showed higher tissue displacement with increasing lateral distance from the proximal aponeurosis for both active lengthening and passive lengthening, and higher tissue displacement for active lengthening than passive lengthening. First principal strain magnitudes were averaged in a 1 cm region near the myotendinous junction, where injury is most frequently observed. It was found that strains are significantly larger during active lengthening (0.19 SD 0.09) than passive lengthening (0.13 SD 0.06) ($p < 0.05$), which suggests that elevated localized strains may be a mechanism for increased injury risk during active as opposed to passive lengthening. First principal strains were higher for subjects with a relatively narrow aponeurosis width (0.26 SD 0.15) than wide (0.14 SD 0.04) ($p < 0.05$). This

result suggests that athletes who have BFlh muscles with narrow proximal aponeuroses may have an increased risk for BFlh strain injuries.

3.2 Introduction

Hamstring strain injury is one of the most common injuries in athletes (Clanton and Coupe, 1998), especially for sports that involve running and sprinting, such as track and field (Bennell and Crossley, 1996), soccer (Ekstrand et al., 2011), Rugby Union (Brooks et al., 2005), Australian Rules Football (Orchard and Seward, 2002), and American Football (Feeley et al., 2008). Of the three biarticular hamstring muscles, the biceps femoris long head (BFlh) muscle is injured most often (De Smet and Best, 2000; Koulouris and Connell, 2003; Verrall et al., 2003). Despite the established prevalence of acute hamstring strain injury in sport, the factors contributing to the high incidence of injury remain poorly understood (Hoskins and Pollard, 2005b).

Animal muscle experiments of injury have found that muscles are most susceptible to injury when they are active and lengthening (Garrett et al., 1987; Lieber et al., 1991). These experiments have been performed at the whole-muscle level and have demonstrated that the magnitude of strain during active lengthening is the best predictor of injury (Lieber and Friden, 1993), though for passive lengthening, the strains that lead to injury are much higher than those for active lengthening (Brooks et al., 1995). However, experiments at the myofibril level found that myofibrils fail at similar sarcomere strains for both active and passive lengthening conditions (Leonard and Herzog, 2010). These two results are inconsistent from the perspective of muscle-tendon unit dynamics. One would expect fibers to stretch less during active lengthening as

compared to passive lengthening, due to the fact that tendons stretch relatively more during active lengthening (Hoang et al., 2007; Zajac, 1989). If fibers stretch less during active than passive lengthening, why are muscles more susceptible to injury during active lengthening? One possible explanation is that, despite the fact that whole muscle-fiber strains may be lower during active lengthening, localized muscle tissue strains (i.e., strains in a small region of the muscle) may be higher during active lengthening as opposed to passive lengthening. However, this comparison has not been made *in vivo*.

The BFlh muscle has a bipennate structure with a narrow, cord-like proximal aponeurosis on the medial side of the muscle and a broad, thin distal aponeurosis on the lateral side (Woodley and Mercer, 2005). Recently, results from a three-dimensional model of the BFlh indicated that the BFlh's internal morphology could contribute to the muscle's increased strain injury risk (Rehorn and Blemker, 2010). The model suggested that the increased strain near the proximal myotendinous junction (MTJ) in the BFlh is due to the fact that the proximal aponeurosis is much narrower than the distal aponeurosis in this muscle and that the relative aponeurosis dimensions may be a predictor of increased strain injury susceptibility in the BFlh. However, the variability of aponeurosis width across individuals and the effect of this variability on measured strain *in vivo* have yet to be explored experimentally.

The goals of this work were to utilize cine DENSE magnetic resonance (MR) imaging to: *i)* measure tissue strains in the BFlh muscle during active lengthening and passive lengthening, *ii)* compare strain magnitudes during active lengthening and during passive lengthening in the region adjacent to the proximal aponeurosis, which is where injury is often observed (Askling et al., 2007; Silder et al., 2008), and *iii)* compare strain

magnitudes in the region adjacent to the proximal aponeurosis for subjects with a relatively narrow proximal aponeurosis to those with a wide aponeurosis during active lengthening. We hypothesize that active lengthening will result in larger strain magnitudes than passive lengthening and that muscles with a narrow proximal aponeurosis will experience larger strains than those with a wide proximal aponeurosis.

3.3 Methods

Subjects

Thirteen (N = 13, 5 female, 8 male) healthy subjects (mean age: 25 SD 5 years, height: 175 SD 7 cm) provided informed consent and were scanned in accordance with the University of Virginia's Institutional Review Board guidelines. All subjects had no known previous hamstring strain injury and were free from lower extremity joint pain at the time of scanning.

Experimental setup

Subjects were positioned in the headfirst, prone position on a non-ferrous exercise device (Silder et al., 2009) in a Siemens Trio 3T MR scanner (Erlangen, Germany) (Figure 3.1A). Subjects performed knee flexion-extension motions at a rate of 0.5 Hz and guided by an auditory metronome. Range of motion inside the scanner depended on the leg length of the subject and was generally 30-40º. A fiber optic angular encoder (Model MR318, Microner Inc., Newbury Park, CA, USA) was fixed to an axis on the back of the device to track rotational motion during scanning (Figure 3.1B). The angular encoder's optical signal was converted to a quadrature signal with a remote encoder interface

(Model MR310, Microner Inc., Newbury Park, CA, USA) such that it could be read by an encoder data acquisition device (Model USB1, USDigital, Vancouver, Washington, USA) and exported to LabVIEW (National Instruments, Austin, TX, USA). A LabVIEW program analyzed the angular encoder signal to determine when maximum knee flexion had been reached and the onset of knee extension (Figure 3.1C), at which time a data acquisition device (Model USB-6211, National Instruments, Austin, TX, USA) sent a square-wave pulse to the scanner to initiate image acquisition.

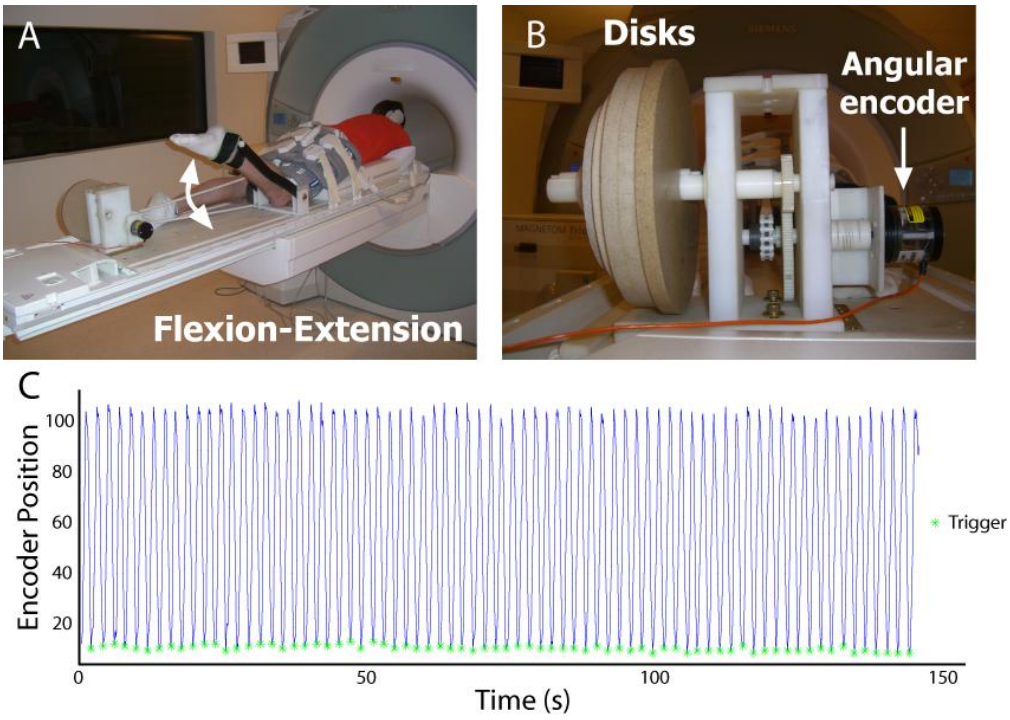

Figure 3.1. DENSE Experimental setup

Subjects were positioned in the head-first, prone position in an MR-compatible exercise device during repeated knee flexion and extension (subject pictured outside the scanner) (A). Cyclic rotation of inertial disks resulted in active lengthening of the biceps femoris muscle (Silder et al., 2009), while an angular encoder signal was sent to a laptop computer running LabVIEW (B). Encoder position values (line) were used to trigger the scanner (asterisk) to begin image acquisition at the onset of knee extension (C). (Example data are from a single DENSE acquisition.)

Static images

Axial plane images were acquired of the right thigh from the biceps femoris' origin on the ischial tuberosity to its insertion on the fibular head. Three coils were used to acquire static images—a body matrix coil on the hip, a large flex coil wrapped around the posterior thigh, and a body matrix coil on the knee. The body matrix coil on the knee was removed prior to dynamic imaging. Static images were acquired with a turbo spin echo sequence and the following parameters: field-of-view 250 x 250 mm^2, imaging matrix 512 x 512, in-plane resolution 0.49 x 0.49 mm^2, slice thickness 5 mm, TE 29 ms, TR 6000 ms and flip angle 120º. Static images were used to define the dynamic imaging plane such that it passed through the proximal aponeurosis, muscle belly and distal aponeurosis (Figure 3.2A). An additional image was acquired in the dynamic imaging plane to confirm the BFlh's orientation in the imaging plane and the presence of the proximal and distal aponeuroses (Figure 3.2B).

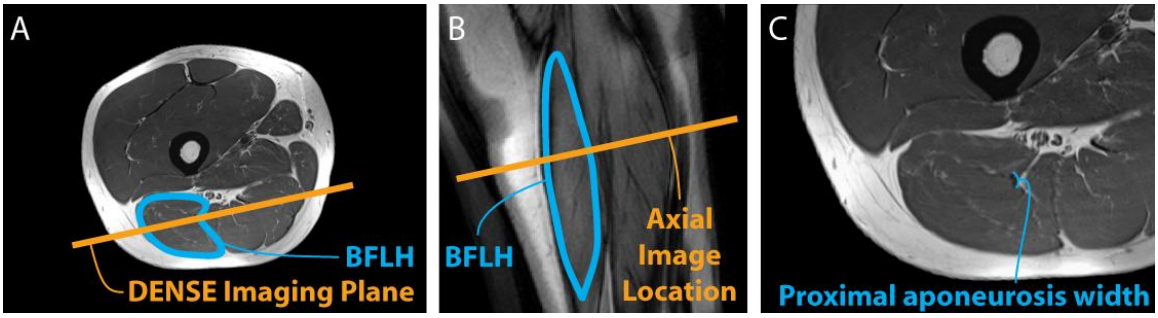

Figure 3.2. DENSE imaging plane and high-resolution images of the BFlh

The DENSE imaging plane was defined on axial plane high-resolution turbo spin-echo images (A), such that the plane included muscle tissue adjacent to the proximal aponeurosis of the BFlh muscle, the muscle belly, and the distal aponeurosis. Prior to DENSE image acquisition, a high-resolution image was obtained in the oblique-coronal DENSE imaging plane to verify the position of the BFlh and the inclusion of the aponeuroses (B). Proximal aponeurosis width measurements were taken directly on axial-plane images (C).

Aponeurosis width measurement

Aponeurosis width measurements were taken directly on static images using Mimics software (The Materialise Group, Leuven, Belgium). For each subject, the end of the proximal aponeurosis was identified by inspection of axial-plane images. The image that was one slice superior from the end of the aponeurosis was used for measurement. This was a more reliable measurement location than the actual end of the aponeurosis, which potentially suffers from averaging over the thickness of the imaging slice. This location was chosen for measurement location because this is precisely where strain magnitudes were found to be the largest in previous computational model simulations (Rehorn and Blemker, 2010). A width measurement was acquired by determining the length of a line drawn directly on the proximal aponeurosis (Figure 3.2C). Subjects were divided into two groups based on the median aponeurosis width, with subjects above the median placed in the wide aponeurosis group (N = 6) and those at or below the median into the narrow aponeurosis group (N = 7). The observer responsible for performing aponeurosis width measurements was blinded to the strain results and vice versa.

Dynamic imaging protocol

Cine Displacement ENcoding with Stimulated Echoes (DENSE) images were acquired in an oblique-coronal imaging plane in the BFlh muscle of the right thigh during repeated knee flexion-extension (Aletras et al., 1999; Kim et al., 2004). In a previous study of skeletal muscle motion in the biceps muscle in the arm (Zhong et al., 2008), DENSE was shown to provide strain measurements that are consistent with strains measured using cine-PC imaging (Pappas et al., 2002). DENSE images provide a measure of

displacement at a pixel-wise resolution by encoding displacement directly into the phase of the MR signal (Figure 3.3A). A spiral *k*-space acquisition and three-point balanced displacement-encoding technique were employed for fast data acquisition and to ensure equivalent phase noise in all directions as well as increased phase signal-to-noise (Zhong et al., 2009). Imaging parameters for the DENSE acquisition included 400 x 400 mm^2 field-of-view, 128 x 128 acquisition matrix, 8 mm slice thickness, 0.08 cycles/mm in-plane and 0.12 cycles/mm through-plane displacement-encoding frequency, TE 1.08 ms, TR 25 ms, flip angle 20º, 1800 ms acquisition window, 35 time frames, and 2.5 minutes scan time.

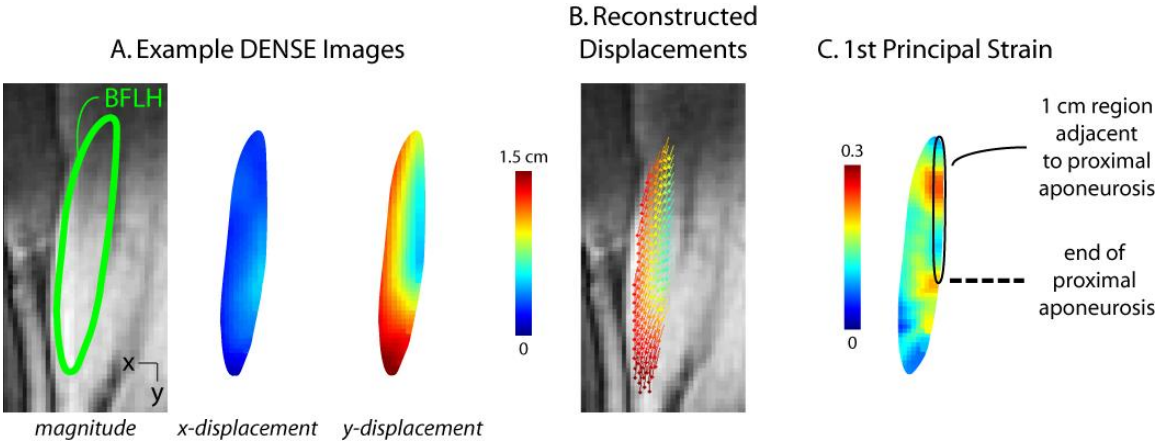

Figure 3.3. Example DENSE images, reconstructed displacements and strain map

Displacement encoding with stimulated echoes (DENSE) images were acquired in an oblique-coronal plane containing the biceps femoris long head muscle (A). Measured displacements were used to reconstruct time-varying tissue position at a pixel-wise resolution (B), where vectors represent displacement from the first image and the vector's color represents the magnitude of displacement. First principal strain was defined as the most positive eigenvalue of the Lagrangian strain tensor and was averaged in the region within approximately 1 cm of the proximal aponeurosis (C).

For active lengthening trials, rotation of inertial disks attached to the back of the device (Figure 3.1B) resulted in active lengthening of the hamstring muscles (Silder et al., 2009). For passive lengthening trials, an individual standing outside the MR scanner moved the subject's leg while the subject remained relaxed. To test strain measurement repeatability, a second active lengthening or passive lengthening trial was acquired for each subject. Repeatability scans found first principal strain measurements to differ by an average of 0.06 (SD 0.03) across all subjects. In addition, an axial-plane data set was acquired in a plane near the inferior end of the proximal aponeurosis to study differences in displacement between the narrow and wide aponeurosis subjects. The order for the four trials (active lengthening, passive lengthening, repeatability, and axial-plane motion) was randomized between subjects and time for rest was included between all trials.

Displacement reconstruction and strain analysis

Time-varying tissue positions were reconstructed from DENSE images, and Lagrangian strain tensors were calculated on a pixel-wise basis (Spottiswoode et al., 2007) (Figure 3.3). The BFlh muscle was outlined on DENSE images, and the MR signal's phase was converted to displacement (displacement = phase / (2π k_e), k_e = encoding frequency) at each pixel. At each time frame, *gridfit*, a function that is freely available on MATLAB's (The Mathworks, Inc., Natick, MA, USA) File Exchange, was used to spatially smooth displacements by employing a linear surface approximation over the entire BFlh region of interest. Displacement measurements at each time frame were projected back to the first time frame, and linear interpolation of the closest 3 pixels' locations was used to define a material description of tissue position at later time frames. Maximum knee

flexion served as the reference configuration for zero displacement and strain calculations. Time-varying tissue positions were determined by temporal fitting with a polynomial. Data sets with a ratio of average through-plane displacement to in-plane displacement greater than 0.3 were disregarded prior to strain analysis, which included five data sets for the passive lengthening acquisitions and no acquisitions for active lengthening. The 0.3 threshold was chosen to ensure that muscle tissue remained in the imaging plane throughout the motion.

Lagrangian strain tensors were found at each pixel with the most positive eigenvalue defined as first principal strain. First principal strain values were averaged in the 1 cm region nearest the BFlh's proximal aponeurosis (i.e. near the myotendinous junction), because recent dynamic MR experiments (Silder et al., 2010a) and computational models (Rehorn and Blemker, 2010) of active lengthening found that tissue strains are higher in the region adjacent to the proximal aponeurosis and this is where injury is typically observed (Askling et al., 2007; Silder et al., 2008). Statistical comparisons were made at the time frame corresponding to full extension, because injury has been observed during the terminal swing phase of sprinting gait (Heiderscheit et al., 2005; Schache et al., 2009).

A one-tailed, paired t-test was used to test whether displacements and strains were larger during active lengthening than during passive lengthening, and a one-tailed, two-sample t-test was used to test whether strains were larger for subjects with a narrow proximal aponeurosis than for subjects with a wide aponeurosis during active lengthening.

3.4 Results

Muscle tissue displacement in the 1 cm region adjacent to the proximal aponeurosis was larger during active lengthening (9.70 SD 0.28 mm) compared to passive lengthening (6.19 SD 0.18 mm) ($p < 0.05$), which demonstrates greater stretch of the proximal tendon during active lengthening. Average 1st principal strain in the 1 cm region nearest the proximal aponeurosis border (Figure 3.4) was greater during active lengthening (0.19 SD 0.09) than during passive lengthening (0.13 SD 0.06) ($p < 0.05$).

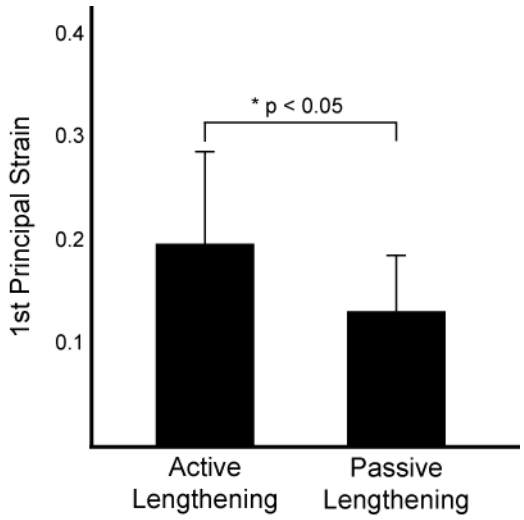

Figure 3.4. Activation strain results

Average 1st principal strain measurements in a region within approximately 1 cm of the proximal aponeurosis of the biceps femoris long head were significantly larger during active lengthening (0.19 SD 0.09) than passive lengthening (0.13 SD 0.06) (*$p < 0.05$).

Proximal aponeurosis width varied from 3.1 mm to 9.2 mm and on average was 5.8 (SD 1.8) mm for all subjects, 4.4 (SD 0.7) mm for the narrow group, and 7.3 (SD 1.3) mm for the wide group. Axial plane color maps of displacement demonstrate that

displacement is smallest along the proximal aponeurosis and increases with distance from the aponeurosis (Figure 3.5). In addition, color maps of displacement showed that the region of low displacement near the proximal aponeurosis had a smaller area for subjects with a narrow proximal aponeurosis as compared to subjects with a wide aponeurosis. During active lengthening, subjects with a narrow proximal aponeurosis experienced greater 1st principal strain (0.26 SD 0.15) in the 1 cm region adjacent to the aponeurosis as compared to the wide aponeurosis group (0.14 SD 0.04) ($p < 0.05$) (Figure 3.6).

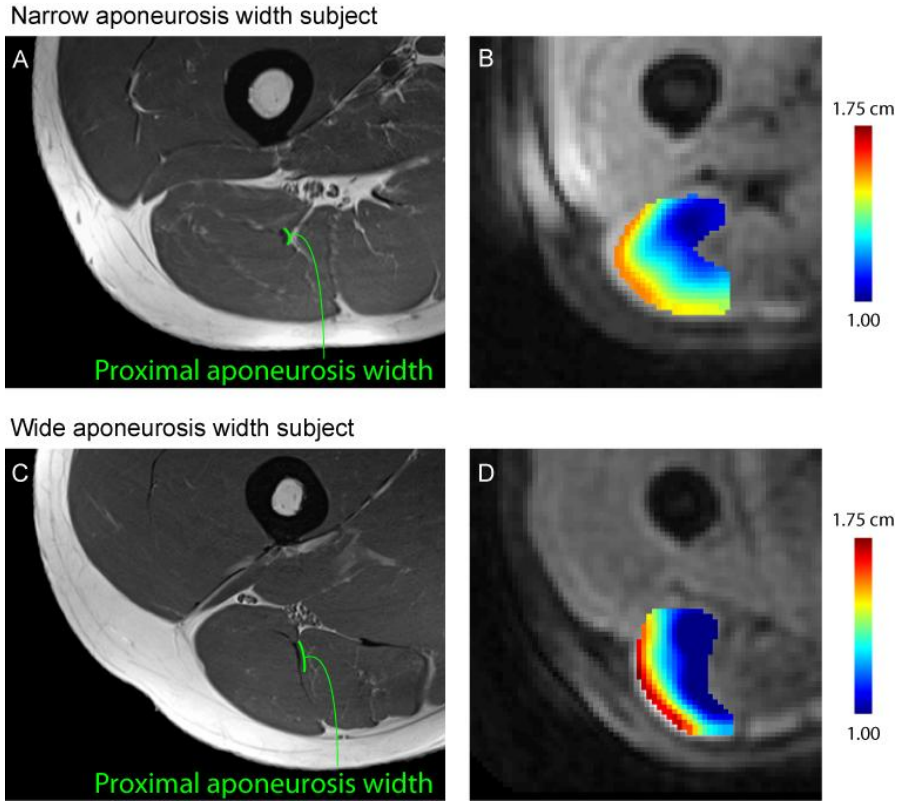

Figure 3.5. Example high-resolution images and displacement color maps

Example high-resolution image and aponeurosis width measurement for a representative subject with a narrow aponeurosis (A) and wide aponeurosis (C) during active lengthening. Color maps of displacement magnitude demonstrate a small region (i.e., area) of localized, low displacement adjacent to the proximal aponeurosis for a narrow width subject (B) relative to a wide aponeurosis width subject (D).

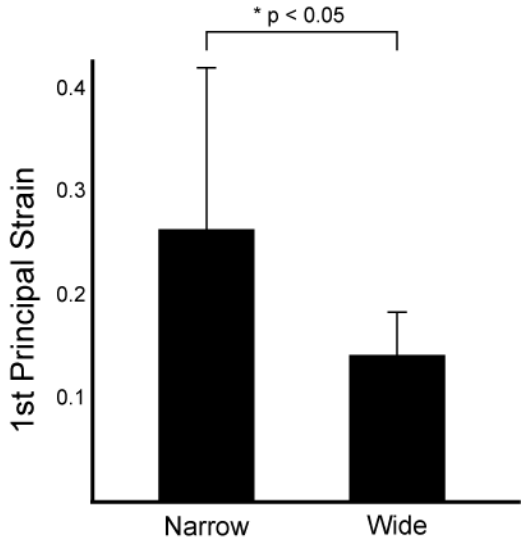

Figure 3.6. Aponeurosis width strain results

Average 1st principal strain measurements in a region within approximately 1 cm of the proximal aponeurosis of the biceps femoris long head were significantly larger for subjects with a narrow aponeurosis width (0.26 SD 0.15) than a wide aponeurosis width (0.14 SD 0.04) (*$p < 0.05$).

3.5 Discussion

This study measured *in vivo* localized strains in the BFlh muscle during active and passive lengthening conditions to answer two questions. Are localized tissue strains elevated during active as opposed to passive lengthening? And, do subjects with a narrower proximal aponeurosis demonstrate elevated localized tissue strains as compared to subjects with a wider proximal aponeurosis? We found that localized tissue strains near the proximal aponeurosis were indeed higher during active lengthening as compared to passive lengthening (Figure 3.4). Furthermore, subjects with a narrower proximal aponeurosis experienced larger localized tissue strains during active lengthening than the subjects with a wider aponeurosis (Figure 3.6).

Our result that *in vivo* localized muscle tissue strains are elevated during active lengthening provides an explanation for why muscles are more susceptible to injury during active lengthening conditions, as compared to passive lengthening. Previous animal models of muscle injury have shown that, while strain magnitude is an excellent predictor of injury for active lengthening (Lieber and Friden, 1993), the relationship between strain magnitude and injury potential is different between active and passive lengthening conditions (Brooks et al., 1995). By contrast, myofibril-level experiments demonstrated that the relationship between sarcomere strain magnitude and myofibril failure is similar for both active and passive lengthening conditions (Leonard and Herzog, 2010). One possible explanation for these disparate findings is that in the animal whole muscle-tendon-unit experiments strains experienced by the muscle tissue (and sarcomeres) are different in the active as compared to the passive lengthening experiments. However, one would expect that, with the presence of a tendon, muscle fiber strains would be less during active lengthening due to increased tendon stretch in active lengthening as compared to the passive lengthening. (Our displacement results also confirm increased stretch of the proximal tendon in the active case.) Nonetheless, while overall fiber strains might be lower during active lengthening in the presence of a tendon, we found that the localized muscle tissue strains adjacent to the proximal aponeurosis were higher, which would result in increased injury potential, particularly in those regions where tissue strains are elevated. More *in vivo* studies that explore a large range of activation levels are needed in order to determine the exact relationship between activation and localized strains.

Displacement and 1st principal strain measurements were found to differ based on the BFlh's proximal aponeurosis width at the inferior end of the muscle. Example displacement color maps in an axial imaging plane (Figure 3.5) showed that subjects with a narrower proximal aponeurosis width had a smaller region of low displacement adjacent to the aponeurosis (Figure 3.5B); whereas subjects with a wider proximal aponeurosis had a wider, more diffuse region of low displacement near the proximal aponeurosis (Figure 3.5D). Average 1st principal strains were found to be higher for subjects with a narrow proximal aponeurosis than for subjects with a wide aponeurosis (Figure 3.6), suggesting that proximal aponeurosis width could influence an individual's susceptibility to strain injury by leading to increased strains in the region where injury is often observed. This result is consistent with previous modeling work that showed that the increased strain near the proximal MTJ in the BFlh is due to the fact that the proximal aponeurosis is much narrower than the distal aponeurosis in this muscle and that the relative aponeurosis dimensions may be a predictor of increased strain injury susceptibility in the BFlh (Rehorn and Blemker, 2010). In contrast, the other two hamstring muscles, which are injured less often than the BFlh (Koulouris and Connell, 2003), have a wide aponeurosis at each end of the muscle (Woodley and Mercer, 2005).

Cine DENSE imaging was performed in a single oblique-coronal imaging plane passing through the proximal aponeurosis, muscle belly, and distal aponeurosis, with the goal of capturing the mechanics of muscle tissue adjacent to the proximal aponeurosis. While this plane allowed us to accurately measure the motion of the muscle in this proximal region, it did not allow us to consistently capture the motion of the distal region of the muscle. In addition, excessive through-plane motion necessitated the removal of

passive data sets for five subjects to avoid spurious in-plane strain results, which limited our ability to test for interactions between activation and aponeurosis morphology. In future studies, a larger cohort of subjects, along with additional loading conditions, will allow for a more detailed analysis of the effects of activation level and morphology on *in vivo* localized strains in the BFlh. It is also possible that extending the dynamic imaging and strain analysis to three dimensions would yield a more robust description of tissue mechanics of the whole muscle, though three-dimensional DENSE imaging over a large field-of-view requires a significant increase in scan time (e.g., 20 minutes to cover 350 x 350 x 110 mm^3 in (Zhong et al., 2010)).

The aponeurosis width measurement used in this study was taken on a single static MR image and toward the inferior end of the proximal aponeurosis. The inferior end of the proximal aponeurosis was chosen for measurement location because previous imaging studies found injury to often occur along the proximal MTJ (Askling et al., 2007; Silder et al., 2008) and computational model simulations of active lengthening predicted strain magnitudes to be largest in this region (Rehorn and Blemker, 2010). Given the large variability in strains in the narrow aponeurosis width group, a more detailed description of aponeurosis dimensions may provide additional insights into the link between BFlh architecture and the muscle's strain injury susceptibility. For example, we noticed that some subjects exhibited a very thin curve-shaped extension of the proximal aponeurosis (a "hook") that penetrated the belly of the muscle, which could potentially influence strain distributions in this region. In addition, the local fiber arrangement in this region could be an important factor, which could be determined with diffusion tensor imaging (Englund et al., 2011). The results presented here motivate the need to conduct

future studies that additionally measure other morphologic factors (such as the “hook” and the fiber arrangement) in a larger cohort of subjects to fully determine relationship between internal muscle-tendon morphology and strains.

Future prospective studies are required to confirm the extent to which the BFlh muscle’s architecture contributes to acute strain injury. Muscle architectural measurements can then be integrated with risk factors that have shown promise as predictors of strain injury, because strain injury risk is likely a confluence of factors—functional and non-functional—instead of a single, stand-alone cause (Bahr and Holme, 2003). Identifying individual athletes and teams at-risk for acute strain injury can be used to motivate training programs that have demonstrated success in preventing injury and re-injury, such as eccentric strength training (Arnason et al., 2008; Askling et al., 2003) and trunk stabilization exercises (Sherry and Best, 2004).

Chapter 4 Computational Models Predict Increases in Localized Muscle Tissue Strain at Faster Sprinting Speeds

4.1 Abstract

Proximal biceps femoris musculotendon strain injury has been well established as a common injury among athletes participating in sports that require sprinting near or at maximum speed; however, little is known about the mechanisms that make this muscle tissue more susceptible to injury at faster sprinting speeds. The biceps femoris long head (BFlh) musculotendon dimensions of 14 athletes were measured on magnetic resonance (MR) images and used to generate a finite element computational model. The model was first validated through comparison with previous dynamic MR experiments. After validation, muscle activation and muscle-tendon unit length change were derived from forward dynamic simulations of sprinting at 70%, 85% and 100% maximum speed and used as input to the computational model simulations. Simulations ran from mid-swing to foot contact, during which time the BFlh is active and lengthening. The model predictions of local muscle tissue strain magnitude compared favorably with in vivo tissue strain measurements determined from dynamic MR experiments of the BFlh. For simulations of sprinting, local fiber strain was non-uniform at all speeds, with the highest muscle tissue strain where injury is often observed (proximal myotendinous junction). At faster sprinting speeds, increases were observed in fiber strain non-uniformity and peak local fiber strain (0.56, 0.67 and 0.72, for sprinting at 70%, 85% and 100% maximum speed). A histogram of local fiber strains showed that more of the BFlh reached larger

local fiber strains at faster speeds. In conclusion, at faster sprinting speeds, peak local fiber strain, fiber strain non-uniformity and the amount of muscle undergoing larger strains are predicted to increase, likely contributing to the BFlh muscle's higher injury susceptibility at faster speeds.

4.2 Introduction

Muscle strain injury remains a prevalent problem in recreational, collegiate and professional sports, consuming a significant portion of sports medicine practice (Kibler, 1990). Athletes participating in high-speed sports, which require sprinting near or at maximum speed, are especially susceptible to acute muscle strain injury (Lysholm and Wiklander, 1987). While it has been well documented that the hamstring muscles are highly susceptible to acute injury while sprinting, the amount of local strain experienced by muscle tissue during sprinting and the mechanisms that lead to increased injury risk with speed remain unclear.

Animal models of injury have established a strong connection between the magnitude of mechanical strain experienced by muscle and the extent of injury (Brooks and Faulkner, 2001; Lieber and Friden, 1993). Furthermore, animal experiments have demonstrated that the site of failure in muscle corresponds to the region of highest localized tissue strain (Best et al., 1995). Experiments in animal tissue have also shown directly that muscle is most susceptible to injury when it is actively generating force and lengthening rather than passively lengthening (Brooks et al., 1995; Lieber et al., 1991). *In vivo* experiments during active lengthening in a running guinea fowl found a regionally dependent amount of tissue strain and an increase in local strain with running

speed (Carr et al., 2011). The ideas set forth by animal models of injury provide a strong basis for understanding mechanisms that potentially lead to muscle injury; however, the direct application and relation of the results to hamstring muscle mechanics during sprinting at high speeds is relatively limited. One of the goals of the current study was to create computational models of the human hamstrings that allow us to predict localized muscle tissue strain while sprinting at high speeds.

Previous studies of the hamstring muscles during running or sprinting generally acquire external measurements of surface electromyography (EMG), ground reaction forces and/or marker-based joint kinematics (Schache et al., 2012; Thelen and Anderson, 2006). Multiple studies have confirmed that the biceps femoris long head muscle, the most commonly injured hamstring muscle (Koulouris and Connell, 2003), is active and lengthening during the late swing phase of sprinting (Chumanov et al., 2012; Thelen et al., 2005; Yu et al., 2008). As sprinting speed increases, previous studies have also shown that the BF muscle activity increases (Higashihara et al., 2010) and it does more negative work (i.e., absorbs more energy) (Chumanov et al., 2007). Counter to intuition, however, peak musculotendon strain remained invariant at top-end sprinting speeds (Chumanov et al., 2007). While marker-based sprinting studies answer questions about potential injury conditions on the global muscle-tendon unit level, injury occurs at the local muscle tissue level; therefore, the behavior of muscle tissue while sprinting may help explain muscle's increased injury susceptibility at faster speeds.

Dynamic imaging and computational modeling have the potential to bridge the gap in knowledge between musculotendon dynamics derived from whole body mechanical models and measurements in animal models of injury. For example, recent

advances in dynamic magnetic resonance (MR) imaging permit strain measurement in muscle tissue during joint motion (Zhong et al., 2008). Dynamic MRI experiments in the BFlh muscle have shown that tissue strain increases with muscle activation (Fiorentino et al., 2012) and is highest near the BFlh's myotendinous junction (MTJ) (Silder et al., 2010a), which is where injury is frequently observed (Askling et al., 2007; Silder et al., 2008). The drawback of dynamic MR experiments is that limitations in scanner bore size and the number of repetitions necessary for dynamic sequences constrain the amount of activation and lengthening that can be studied, which make testing hypotheses about increased strain and higher strain non-uniformity during high-load lengthening contraction infeasible. A recent computational modeling study demonstrated the importance of the BFlh's architecture to its muscle tissue strain distribution and strain injury susceptibility (Rehorn and Blemker, 2010); however, the model was not validated against *in vivo* strain measurement and the simulations were based on non-specific, low levels of activation and muscle-tendon length change. No studies currently exist that show how the behavior of muscle tissue changes with sprinting speed. Understanding how muscle tissue behavior changes with sprinting speed will provide direct insight into muscle's increased injury susceptibility at faster sprinting speeds.

Therefore, the goals of this study were to *(i)* generate a finite-element model of the BFlh based on musculotendon dimensions of athletes participating in high-speed sports, *(ii)* validate model predictions with *in vivo* dynamic MR experiments, and *(iii)* use the model to predict how localized tissue strains in the BFlh are affected by sprinting speed.

4.3 Methods

Finite-element mesh generation and fiber mapping

The dimensions of the finite-element computational mesh were based on the average musculotendon dimensions of University of Virginia Track and Field athletes. Fourteen UVa Track and Field athletes (seven male, height: 177 +/- 9 cm, mass: 71 +/- 10 kg) provided informed consent to participate in a University Internal Review Board approved study. All athletes participated in high-speed events and had no history of acute hamstring strain injury. Magnetic resonance (MR) images were acquired with a Siemens Trio 3T MR scanner (Erlangen, Germany) using a Dixon sequence (TR 7 ms, TE 2.45 ms, flip angle 9 degrees, 5-mm slice thickness, field-of-view 375 mm x 500 mm, imaging matrix 504 x 672, N_{avg} 2) with a high spatial resolution (0.74 x 0.74 mm^2). Axial plane images were acquired from the muscle-tendon unit's origin at the hip to the insertion at the knee. The Dixon imaging sequence acquires separately an image when the signal from water and fat are in-phase and when the signal from water and fat are out-of-phase, and the in-phase and out-of-phase images were combined to provide high contrast between muscle, fat and connective tissue but not suffer from chemical shift artifact (Dixon, 1984).

Biceps femoris long head musculotendon dimensions were measured directly on MR images using OsiriX Imaging Software (Rosset et al., 2004) (Figure 4.1A) or were derived from full segmentations of the muscle using custom in-house MATLAB (The Mathworks, Inc., Natick, MA, USA) software (Table 4.1).

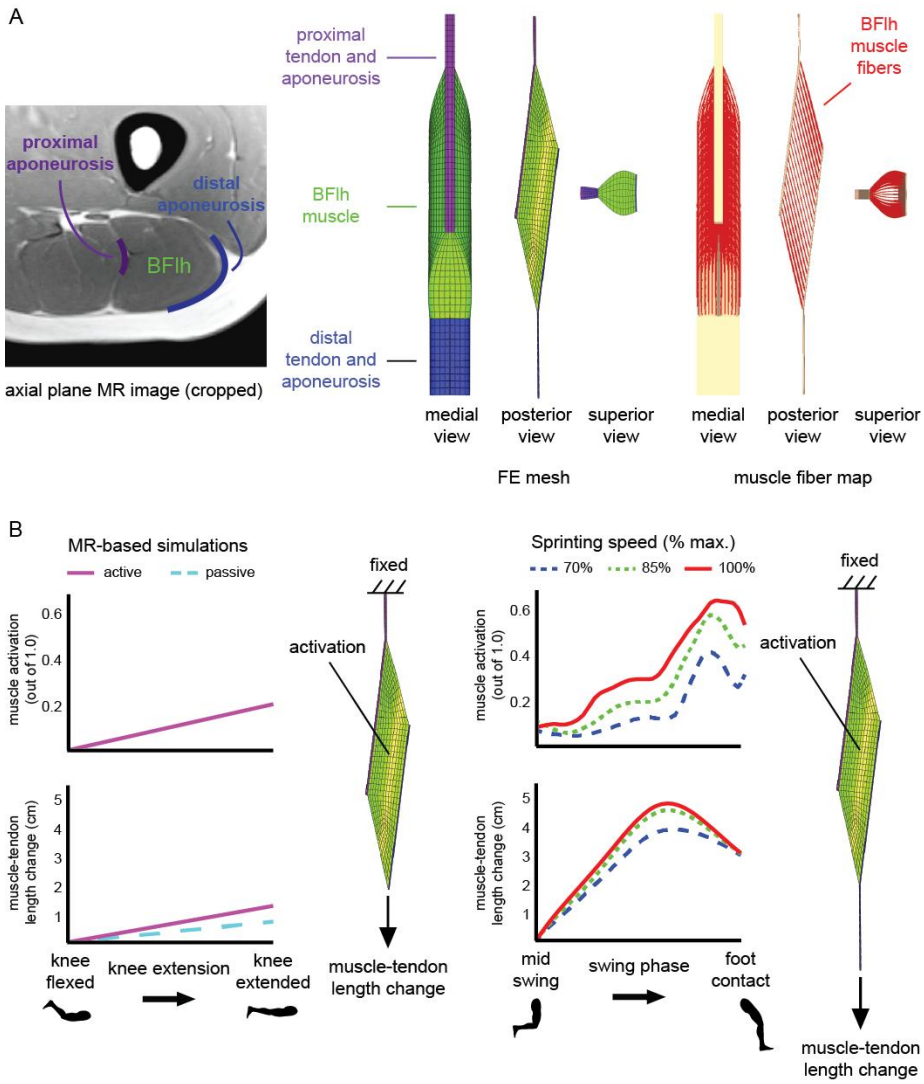

Figure 4.1. Computational model

Musculotendon measurements of collegiate track and field athletes were acquired from axial plane MR images and were used to generate a finite-element (FE) computational mesh (A). Muscle fiber direction was defined at each element by mapping fibers through the FE mesh from the fibers' origin on the proximal aponeurosis to the insertion on the distal aponeurosis (Blemker and Delp, 2005). To compare model predictions and *in vivo* measurements, a separate computational mesh was generated based on MR imaging subjects in a previous study (Fiorentino et al., 2012). The muscle-tendon length change boundary condition was based on the dynamic MR experiment, and muscle activation was based on experiments in the exercise device (Silder et al., 2009) (B). For sprinting simulations, forward dynamic simulations of measured sprinting kinematics yielded BFlh muscle activation and muscle-tendon length change at 70%, 85% and 100% of maximum sprinting speed (Chumanov et al., 2007). Muscle activation was applied to muscle tissue and muscle-tendon length change was applied to the distal end of the distal tendon while holding the proximal end fixed. Simulations were performed from mid-swing to foot contact.

Musculotendon measurements [cm]

muscle			proximal tendon	connective tissue						distal tendon
				proximal aponeurosis			distal aponeurosis			
AP width	ML width	length	length	length	width	thickness	length	width	thickness	length
4.78 (0.58)	3.93 (0.24)	28.55 (3.78)	5.96 (0.14)	17.32 (1.87)	1.13 (0.24)	0.23 (0.06)	20.89 (1.98)	4.87 (0.55)	0.13 (0.02)	9.61 (1.29)

Material parameters

muscle									connective tissue							
σ_{max}	P1	P2	λ_{ofl}	λ^*	A_o	G_ϕ	G_φ	K	P1	P2	λ_{ofl}	λ^*	A_o	G_ϕ	G_φ	K
0.125 MPa	0.04	6.6	1.0	1.06	2.0	3.87×10^{-3} MPa	2.24×10^{-2} MPa	5.0×10^{2} MPa	1.2 MPa	50	1.0	1.03	2.0	3.0 MPa	15.0 MPa	5.0×10^{3} MPa
		dimensionless								dimensionless						

Table 4.1. Sprinting model inputs

Musculotendon measurements were taken from high-resolution axial plane MR images and averaged across 14 University of Virginia Track and Field athletes. Musculotendon measurements were used to define the geometry of the computational mesh. Material parameters were defined for implementation in the transversely isotropic, hyperelastic and quasi-incompressible material model detailed in (Blemker et al., 2005). AP: anterior-posterior. ML: medial-lateral. σmax: peak isometric stress. P1: along-fiber extension multiplicative modulus. P2: along-fiber extension exponential modulus. λofl: along-fiber stretch at optimal fiber length. λ*: stretch at which stress-strain relationship becomes nonlinear. Ao: exponential shear modulus (Sharafi et al., 2011). Gφ: along-fiber shear modulus. Gϕ: cross-fiber shear modulus. K: bulk modulus.

Width and thickness measurements were acquired directly on axial-plane images, whereas muscle length, which runs in the superior-inferior direction perpendicular to the axial imaging plane, was derived from full segmentations. Average musculotendon measurements were used to define the dimensions of the finite-element (FE) mesh, which included three materials (proximal tendon and aponeurosis, muscle, and distal tendon and aponeurosis) connected directly by coincident nodes. A previous modeling study found that a simplified FE computational model based on musculotendon measurements produced the same results as a segmentation-based subject-specific model (Rehorn and Blemker, 2010). The FE computational mesh was generated using TrueGrid software

(XYZ Scientific Applications) and included 2960 hexahedral elements and 2112 nodes. Representative muscle fibers were mapped through the finite element mesh from the fibers' origin on the proximal aponeurosis to the fibers' insertion on the distal aponeurosis (Blemker and Delp, 2005). Muscle fibers were used to define the initial fiber direction at each element, which was an input to the constitutive model, and to calculate spatially varying local tissue strain.

Constitutive model of muscle and connective tissue

A full description of the constitutive model has been published previously (Blemker et al., 2005). Briefly, muscle and connective tissue were modeled as transversely isotropic, hyperelastic and quasi-incompressible (Blemker et al., 2005; Criscione et al., 2001; Weiss et al., 1996). For a hyperelastic material, stress and strain are related through the following expression.

$$\mathbf{S} = 2*\partial\Phi/\partial\mathbf{C}$$

where $\mathbf{S}$ is the 2nd Piola-Kirchoff stress tensor

Φ is the strain-energy density function and

$\mathbf{C}$ is the right-Cauchy-Green strain tensor

To employ transverse isotropy, a preferred direction is defined at each finite element. For tendon, the preferred direction is defined along the length of the connective tissue, or in the superior-inferior direction of the element. For muscle, this is defined by the direction of the muscle fiber and specifies the direction along which active stress is generated. The amount of activation linearly modulates muscle fiber's force-length relationship (Zajac, 1989). The amount of stretch in the direction of the fiber is referred

to as along-fiber stretch (λ). For muscle and connective tissue, the relationship between passive along-fiber stretch and stress is characterized by a nonlinear toe region followed by a linear increase (Zajac, 1989). Shear deformation along the fiber and across the fiber are represented by an exponential relationship between shear strain and stress (Sharafi et al., 2011). The materials are quasi-incompressible, which is enforced by highly penalizing changes in volume. Simulations were run with the nonlinear implicit FE solver Nike3D (Puso et al., 2002). Material constants for muscle (Table 4.1) were defined based on a recent study of along-fiber extension, cross-fiber extension, and along-fiber shear experiments in muscle tissue (Morrow et al., 2010). Peak isometric stress (i.e., specific tension) was taken from a study on the maximum force generating capacity of fibers in human vastus lateralis muscle (Shoepe et al., 2003). Connective tissue parameters (Table 4.1) were derived from linear moduli and stress-strain values reported from experiments in tendon (Chandrashekar et al., 2012).

Comparison to dynamic imaging

We previously measured local tissue strains in the BFlh muscle using a dynamic MRI technique (Fiorentino et al., 2012). The study reported first principal strain in muscle tissue adjacent to the proximal MTJ during passive lengthening and during active lengthening of the BFlh (for N = 13 healthy subjects). To compare *in vivo* measurements and model predictions, a separate finite-element computational mesh was generated based on musculotendon dimensions of the subjects in the dynamic imaging study (Figure 4.1B). Simulation boundary conditions were defined based on measurements while subjects were exercising in a MR-compatible device that induced lengthening

contractions in the hamstrings muscles (Silder et al., 2009). Because the dynamic MR technique measured displacement in muscle tissue, the muscle-tendon length change boundary condition was applied to the distal MTJ while the proximal end was held fixed. Forward dynamic simulations of subjects exercising in the MR-compatible device were used to define the temporal variation in muscle activation (Silder et al., 2009; Thelen and Anderson, 2006).

Simulations of sprinting

Muscle activation and muscle-tendon length change for sprinting were defined based on measured joint kinematics and forward dynamic simulations of sprinting at 70%, 85% and 100% of maximum speed (Figure 4.1B) (Chumanov et al., 2007). A computed muscle control (CMC) algorithm (Thelen and Anderson, 2006) was used to determine muscle excitation patterns such that the forward dynamic model closely matched joint kinematics measured in 19 athletes during treadmill sprinting. To account for muscle redundancy, numerical optimization was used to minimize the sum of squared weighted contractile element forces. Constraints on the timing of muscle excitation were added to ensure that excitations were minimal when EMG data indicated low levels of activation. Muscle-tendon length trajectories were normalized to muscle-tendon lengths in an upright trial for each subject, and the trajectories were then averaged across subjects. Average activation and length trajectories at each speed were then applied as boundary conditions to the muscle and the distal end of the computational mesh, respectively. To apply the appropriate amount of muscle-tendon unit length change relative to the length of the muscle-tendon unit, the finite-element simulation began at the muscle-tendon

length measured on MR images, which corresponded to the mid-swing, or 65% of the gait cycle, and proceeded to foot contact, or 100% of the gait cycle.

Simulation analysis

For each simulation, model predictions of whole muscle fiber length change and local fiber strain were analyzed. To determine whole-fiber length change from simulations, representative muscle fibers were mapped through the computational mesh and tracked throughout the simulation (Blemker and Delp, 2005). To find local fiber strain, sixty-one points along each fiber were tracked throughout the finite-element simulation, which permitted values for local fiber strain to be calculated at 60 intra-fiber segments along each representative muscle fiber. Local fiber strain was calculated as the difference in intra-fiber segment length at each time in the simulation and the original segment length divided by the original length. Local fiber strain is a measure of spatially varying engineering strain. For lengthening, strain is greater than zero. For shortening, strain is less than zero. Based on the local fiber strain data, the peak local strain for each fiber was found at each time step in the simulation, and the peak local fiber strain for each fiber was averaged at each sprinting speed. In addition, to assess the amount of strain non-uniformity, peak local fiber strain for each fiber was plotted against strain of the fiber, where values further away from unity represent more non-uniform strain distributions. Spatially varying fiber strain was analyzed to assess which region(s) of the muscle experienced the largest fiber strain. Fiber strain was averaged in three evenly spaced regions to quantify fiber strain in muscle tissue near the proximal MTJ, in the middle of the muscle and near the distal MTJ. At the overall peak strain for each speed, a

local fiber strain histogram plot demonstrates how much of the muscle was undergoing relatively larger strains.

4.4 Results

The model simulation of dynamic MR experiments compared favorably to experimental measures of tissue strain (Figure 4.2). The model predicted first principal strains in muscle tissue adjacent to the proximal MTJ that were within a standard deviation of measurements during both passive lengthening (0.13 vs. 0.13 +/- 0.06 for MR measurements) and active lengthening (0.22 vs. 0.19 +/- 0.09 for MR measurements) (standard deviation represents variability across imaging subjects). The similar magnitudes of 1st principal strain demonstrate the computational model's ability to replicate muscle tissue strains experienced *in vivo*.

Sprinting simulations showed that whole-fiber length change was non-uniform throughout the BFlh muscle and peaked prior to foot contact (Figure 4.3A). Average maximum whole-fiber length change was 2.7 +/- 0.1 cm, 3.2 +/- 0.1 cm and 3.3 +/- 0.2 cm for maximum MTU lengthening of 3.9 cm, 4.6 cm and 4.8 cm at sprinting speeds of 70%, 85% and 100% of maximum, respectively. Maximum length change of muscle fibers relative to the length change of the MTU was 0.69, 0.70 and 0.69. Strain of the entire MTU was 0.09, 0.10 and 0.11 at 70%, 85% and 100% of maximum speed. Maximum whole-fiber strain averaged over all fibers was 0.24, 0.29 and 0.29 and was at most 0.27, 0.32 and 0.34 for 70%, 85% and 100% of maximum speed, respectively.

Peak local fiber strain was non-uniform throughout the BFlh muscle, reached a maximum before foot contact, and increased with sprinting speed (Figure 4.3B).

Averaged over all fibers, peak local fiber strain was 0.46 +/- 0.08, 0.55 +/- 0.09 and 0.59 +/- 0.09, with a maximum of 0.56, 0.67 and 0.72, for sprinting at 70%, 85% and 100% of maximum speed, respectively. Average peak local fiber strain also increased after normalization by strain of the muscle-tendon unit (5.20, 5.31 and 5.48 for sprinting at 70%, 85% and 100% of max. speed) and was highest at the fastest sprinting speed after normalization by average strain of the whole muscle fibers (1.93, 1.91 and 2.01 for sprinting at 70%, 85% and 100% of max. speed). Maximum peak local strain also increased with sprinting speed after normalization by MTU strain (6.41, 6.49 and 6.67 for sprinting at 70%, 85% and 100% of max. speed) and was highest at the fastest speed after normalization by the maximum whole-fiber strain (2.08, 2.07 and 2.15 for sprinting at 70%, 85% and 100% of max. speed).

To assess the uniformity of local fiber strain and the dependency on strain of the whole fiber, peak local fiber strain was plotted as a function of whole-fiber strain (Figure 4.3C). The average distance to the unity line was 0.17 +/- 0.05, 0.20 +/- 0.07 and 0.22 +/- 0.06 for sprinting at 70%, 85% and 100% maximum speed, indicating that local fiber strain becomes more non-uniform with increasing sprinting speed. For comparison, distance to the unity line was also calculated for simulations of passive and active lengthening MR experiments and was found to be 0.02 +/- 0.01 and 0.05 +/- 0.01 for passive and active lengthening, respectively.

Fiber strain distribution was found to be non-uniform at each sprinting speed and for MR-based simulations, with the largest fiber strain along the proximal MTJ and decreasing with distance toward the distal MTJ (Figure 4.4). Average fiber strain near the proximal MTJ, in the middle of the muscle fibers and near the distal MTJ increased

with sprinting speed, with the largest increases in muscle tissue near the proximal MTJ. In addition, as sprinting speed increased, a larger portion of the muscle experienced larger local fiber strains, as demonstrated by bigger bins at larger strains in a histogram plot of local fiber strain (Figure 4.5).

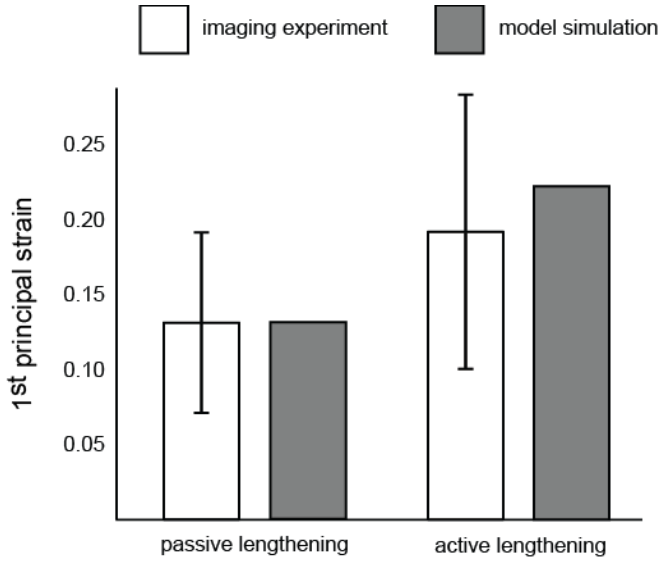

Figure 4.2. Model-imaging comparison

Model simulation results for 1st principal strain were compared to *in vivo* measurements in a recent dynamic MR imaging study (Fiorentino et al., 2012). Average 1st principal strain in the muscle tissue adjacent to the proximal MTJ was reported as 0.13 +/- 0.06 during passive lengthening experiments and 0.19 +/- 0.09 during active lengthening experiments (standard deviation represents variability across N = 13 imaging subjects). Model simulations results found an average of 0.13 and 0.22 for passive lengthening and active lengthening, respectively.

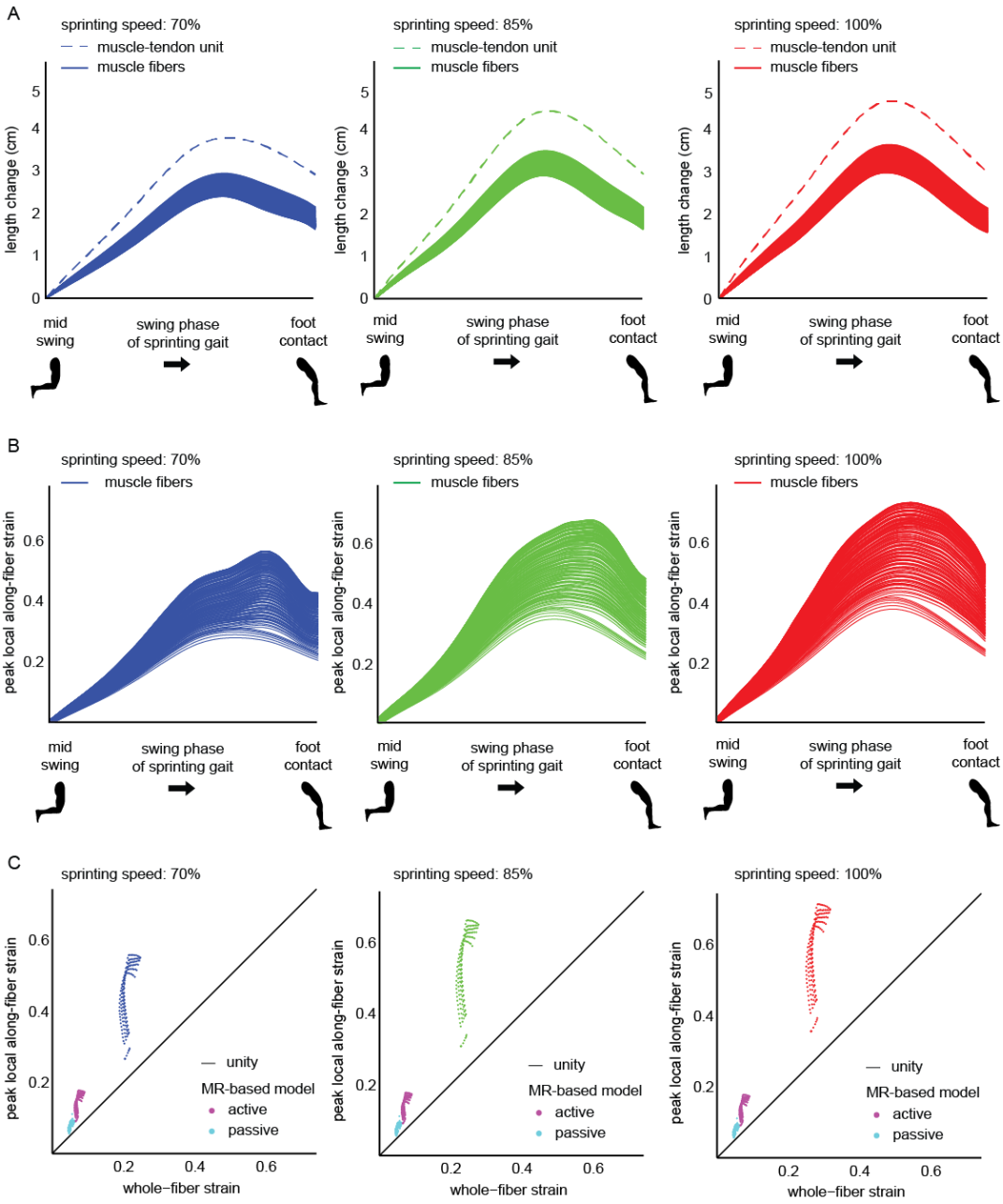

Figure 4.3. Whole-fiber length change and peak local strain during sprinting

Whole-fiber length change in the FE computational model (muscle fibers) was non-uniform throughout the BFlh muscle and increased with sprinting speed (A) (representative fibers are plotted as individual lines). The boundary condition for muscle-tendon unit length change was plotted for comparison (muscle-tendon unit). Peak local along-fiber strain was found for each representative muscle fiber (B). To assess the uniformity of fiber strain while sprinting, local peak fiber strain was plotted as a function of whole-fiber strain for each representative fiber (C). Values on the unity line represent perfectly uniform strain distribution along the fiber.

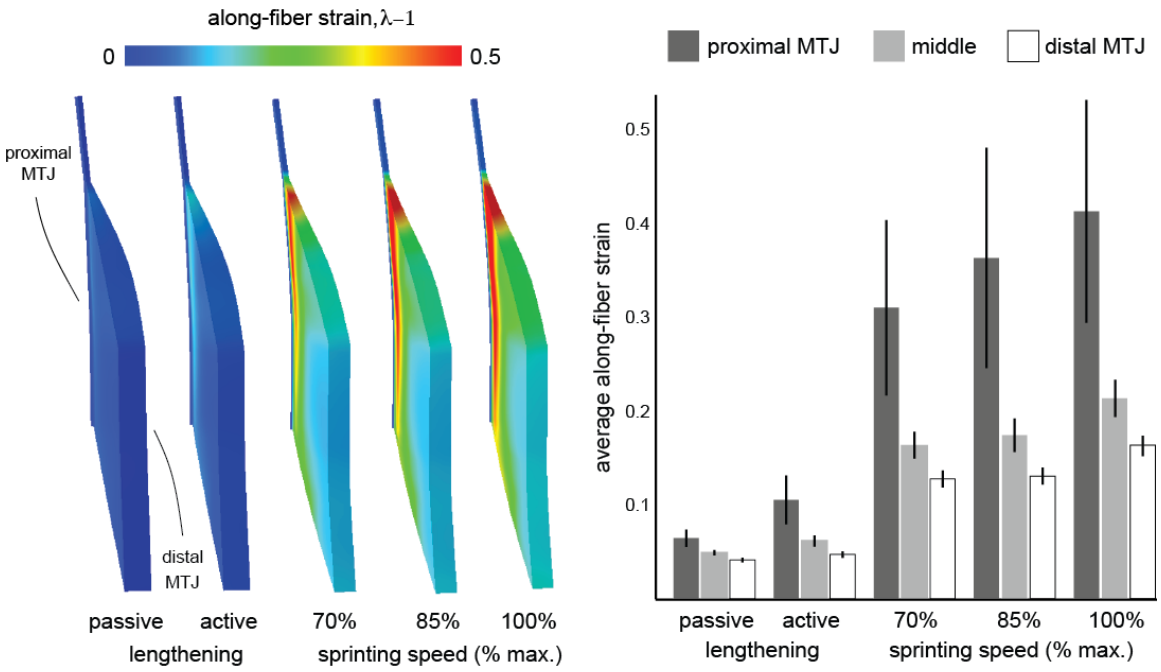

Figure 4.4. Along-fiber strain distribution

Along-fiber strain distribution was analyzed at the time of maximum local strain and was found to be non-uniform throughout the BFlh muscle (shown in longitudinal cross-section). Color maps of along-fiber strain distribution are shown for simulations of passive and active lengthening during dynamic MR experiments and for sprinting at 70%, 85% and 100% of maximum speed. Along-fiber strain was averaged in three evenly spaced regions along the muscle fibers from the proximal myotendinous junction (MTJ) to the distal MTJ. Average along-fiber strain was found to decrease as a function of distance from the proximal MTJ and to increase with speed.

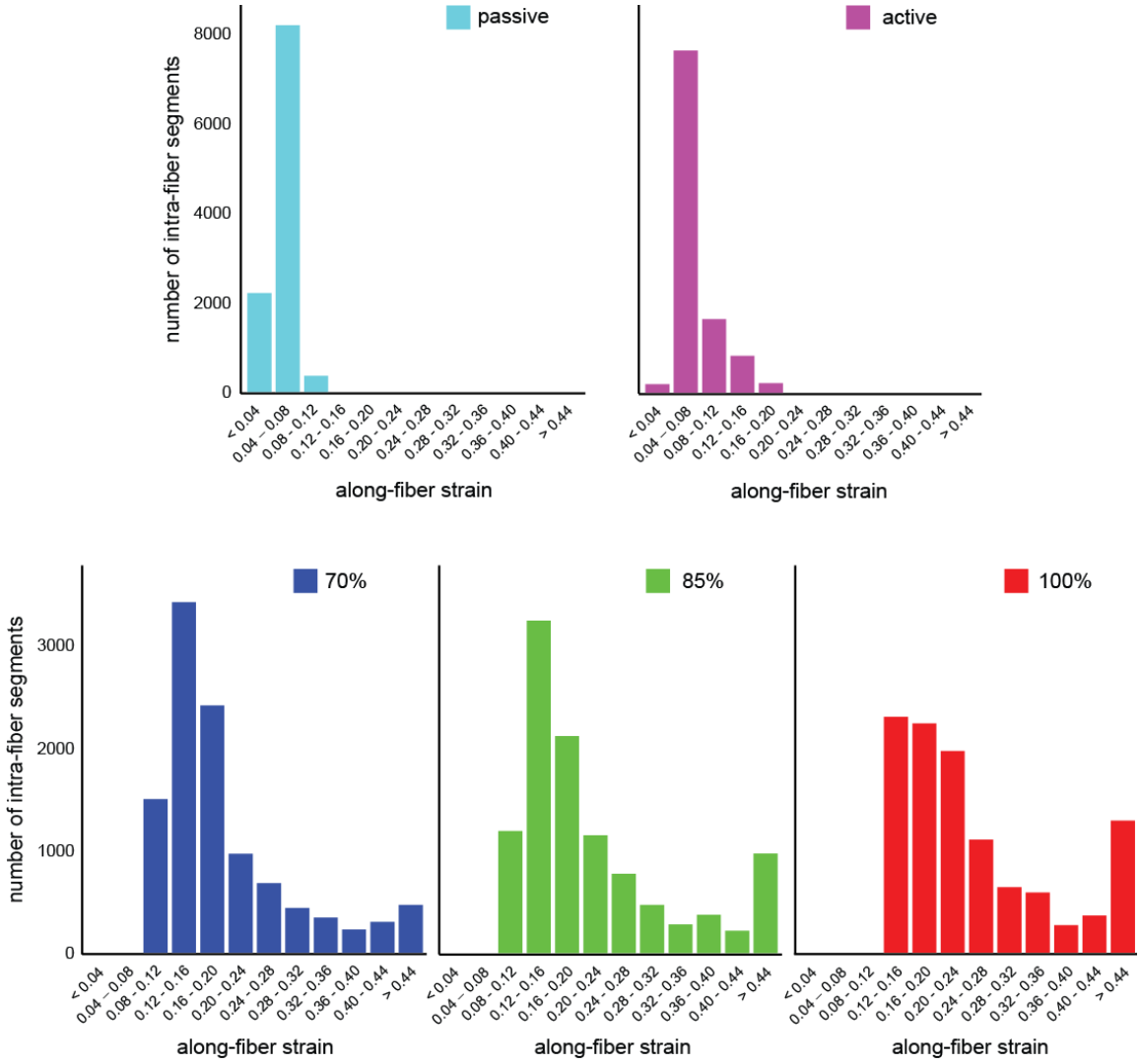

Figure 4.5. Histogram of along-fiber strain

Local along-fiber strain was calculated for 60 intra-fiber segments along 180 fibers and was binned according to amount of strain. Histograms are shown for simulations of passive and active lengthening during dynamic MR experiments (top row) and for sprinting at 70%, 85% and 100% of maximum speed (bottom row). Bigger bins to the right indicate a higher portion of the muscle undergoing larger strains.

4.5 Discussion

Finite-element model simulations accurately predicted local muscle tissue strains when compared to measurements in dynamic MR experiments, demonstrating the model's ability to predict muscle tissue strains experienced *in vivo*. Simulations of sprinting demonstrated increased BFlh peak local fiber strain and higher fiber strain non-uniformity at faster sprinting speeds. Whole-fiber length change relative to muscle-tendon unit length change remained relatively constant with increasing speed; however, peak local fiber strain relative to strain of the muscle-tendon unit and strain of whole muscle fibers increased with speed. These results offer new insights into the deformation of muscle tissue during sprinting and provide an explanation for muscle tissue's increased strain injury susceptibility at faster speeds.

This is the first study to provide direct insight into localized muscle tissue strain in the oft-injured hamstring muscles during sprinting, because measuring local muscle tissue mechanics while sprinting is not yet possible and marker-based studies of sprinting gait only provide information about the behavior of the entire muscle-tendon unit. In the current study, we combined forward dynamic simulation output with finite-element modeling to study the effect of increased sprinting speed on local muscle fiber strain. Previous forward dynamic simulations of sprinting matched marker measurements of joint kinematics by driving a lumped parameter muscle-tendon model with activations (Thelen and Anderson, 2006), or an inverse dynamics approach has been used along with static optimization to derive muscle-tendon unit results from calculated joint torques (Schache et al., 2012). Marker-based studies of sprinting have shown that the BFlh muscle-tendon unit does more work with increasing sprinting speed (Chumanov et al.,

2007; Schache et al., 2011), however, insights into the behavior of the muscle-tendon unit only provide a more global mechanism for muscle injury. The power of the modeling approach described in this paper is that the output of the computational model is spatially varying tissue strain, which can identify regions of large localized tissue strain and test hypotheses about what factors lead to increases in strain injury susceptibility.

At all speeds the computational model found that local fiber strain was non-uniform throughout the BFlh muscle and highest along the proximal MTJ (Figure 4.4), which corresponds to the most frequent injury location in the BFlh (Askling et al., 2007; Silder et al., 2008). Large localized fiber strain where injury is frequently observed supports the hypothesis that large localized tissue strain is the injury mechanism in lengthening contractions during sprinting. Experimental studies in humans have also measured regionally varying muscle tissue strain (Zhong et al., 2008), and, in the BFlh, higher strain closer to the proximal MTJ during lengthening contractions (Silder et al., 2010a). In all three evenly spaced regions along the muscle fiber, sprinting simulations showed that the average magnitude of fiber strain increased with increasing speed, with the largest increases in the muscle tissue near the proximal MTJ. These results are in agreement with sonomicrometry experiments in guinea fowl that found local tissue strain increased with running speed and increases were the largest in regions that were experiences the largest strains at slower speeds (Carr et al., 2011). The current study's results are the first to demonstrate increased muscle tissue strain with sprinting speed in humans, which is important because the BFlh's increased injury susceptibility with sprinting speed has yet to be explained on the local, muscle tissue level.

Model simulations found that peak local fiber strain was nonuniform throughout the BFlh and occurred during the late swing phase of sprinting (prior to foot contact) (Figure 4.3B), which corresponds well with the timing of acute strain injury observed during a sprinting kinematics study (Heiderscheit et al., 2005). The amount of strain non-uniformity increased with sprinting speed, as shown by the larger in difference normalized peak local fiber strain and whole fiber strain in Figure 4.3C (0.17, 0.20 and 0.22 for sprinting at 70%, 85% and 100% maximum speed). Furthermore, as sprinting speed increased, more of the muscle experienced higher fiber strain, which is shown by the relatively larger bins at larger fiber strains in the histogram in Figure 4.5. If acute muscle strain injury is sustained by tissue strain crossing an injury threshold, as suggested by injury after single active stretches in animal experiments (Hasselman et al., 1995), more of the muscle will be susceptible to injury at faster speeds. Similarly, if muscle injury occurs after accumulation of damage to muscle tissue during an activity, as suggested by stretch-shorten cycles in animals over physiological ranges (Butterfield, 2010), more muscle tissue undergoing larger tissue strain will increase muscle's strain injury susceptibility at faster sprinting speeds.

The observed increase in strain non-uniformity and peak local strain was a result of higher muscle activations at faster speeds. The primary factor that leads to this phenomenon is the converging of the BFlh's longitudinal cross-sectional area near the proximal MTJ. The region of muscle tissue near the proximal MTJ is smaller in cross-sectional area than neighboring regions in the middle of the muscle and near the distal myotendinous junction. The relatively larger cross-sectional areas of adjacent tissue generate more force for a given amount of muscle activation, and the larger forces must

be balanced by forces generated in tissue near the proximal MTJ. Given the smaller cross-sectional area, muscle tissue near the proximal MTJ will experience higher stresses and as a result undergo greater strain than neighboring tissue. Higher levels of activation at faster sprinting speeds will exacerbate this effect because of muscle's nonlinear force-length relationship, and tissue near the proximal MTJ will strain even more. More specifically, at higher activation levels the active force-length curve will influence the total force-length curve more, and, given that strains in these simulations occur on the descending limb of the force-curve, relatively more strain will be necessary for a given increase in stress.

Animal models of injury are able to relate the amount of strain and damage to muscle tissue. A study in rabbit extensor digitorum longus (EDL) muscle-tendon units found that an active strain of 0.15 (of the entire muscle-tendon unit) was necessary to detect injury (Hasselman et al., 1995), though the threshold for strain injury has not been consistent in the literature. Other studies found much higher amounts of active muscle-tendon unit strain are necessary to produce injury (e.g., 0.30 strain in Brooks et al. (1995)). Both injury thresholds are larger than the amount of muscle-tendon unit strain in this study (0.11 for sprinting at 100% maximum speed). On the local level, a previous study measured local mechanical strain during passive extension of animal muscle-tendon units, and muscle tissue was shown to suffer injury at a local mechanical strain of 0.61 (Best et al., 1995). The maximum peak local strain in the current modeling study was 0.72 at 100% maximum sprinting speed. It should be noted that the reference configuration for the current study is mid-swing, which is not passively unloaded like

animal muscle-tendon unit injury studies, and caution should be taken when directly comparing the results of the current modeling study to those of animal studies.

The relative amount of muscle fiber strain to muscle-tendon unit strain in sprinting simulations was similar to observations in active lengthening of intact rabbit muscle-tendon units. Sprinting simulations had 2.6 times more fiber strain than MTU strain, and rabbit MTU lengthening experiments showed about 2.6 times more fiber strain than MTU strain averaged over the course of many strain shorten cycles (Butterfield and Herzog, 2005). As demonstrated by the same study, the relative amount of muscle fiber strain in animal muscle-tendon unit experiments depends on the reference length (Butterfield and Herzog, 2005). In addition, the muscle-tendon architecture, magnitude of length change and amount of activation will alter the amount of muscle fiber strain relative to MTU strain. It would also be expected that, relative to the submaximal activations in the current study, maximally activated muscle in animal studies will generate more force and cause more tendon stretch for a given muscle-tendon unit lengthening and result in relatively less muscle fiber strain. In any case, the results presented here demonstrate how muscle-tendon unit strain (0.11) is not representative of the amount of muscle fiber strain (0.29 +/- 0.02 for sprinting at 100% max.), which is also not representative of the amount of local fiber strain (peak 0.59 +/- 0.09 for sprinting at 100% maximum speed).

The computational model's material parameters incorporated recent measurements in muscle (Morrow et al., 2010) and connective tissue (Chandrashekar et al., 2012). A sensitivity analysis of material parameters showed that the shear properties of tendon had the least effect on muscle fiber strain and peak local tissue strain, with

twice as stiff and twice as compliant tendon shear moduli resulting in less than a 1% change in peak local fiber strain. On the other hand, doubling the along-fiber stiffness of tendon had a larger influence on muscle tissue strain, with twice as stiff along-fiber extension moduli (P1 and P2) yielding an 11% increase in peak along-fiber strain. The dependence of muscle fiber strain on tendon stiffness has also been observed in forward dynamic simulations of running (Thelen et al., 2005).

Of all the parameters, peak isometric stress had the biggest influence on peak local fiber strain, with a 50% increase in peak isometric stress resulting in an increase of 13% in peak along-fiber strain. It should be noted that peak isometric stress is an intrinsic property of muscle fibers that may not necessarily change with training. Training likely alters neuromuscular coordination (i.e., the magnitude and timing of muscle activation and muscle-tendon length change) and the amount of muscle tissue available for generating force (i.e., muscle hypertrophy) rather than muscle's intrinsic ability to generate force. Muscle's intrinsic ability to generate force could be changed by altering fiber type composition, given that different fiber types exhibit different levels of peak isometric stress (Shoepe et al., 2003). While the model's results were sensitive to perturbations in certain material parameters, the values that were used yielded results that match experimental data, which inspires confidence in the model's ability to replicate tissue strains experienced *in vivo*. Furthermore, the conclusions of this study regarding increases in tissue strain at faster sprinting speeds were not altered by changes in the model's material parameters.

The current study's model results help fill the gap in knowledge between whole-body kinematics studies and animal muscle fiber experiments by predicting local fiber

strain during physiological muscle activations and muscle-tendon length changes. This approach can be used in future studies of tissue-level muscle function during movements that cannot be imaged directly or measured with joint-level kinematic studies. A future application of this modeling framework would be to generate finite-element models based on the range of musculotendon dimensions rather than using one mesh of the average dimensions of all subjects, as a previous modeling study (Rehorn and Blemker, 2010) and imaging experiments (Fiorentino et al., 2012; Silder et al., 2010a) have found a connection between musculotendon morphology and internal muscle tissue strains. In the present study, however, our goal was to address the effects of increased running speed and not the influence of subject musculotendon dimensions. In addition, the reference configuration for the current study was in the middle of the swing phase of sprinting, because the muscle-tendon length measured on MR images corresponded to the muscle-tendon unit length at 65% of the sprinting gait cycle in forward dynamic simulations; future simulations starting from an earlier point in the gait cycle might find a different absolute magnitude of fiber strain and relative change with speed. An additional limitation to the current approach is that the effects of contraction velocity and passive visco-elasticity were not included in the constitutive formulation. Future model developments include adding these effects in the constitutive equation, which will possibly alter changes with speed, including the relative magnitude strain and the timing between activation, muscle-tendon unit lengthening and local fiber strain.

To summarize, we developed a unique approach to reveal the tissue-level behavior of the oft-injured biceps femoris long head muscle during sprinting. Forward dynamic simulations output of muscle activation and muscle-tendon length change were

incorporated into a finite-element model of sprinting at faster speeds. The models showed that as sprinting speed increases so does peak local fiber strain, fiber strain non-uniformity and the amount of muscle tissue that undergoes larger strain. Increases in peak local fiber strain are attributed to the converging of the BFlh cross-sectional area near the proximal MTJ and increases in muscle activation at faster sprinting speed. Increased peak local fiber strain in the muscle tissue where injury is often found provides additional evidence for the hypothesis that localized fiber strain is the injury mechanism during lengthening contractions. Larger peak fiber strain, higher fiber strain non-uniformity, and a higher percentage of the muscle undergoing larger strain provide evidence to explain muscle's increased strain injury susceptibility at faster sprinting speeds and in high-speed sports.

With the current modeling approach, future model simulations can aid in the design and vetting of potential neuromuscular coordination strategies for reducing strain injury incidence by testing which strategies reduce localized muscle tissue strain. Furthermore, with a better understanding of the connection between neuromuscular strategies and increased strain injury susceptibility at faster sprinting speeds, future training programs can be designed to limit the variables that lead to increased injury susceptibility and reduce the number of acute muscle strain injuries.

Chapter 5 FE Simulations of Sprinting Demonstrate the Implications of Measured Musculotendon Architecture Variability on Strain Injury Susceptibility

5.1 Abstract

The hamstring muscles frequently suffer injury during high-speed running. The factors that make the biceps femoris long head (BFlh) muscle, the hamstring injured most often, more susceptible to injury remain poorly understood. The goals of this project were to measure the musculotendon dimensions of the BFlh and assess the influence of the BFlh's architectural dimensions on its strain injury susceptibility during sprinting. High-resolution magnetic resonance (MR) images were acquired over the entire thigh in 12 athletes, and musculotendon dimensions were measured in the proximal tendon, muscle and distal tendon. Tendon dimensions included the free tendon and aponeurosis (where muscle fibers connect to the tendon). A finite element (FE) mesh was generated based on the average BFlh's musculotendon dimensions, and simulation boundary conditions were defined to match muscle activation and muscle-tendon length change in the BFlh during sprinting. Prior to simulation of sprinting, a model simulation was performed to compare with dynamic MR measurements, and model predictions were well within the standard deviation of 1st principal strain measurements. Model results of sprinting showed that peak local strain was highest along the proximal myotendinous junction (MTJ), which was attributed to the converging of the muscle's cross-sectional area near the proximal

aponeurosis. Additional FE meshes were generated varying the proximal aponeurosis width, muscle width and aponeuroses lengths. Model variations showed that peak local tissue strain increased as the proximal aponeurosis width narrowed, the muscle width increased and the proximal aponeurosis length shortened (listed in decreasing order of peak local strain range). The aponeurosis width and muscle width variation models showed that the relative widths of these structures influence the strain injury susceptibility of the BFlh. The aponeurosis length model variations showed that the heterogeneity of fiber lengths throughout the BFlh had less of an effect on internal tissue strain than the proximal aponeurosis width and muscle width. The results of this modeling study reveal that a muscle-tendon's architecture can influence internal muscle tissue strains during high-speed running and therefore its strain injury susceptibility.

5.2 Introduction

Acute hamstring strain injury is common among athletes who participate in a wide range of high-speed sports, including soccer (Hagglund et al., 2013), rugby (Brooks et al., 2006), American football (Elliott et al., 2011) and track and field (Alonso et al., 2012). Previous research attempting to associate acute muscle strain injury with a variety of intrinsic factors has been inconsistent and inconclusive (Opar et al., 2012). The mixed success in attempting to associate factors about an individual with the possibility of future injury suggests a lack of understanding of hamstring strain injury susceptibility. The purposes of this study were to measure the musculotendon dimensions of the biceps femoris long head muscle, the most commonly injured hamstring muscle, and use finite

element modeling to investigate the influence of musculotendon variability on strain injury susceptibility during sprinting.

The biceps femoris long head (BFlh) muscle has a pennate fiber arrangement with fibers that originate on a relatively narrow proximal aponeurosis and insert on a broader distal aponeurosis (Woodley and Mercer, 2005). Anatomical studies have primarily been based on cadaveric specimens and reported the length of BFlh muscle and tendon dimensions (Friederich and Brand, 1990; Kellis et al., 2010; Ward et al., 2009). To date, anatomical studies have not reported the relative dimensions of the fiber attachment sites (i.e., the proximal aponeurosis and distal aponeurosis) in the BFlh. Furthermore, to what extent variability in musculotendon dimensions affects BFlh function has not been explored in the context of high-speed running.

The BFlh muscle-tendon unit actively generates force while lengthening during the swing phase of running (Thelen et al., 2005). Active lengthening makes the BFlh muscle-tendon unit inherently susceptible to injury, as animal models of injury have shown that generating force while lengthening induces greater injury than generating force at a constant length or shortening (Brooks et al., 1995; Lieber et al., 1991). Moreover, multi-body forward dynamic simulations of high-speed running have shown the BFlh absorbs more energy from the lower limb as running speed increases (Chumanov et al., 2007). While multi-body simulations of running have uncovered reasons behind the BFlh muscle-tendon unit's injury susceptibility, they provide only global measures of muscle-tendon unit dynamics and cannot demonstrate the local effects of the BFlh's architecture and of musculotendon variability between individuals.

Dynamic magnetic resonance (MR) imaging studies and finite element (FE) simulations are able to study the local deformation of muscle tissue during motion. Dynamic MR studies have shown a dependence of local tissue strains on injury history (Silder et al., 2010a) and aponeurosis width (Fiorentino et al., 2012); however, imaging studies are unable to measure strain for high muscle activation levels, large forces and large joint angle ranges, such as the BFlh's conditions while running at high speeds. Computational models provide tissue strain predictions where experiments are not able to produce direct measurements. Finite element model simulations of active lengthening in the BFlh established the importance aponeurosis dimensions to internal muscle tissue strains and high tissue strains where injury is often observed (Rehorn and Blemker, 2010). The previous FE simulations showed that muscle tissue strains were higher for a model with a narrow proximal aponeurosis width and a wider distal aponeurosis width than a model with two wide aponeuroses widths. These simulations, however, represented a single, non-physiological variation in aponeurosis dimensions and were not representative of muscle activations and muscle-tendon length changes experienced during sprinting.

The purpose of this project was to determine the influence of musculotendon variability in the oft-injured BFlh on internal tissue strains and strain injury susceptibility during high-speed running. The specific goals of this project were three-fold. First, the musculotendon dimensions athletes were measured with high resolution MR imaging. Second, finite element computational meshes were generated based on the average musculotendon dimensions of athletes and over the ranges measured in the muscle and proximal aponeurosis width. Third, local tissue strains were predicted while running at

high speeds to explore the influence of musculotendon variability on muscle tissue strains and strain injury susceptibility.

5.3 Methods

Subjects

Twelve University of Virginia track and field athletes (eight male) signed informed consent and were imaged with a 3T Siemens Trio magnetic resonance (MR) scanner (Erlangen, Germany). All athletes competed in sprinting or jumping events and comprised a range of heights (168 cm – 183 cm) and masses (62 kg – 82 kg). Athletes were participating fully in practice and events at the time of scanning and filled out a questionnaire about previous injury prior to scanning. Six athletes had no self-reported history of acute muscle strain injury, and six athletes had self-reported symptoms corresponding to a grade I or grade II injury at any point their past. All injures were at least six months prior to image acquisition. Previously injured athletes and athletes without a history of injury were grouped together because a multivariate ANOVA statistical test did not reveal a significant difference between the measurements for the two groups.

MR image acquisition

Subjects were imaged in the prone position with a MR-compatible foam pad under the hips and torso. The pad flexed the hips and knees to 15-20^{o}. Magnetic resonance images were acquired from the biceps femoris long head's origin in the hip to its insertion below the knee. A Dixon pulse sequence was used to account for the chemical shift artifact that

could interfere with fine musculotendon measurements (TR 7 ms, TE 2.45 ms, flip angle 9 degrees, 5-mm slice thickness, field-of-view 375 mm x 500 mm, imaging matrix 504 x 672, N_{avg} 2) (Dixon, 1984). The Dixon sequence acquires an image when the signals from water and fat are in-phase and an image when the signals are out-of-phase. The in-phase and out-of-phase images are added to produce an image of water content and subtracted to produce a separate image of fat content. The fat and water images are combined to yield an image with high spatial resolution (0.7 x 0.7 mm^2) and high contrast between muscle, fat and connective tissue (Figure 5.1).

Musculotendon measurements

The biceps femoris long head is comprised of a proximal tendon, muscle and distal tendon. The proximal and distal tendons have two parts—a thick and relatively narrow free tendon that originates or inserts onto bone and a thin and relatively wide aponeurosis on which muscle fibers originate and insert at the myotendinous junction (MTJ). The proximal aponeurosis has been qualitatively described as relatively narrower and thicker than the wider distal aponeurosis (Woodley and Mercer, 2005). The dimension of the proximal tendon, muscle and distal tendon were assessed on high-resolution MR images (Figure 5.1) using image analysis software OsiriX (Rosset et al., 2004). The musculotendon measurements defined the shape of the finite-element computational mesh (Table 5.1).

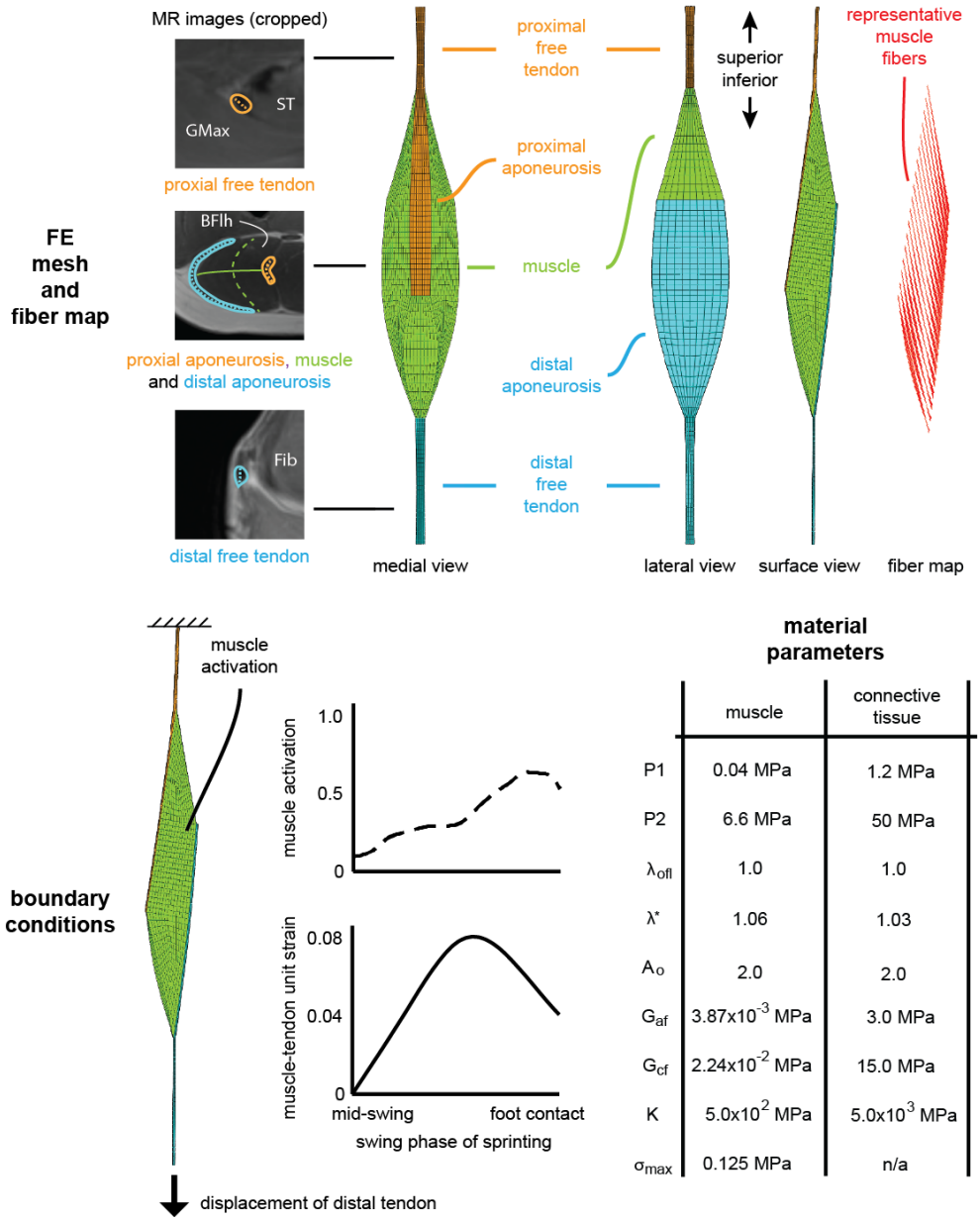

Figure 5.1. BFlh mesh generation and sprinting simulation

The dimensions of FE computational meshes were based on musculotendon measurements on MR images. Width measurements are indicated as dashed lines. Representative muscle fibers were mapped through the FE mesh to define initial fiber direction at each element and calculate spatially-varying local tissue strain. Boundary conditions for the simulation were defined based on measured kinematics and forward dynamic simulations of sprinting in a previous study (Chumanov et al., 2007). Material parameters and the constitutive relationships for muscle and connective tissue are detailed in (Blemker et al., 2005). P1: along-fiber extension multiplicative modulus. P2: along-fiber extension exponential modulus. λ_{ofl}: along-fiber stretch at optimal fiber length. λ^*: stretch at which stress-strain relationship becomes nonlinear. A_o: exponential shear modulus (Sharafi et al., 2011). G_{af}: along-fiber shear modulus. G_{cf}: cross-fiber shear modulus. K: bulk modulus. σ_{max}: peak isometric stress.

[cm]

structure	measurement location	dimension	athletes
proximal free tendon	superior	width	0.78 (0.13)
		thickness	0.21 (0.07)
	middle	width	0.63 (0.08)
		thickness	0.22 (0.05)
	inferior	width	0.69 (0.17)
		thickness	0.23 (0.05)
	n/a	length	7.04 (0.96)
proximal aponeurosis	superior	width	0.68 (0.10)
		thickness	0.23 (0.04)
	middle	width	1.78 (0.31)
		thickness	0.12 (0.01)
	inferior	width	1.68 (0.38)
		thickness	0.11 (0.02)
	n/a	length	17.88 (1.62)
muscle	super taper	width	2.29 (0.38)
		thickness	1.64 (0.23)
	distal apo. end	width	4.80 (0.52)
		thickness	3.11 (0.49)
	middle	width	5.23 (0.43)
		thickness	3.58 (0.59)
	proximal apo. end	width	4.73 (0.49)
		thickness	3.99 (0.45)
	inferior taper	width	3.61 (0.48)
		thickness	2.34 (0.44)
	n/a	length	28.56 (2.10)
distal aponeurosis	superior	width	5.81 (0.64)
		thickness	0.15 (0.02)
	middle	width	6.29 (0.74)
		thickness	0.16 (0.03)
	inferior	width	0.93 (0.21)
		thickness	0.09 (0.02)
	n/a	length	18.74 (2.20)
distal free tendon	superior	width	0.73 (0.11)
		thickness	0.18 (0.05)
	middle	width	0.66 (0.14)
		thickness	0.20 (0.05)
	inferior	width	0.75 (0.16)
		thickness	0.16 (0.05)
	n/a	length	11.10 (1.68)

Table 5.1. Musculotendon measurements for the BFlh

Biceps femoris long head (BFlh) muscle-tendon measurements were made on high-resolution MR images for track and field athletes. Measurements are reported as average (standard deviation).

Connective tissue width and thickness were measured at six superior-inferior locations along the proximal and distal tendons: *i*) the origin / insertion of the muscle-tendon unit (i.e., where the free tendon meets the bone), *ii*) halfway between the origin / insertion and the last image on which no muscle was present, *iii*) the last image where no muscle was present, *iv*) the first image on which muscle was present, *v*) halfway between the first image on which muscle was present and the end of the aponeurosis and *vi*) the end of the aponeurosis. For the free tendon, width measurements were taken as the curvilinear distance corresponding to the long axis of the cross section and through the center of the cross section (Figure 5.1). For aponeurosis measurements, width measurements were taken as the curvilinear distance in the circumferential direction with respect to the center of the muscle's cross section. Because of variable thickness over the width of connective tissue structures, thickness was derived from an outline of the structure and the width measurement, where thickness was defined as the area divided by the width measurement. This approach yielded a more reliable measurement for thickness than arbitrarily choosing a point in the connective tissue structure and direction for thickness measurement, which, for the proximal aponeurosis especially, was considerably variable over its width.

Muscle width and thickness were assessed at five superior-inferior locations: *i*) halfway between the most superior image on which muscle was present and the end of the distal aponeurosis, *ii*) the end of the distal aponeurosis, *iii*) halfway between the most superior and most inferior images on which muscle was present, *iv*) the end of the proximal aponeurosis and *v*) halfway between the end of the proximal aponeurosis and the distal most image on which muscle was present. Muscle thickness measurements

were taken as the curvilinear distance between the middle of aponeuroses and through the center of the cross section (Figure 5.1). For the images on which both aponeuroses were not present, which included the tapering regions superior and distal of the end of the distal aponeurosis and proximal aponeurosis, respectively, the thickness measurement was made perpendicular to the aponeurosis that was present in the image. Muscle width measurements were taken as the curvilinear line through the center of the cross section and the points in the muscle furthest away from the center. This was usually the most anterior and posterior points in the muscle. For muscle thickness and muscle width, the center of the cross section was identified by outlining the muscle and calculating the centroid of the outlined shape. For muscle and connective tissue, the centroid of the segmentation outlines was used to calculate the length of the structure, which was found by summing the linear distance between centroids along the structure's length.

Computational mesh generation and sprinting simulations

The process for building the finite element (FE) computational meshes and simulating sprinting has been described previously (Fiorentino and Blemker, 2013). Briefly, FE meshes were generated with TrueGrid software (XYZ Scientific Applications) and included 3900 hexahedral elements and 5262 nodes (Figure 5.1). The mesh consisted of three materials—proximal free tendon and aponeurosis, muscle and distal aponeurosis and free tendon—connected rigidly by coincident nodes. Representative muscle fibers were mapped from the fibers' origin on the proximal aponeurosis to their insertion on the distal aponeurosis (Blemker and Delp, 2005). Representative muscle fibers defined the initial fiber direction at each element, which was an input to the constitutive model, and

allowed spatially varying local strain to be calculated when analyzing the simulation results. For tendon, the initial fiber direction was defined in the superior-inferior direction.

Muscle and connective tissue were modeled as transversely isotropic, hyperelastic and quasi-incompressible (Blemker et al., 2005; Criscione et al., 2001; Weiss et al., 1996). The constitutive formulation has previously been described in detail (Blemker et al., 2005). Material parameters for muscle were derived from mechanical tests on muscle tissue (Morrow et al., 2010) and maximally active muscle fibers (Shoepe et al., 2003), and material parameters for tendon were derived from mechanical tests in cadaveric patellar tendons (Chandrashekar et al., 2012) (Figure 5.1). Simulations were run with the nonlinear implicit solver Nike3D (Puso et al., 2002) and qualitatively analyzed with PostView software (Maas et al., 2010). Boundary conditions for the FE simulation were defined based on a previous multi-body kinematics study (Chumanov et al., 2007). The muscle activation and length change data were ensemble averages for 19 athletes sprinting on a treadmill at maximum speed. The forward dynamic simulation's output was muscle activation and muscle-tendon unit length change, which, in this study, was applied to muscle tissue and to the inferior end of the distal tendon while holding the superior end fixed, respectively (Figure 5.1). Simulations ran from mid-swing to foot contact, or from 70% of the sprinting gait cycle to 100%.

Strain analysis

To quantify muscle fiber strain and local strain, seventy-six points along 324 representative muscle fibers were tracked throughout the simulation and used to define 75

intra-fiber segment lengths (Blemker and Delp, 2005). Local fiber strain was defined as the difference between the intra-fiber segment length at each point in the simulation and the original segment length divided by the original segment length. Local fiber strain is an engineering strain definition. Peak local strain refers to the largest local strain for each fiber. Maximum peak local strain refers to the largest peak local strain achieved by each fiber at any point in the simulation.

Model variations

Finite-element meshes were generated based on the average dimensions of athletes and variability in proximal aponeurosis width and muscle width. The dimensions for the model variations are listed in Table 5.2. Varying proximal aponeurosis width and muscle width dimensions was motivated by previous modeling work that found a non-physiological widening of proximal aponeurosis width significantly decreased local tissue strains (Rehorn and Blemker, 2010). Proximal aponeurosis width and muscle width were varied based on the range and standard deviation of measurements for all athletes and included the minimum, minus one standard deviation from the average, plus one standard deviation from the average and the maximum.

aponeurosis width model variations

	minimum	average minus standard deviation	average	average plus standard deviation	maximum	
proximal aponeurosis width dimensions (cm)	0.55	0.57	0.68	0.78	0.87	superior
	1.28	1.47	1.78	2.09	2.36	middle
	1.22	1.30	1.68	2.07	2.47	inferior

muscle width model variations

	minimum	average minus standard deviation	average	average plus standard deviation	maximum	
	1.89	1.91	2.29	2.67	2.93	superior taper
muscle width dimensions (cm)	4.21	4.28	4.80	5.31	5.95	distal apo. end
	4.40	4.81	5.23	5.65	5.73	middle
	3.84	4.24	4.73	5.21	5.34	proximal apo. end
	2.75	3.13	3.61	4.09	4.39	inferior taper

Table 5.2. Dimensions of model variations

The model of the average athletes' dimensions was varied to investigate the effects of proximal aponeurosis width and muscle width on internal muscle tissue strain. For proximal aponeurosis width and muscle width variations, width was varied at each superior-inferior location and over the range of measurements. Widths were set to the minimum dimensions, the average minus one standard deviation, the average plus one standard deviation and the maximum dimensions. The average model corresponds to the average dimensions across all athletes. All other dimensions in the model variations remained at the values listed in Table 5.1.

Comparison of model predictions and dynamic imaging

A previous study showed that the FE modeling framework used here was able to accurately predict strain measurements in dynamic magnetic resonance (MR) imaging experiments (Fiorentino and Blemker, 2013). The dynamic imaging study measured local strain in muscle tissue during active and passive knee extension (Fiorentino et al., 2012). A FE mesh was generated based on the musculotendon dimensions of subjects in the dynamic MR study, and boundary conditions were applied to the mesh such that the simulation appropriately matched the experimental conditions. Model prediction of 1st

principal strain was compared within the same region of muscle tissue (1 cm of the proximal MTJ) to the average 1st principal strain magnitude measurement reported in the study. The model predicted first principal strains in muscle tissue adjacent to the proximal MTJ that were within the standard deviation of measurements during both passive lengthening (0.13 for the model vs. 0.13 +/- 0.06 for MR measurements) and active lengthening (0.22 for the model vs. 0.19 +/- 0.09 for MR measurements), where the standard deviation represents variability across imaging subjects.

5.4 Results

Musculotendon dimensions of track and field athletes were variable between subjects, where the standard deviation was 17 +/- 6% of the average dimensions over all measurement locations (Table 5.1). Width dimensions for aponeuroses and muscle were variable along their length, with smaller widths in regions where the transverse cross-section narrows as it approaches the free tendon. Free tendon dimensions were relatively similar at each superior-inferior location. Musculotendon measurements of track and field athletes were generally within the range of values reported in cadaver and *in vivo* studies of the BFlh (Table 5.3), especially when length dimensions were expressed relative to the muscle-tendon unit length. As would be expected when comparing an athletic population to cadavers, however, the athletes' muscle size measurements were generally larger in magnitude than cadavers. The most notable deviation in muscle measurements was the fiber length to muscle length ratio, which was greater in the current study than measurements in cadaveric specimens.

	current study	literature	type	source
muscle-tendon length (cm)	46.7 (100%)	38.9 (100%)	cadaver	Kellis et al., 2012
		39.8 (100%)	cadaver	Kellis et al., 2010
		43.8 (100%)	cadaver	Woodley and Mercer, 2005
muscle length (cm)	28.6 (61%)	29.6 (75%)	cadaver	Kellis et al., 2012
		34.7	cadaver	Ward et al., 2009
		27.4	cadaver	Friederich and Brand, 1990
proximal tendon length (cm)	7.0 (15%)	5.0 (13%)	cadaver	Kellis et al., 2012
		4.9 (12%)	cadaver	Kellis et al., 2010
		6.5 (15%)	cadaver	Woodley and Mercer, 2005
proximal aponeurosis length (cm)	17.9 (38%)	19.1 (48%)	cadaver	Kellis et al., 2010
		20.6 (47%)	cadaver	Woodley and Mercer, 2005
		17.8	in vivo	Rehorn and Blemker, 2010
distal aponeurosis length (cm)	18.7 (40%)	18.3 (46%)	cadaver	Kellis et al., 2010
		18.3 (41%)	cadaver	Woodley and Mercer, 2005
		15.6	in vivo	Rehorn and Blemker, 2010
distal tendon length (cm)	11.1 (24%)	5.3 (14%)	cadaver	Kellis et al., 2012
		5.3 (13%)	cadaver	Kellis et al., 2010
		9.2 (21%)	cadaver	Woodley and Mercer, 2005
proximal aponeurosis width (cm)	1.4 +/- 0.6	0.8	in vivo	Rehorn and Blemker, 2010
		0.6	in vivo	Fiorentino et al., 2012
distal aponeurosis width (cm)	4.3 +/- 3.0	4.0	in vivo	Rehorn and Blemker, 2010
muscle thickness (cm)	2.9 +/- 0.9	2.0 +/- 0.6	cadaver	Kellis et al., 2010
muscle volume (cm^3)	266.6	251.8	in vivo	MR image segmentation
		138.5	cadaver	Friederich and Brand, 1990
fiber length (cm)	10.7 +/- 0.3	6.5 +/- 0.4	cadaver	Kellis et al., 2010
* adjusted to optimal fiber length		9.8	cadaver	Ward et al., 2009*
		10.5	model	Rehorn and Blemker, 2010
		11.5	in vivo	Chleboun et al., 2001
		6.5	in vivo	Potier et al., 2009
fiber length to muscle length	0.37	0.27	cadaver	Kellis et al., 2012
		0.28	cadaver	Ward et al., 2009
		0.25	cadaver	Wickiewicz et al., 1983
pennation angle (^{o})	20.5 +/- 2.4	20.3 +/- 2.6	cadaver	Kellis et al., 2010
		11.6	cadaver	Ward et al., 2009
		0.0	cadaver	Wickiewicz et al., 1983
		11.0	in vivo	Chleboun et al., 2001
		15.6	in vivo	Potier et al., 2009

Table 5.3. Comparison to literature values

Musculotendon measurements for the BFlh model were compared to measurements in the literature. If more than one measurement was reported in a literature source, the numbers were averaged. If more than one measurement location was available for the model or literature source (e.g., superior, middle, inferior), the numbers were averaged and the standard deviation is listed. When provided, percentage of the muscle-tendon unit length is listed in conjunction with the measurements. For the *in vivo* muscle volume comparison, the BFlh was outlined on all MR images and muscle volume was calculated as the in-plane segmentation area times the slice width summed over the muscle's length. Certain fiber length studies adjusted the measured fiber length to optimal fiber length by scaling the measured length by 2.7 μm divided by the measured sarcomere length (Ward et al., 2009). For in the *in vivo* studies of fiber length, fascicles lengths were measured with ultrasound imaging. For pennation angle, the measurement was averaged for the proximal aponeurosis (i.e., deep aponeurosis) and the distal aponeurosis (i.e., superficial aponeurosis).

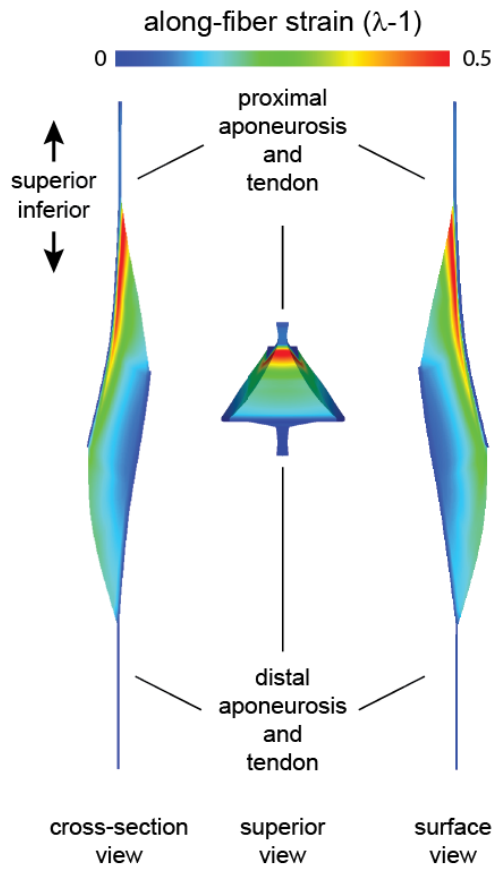

Figure 5.2. FE results

Finite element (FE) results were viewed and qualitatively analyzed with PostView post processing software (Maas et al., 2010). Along-fiber strain was largest along the proximal aponeurosis, or near the proximal myotendinous junction (MTJ), and decreased with distance to the distal aponeurosis. Views are of a longitudinal cross section (cross-section view), from superior of the muscle-tendon unit (superior view) and from the outside surface (surface view).

Finite element results of the model with the average athletes' musculotendon dimensions found highest along-fiber strain in muscle tissue near the proximal aponeurosis (Figure 5.2). For muscle tissue near the proximal aponeurosis, along-fiber strain was higher superiorly than inferiorly. Near the distal aponeurosis, on the other hand, along-fiber strain was higher inferiorly than superiorly. For the BFlh model

variations of proximal aponeurosis width, peak local strain decreased with increasing aponeurosis width (Figure 5.3). For the BFlh model variations of muscle width, peak local strain increased with increasing muscle width (Figure 5.4). For all model variations, peak local strain reached a maximum prior to foot contact.

The maximum peak local strain had a larger range for the proximal aponeurosis width model variations than for the muscle width model variations (Figure 5.5). For the proximal aponeurosis width model variations corresponding to the minimum, the average minus one standard deviation, the average, the average plus one standard deviation and the maximum dimensions, maximum peak local strain was 0.62, 0.61, 0.57, 0.54 and 0.51, respectively. For the muscle width model variations, maximum peak local strain was 0.55, 0.56, 0.57, 0.59 and 0.60, respectively. To compare maximum peak local strain for the aponeurosis width and muscle width models, maximum peak local strain was also plotted as a function of the ratio of aponeurosis width to muscle width. Maximum peak local strain was found to increase for a smaller ratio of proximal aponeurosis width to muscle width.

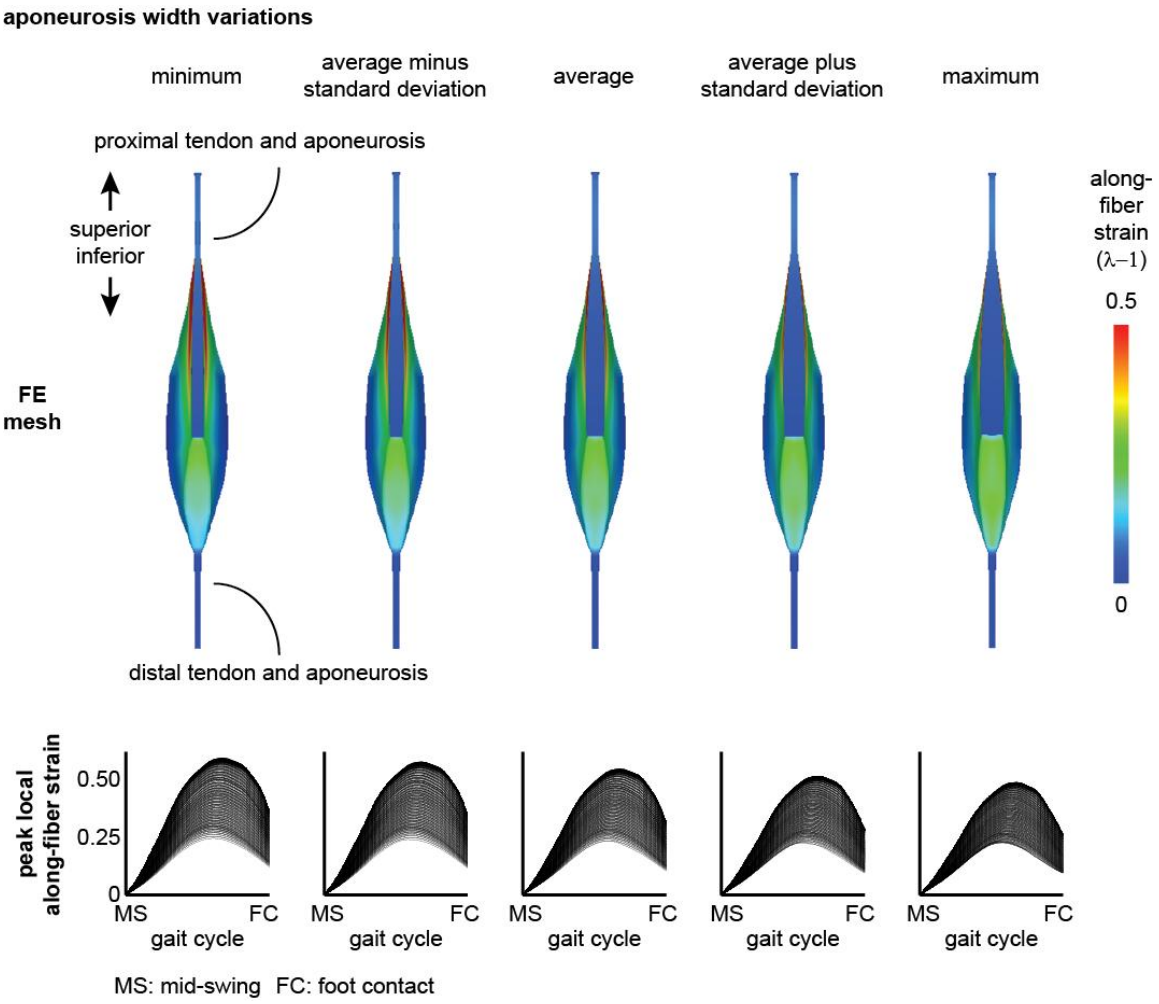

Figure 5.3. Aponeurosis width variation results

The proximal aponeurosis width was varied at each superior-inferior location over a phygiological range and included the minimum, the average minus one standard deviation, the average plus one standard deviation and the maximum dimensions. (Dimensions are listed in Table 5.2.) The average model results correspond to the average dimensions across all athletes. Peak local along-fiber strain plots show the temporal variation from mid-swing to foot contact, where each line represents a single representative fiber. Plots demonstrate decreasing maximum peak local along-fiber strain with increasing proximal aponeurosis width. MS: mid-swing. FC: foot contact.

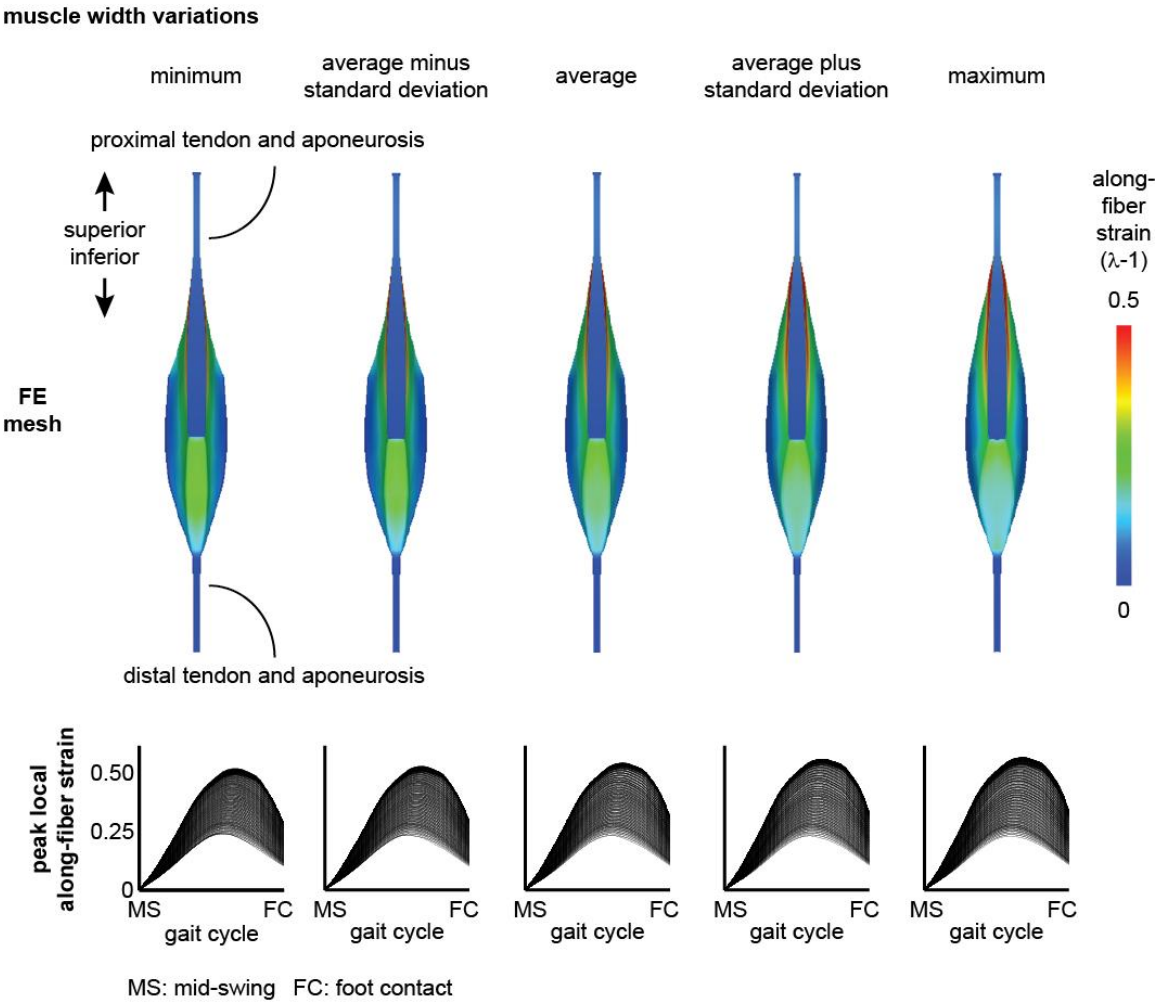

Figure 5.4. Muscle width variation results

The muscle width was varied at each superior-inferior location over a phygiological range and included the minimum, the average minus one standard deviation, the average plus one standard deviation and the maximum dimensions. (Dimensions are listed in Table 5.2.) The average model results correspond to the average dimensions across all athletes. Peak local along-fiber strain plots show the temporal variation from mid-swing to foot contact, where each line represents a single representative fiber. Plots demonstrate increasing maximum peak local along-fiber strain with increasing muscle width. MS: mid-swing. FC: foot contact.

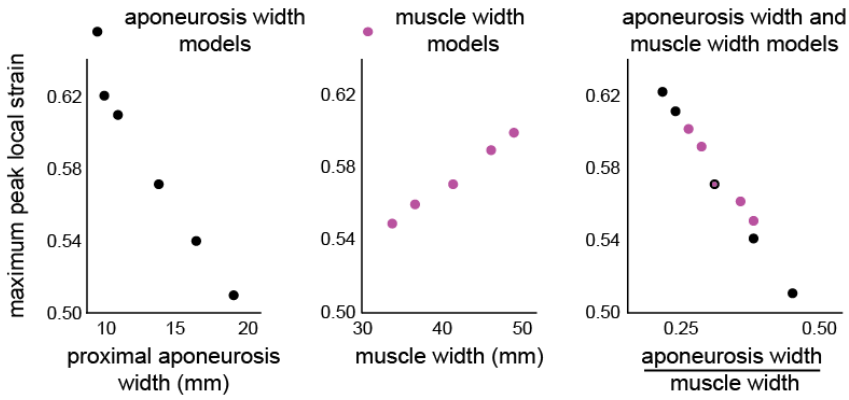

Figure 5.5. Maximum peak local strain results

Maximum peak local strain was plotted for proximal aponeurosis width and muscle width model variations. The width variations results were combined by plotting maximum peak local strain versus the ratio of proximal aponeurosis width to muscle width. The combined plot demonstrates a decreased maximum peak local strain for an increasing ratio of aponeurosis width to muscle width and the larger range of maximum peak local strain for aponeurosis width models than muscle width models.

5.5 Discussion

Biceps femoris long head musculotendon dimensions were measured on high-resolution MR images of elite athletes. Width, thickness and length dimensions of muscle and connective tissue structures were found to vary along the BFlh's length and between subjects. Measurements were generally within the range reported in the literature for cadaver and *in vivo* studies, though certain dimensions were outside those reported previously and no sources were available for many measurements. This is the first study to report detailed BFlh muscle and connective dimensions at multiple superior-inferior locations and for width, thickness and length. Moreover, no other study has reported *in vivo* measurements for aponeuroses dimensions over a range of subjects.

Finite element meshes were generated based on the musculotendon dimensions of athletes and used to predict internal tissue strains during sprinting. Modeling results found peak local strain to be the largest in muscle tissue adjacent to the proximal aponeurosis, which been shown to suffer acute strain injury more often than other regions within the muscle (Askling et al., 2007; Silder et al., 2008). Higher strain closer to the BFlh's proximal aponeurosis has also been observed in experimental studies (Silder et al., 2010a) and computational model simulations (Fiorentino and Blemker, 2013; Rehorn and Blemker, 2010). Larger strain in muscle tissue near the proximal aponeurosis was the result of the BFlh's longitudinal cross section converging from the middle of the muscle (in between the aponeuroses) into the proximal MTJ. Because the muscle's cross sectional area is larger in the middle between the two aponeuroses and smaller adjacent to the proximal aponeurosis, muscle activation generates more stress in the middle than near the proximal MTJ. To balance the difference in stress, the muscle tissue near the proximal MTJ must stretch more than adjacent tissue.

Model variations showed a dependence of peak local strain on musculotendon architecture, with higher peak local strain for decreasing proximal aponeurosis width and increasing muscle width. A narrower proximal aponeurosis width or wider muscle will exacerbate the converging cross-section effect described above and result in even higher muscle tissue strain. Higher strain for narrower proximal aponeurosis has also been observed in the BFlh during low-load active lengthening MR experiments (Fiorentino et al., 2012). A wider muscle was also shown to increase local tissue strains, though to a lesser extent than aponeurosis width over the physiological range of musculotendon measurements. The results of the muscle width and aponeurosis width model variations

demonstrate that musculotendon architecture and physiological variability can influence internal muscle tissue strains and strain injury susceptibility during sprinting.

Biceps femoris long head musculotendon measurements were generally within the range of values reported in previous cadaveric and *in vivo* studies. As would be expected when comparing a group of athletes to a cadaveric population, the magnitude of measurements was generally larger for athletes than for cadavers. When length measurements were expressed relative to the MTU length, the values reported in this study matched more closely the values from cadaver measurements. The largest deviation from previous research was in the fiber length relative to muscle length ratio. The ratio in the current study was larger than for cadaver studies, suggesting that athletes have longer muscle fibers relative to their muscle length. Alternatively, differences between this *in vivo* study and cadaveric specimens could be attributed to the difference in posture when measurements were acquired (Schache et al., 2013), given that cadavers are typically embalmed in anatomically neutral, or the hips and knees fully extended (0^o), and the hips and knees of athletes in this study were flexed to 15-20^o in the MR scanner.

A cadaver study qualitatively described the narrower proximal aponeurosis and wider distal aponeurosis (Woodley and Mercer, 2005), and a previous modeling study reported these dimensions for a single subject (Rehorn and Blemker, 2010). One of the reasons aponeurosis dimensions have not been thoroughly investigated *in vivo* is that the aponeuroses are relatively thin and require high spatial resolution to measure directly. Furthermore, traditional T1-weighted MR imaging suffers from an inherent chemical shift artifact, which, due to the different chemical environments of hydrogen in fat, muscle and connective tissue, cause the signal from fat and muscle tissue to shift into and

overlap the signal from connective tissue. An imaging sequence that accounts for chemical shift, such as the one used in this study, is advantageous for imaging the thin aponeuroses (Dixon, 1984; Reeder et al., 2005). Future investigations might benefit from acquiring images over the entire muscle with a diffusion tensor imaging (DTI) MR sequence (Damon et al., 2002; Porter and Heidemann, 2009), which measures fiber direction throughout the muscle and could provide helpful information when assessing the dimensions of the MTJ.

A detailed cadaver study of the BFlh measured significant variation of fiber length over the length of the BFlh (Kellis et al., 2010), where longer fibers were found superiorly than inferiorly. To compare the current study's representative fiber lengths with the cadaveric literature source, representative muscle fibers were plotted in three-dimensional space and colored by their length (Figure 5.6). Shorter representative fibers were found superiorly than inferiorly, which was in contrast to the cadaver study. To assess the effect of fiber length distribution, two additional models were created—one with the proximal and distal aponeurosis lengths averaged and one with the proximal and distal aponeurosis lengths switched. The first model effectively reduced fiber length heterogeneity by using average aponeurosis lengths, and the second model switched the superior-inferior fiber length distribution by switching the proximal and distal aponeurosis lengths (consistent with the Kellis et al., 2010, measurements).

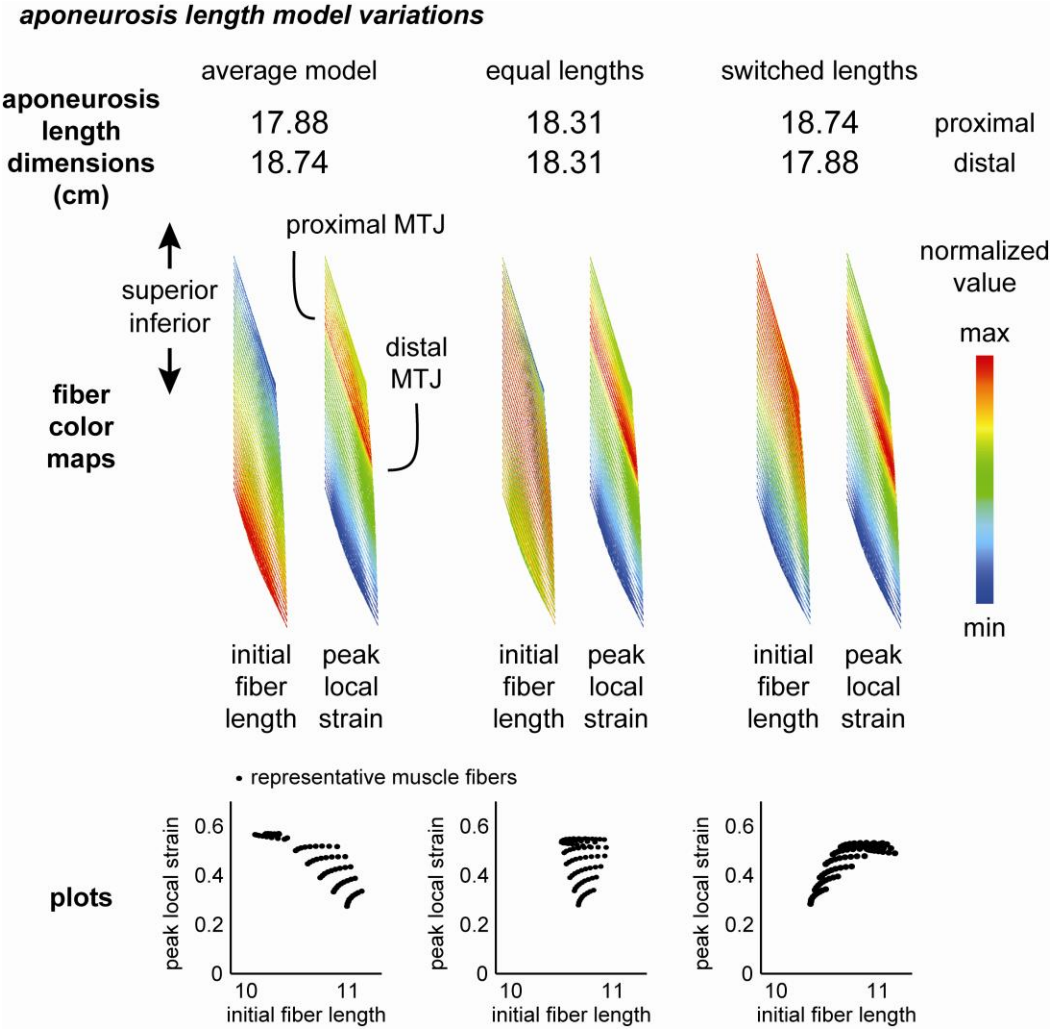

Figure 5.6. Aponeurosis length variation results

The aponeurosis length was varied for both the proximal aponeurosis and distal aponeurosis. The average model results correspond to the average dimensions across all athletes, and the equal lengths model has the length of each aponeurosis set to the average of the measured lengths. The switched length model switches the proximal and distal aponeurosis lengths. Fiber color maps show that initial fiber length depends on the relative dimensions of the aponeurosis lengths, with shorter fibers superior for the average model and shorter fibers inferior for the model with switched lengths. The equal lengths model has a relatively more homogenous fiber length distribution. Regardless of fiber length distribution, larger peak local strain was found superior in the muscle. Scatter plots of initial fiber length versus peak local strain showed that peak local strain's dependence on initial fiber length switched when the aponeurosis lengths switched and that peak local strain was independent of initial fiber length for the average lengths model. MTJ: myotendinous junction.

Sprinting simulations of aponeurosis length variations showed that the distribution of peak local strain was independent of fiber length distribution (Figure 5.6). Peak local strain was consistently higher in more superior fibers than inferior fibers regardless of initial fiber length. Scatter plots confirmed that dependency of peak local strain on initial fiber length was not consistent across the model variations. This suggests that the current study's results would not be affected by fiber length distribution throughout the BFlh muscle and that the converging of the BFlh muscle's cross-section into the proximal MTJ is the more dominant effect than fiber length heterogeneity.

Modeling results have shown that the BFlh's muscle-tendon architecture influences its strain injury susceptibility by altering the magnitude of local muscle tissue strains during sprinting. An individual's muscle and tendon dimensions should be taken into account in combination with other factors when assessing athletes' strain injury susceptibility, as strain injury susceptibility is likely a confluence of factors (Bahr and Holme, 2003). Previous injury and age have garnered the most support as factors that increase strain injury susceptibility (Opar et al., 2012); however, the cause-effect relationships between strain injury susceptibility and post-injury changes and age have yet to be determined. Post-injury muscular changes such as atrophy, edema and strength deficits, which were recently measured at the time of return-to-sport and/or six months afterwards (Sanfilippo et al., 2013), likely contribute to strain injury susceptibility as well. Recently studies have pointed to neuromuscular inhibition as the root cause of these changes and the BFlh's increased injury susceptibility after injury (Fyfe et al., 2013; Sanfilippo et al., 2013), though more direct evidence is required to clarify the role of neuromuscular inhibition in strain injury susceptibility.

The model variation results reported here motivate future work to track how musculotendon dimensions are altered after training or disuse. It is possible that aponeuroses dimensions remodel at the same rate as muscular dimensions, thereby reducing (or not increasing) strain injury susceptibility by compensating for increases in muscle width with increases in aponeurosis width. In addition, increases in muscle width from muscle hypertrophy may be accompanied by reductions in muscle activation, because a larger muscle will require less muscle activation to produce the same amount of force. Reduced muscle activation would be an important consequence as dynamic MR experiments (Fiorentino et al., 2012) and FE simulations (Fiorentino and Blemker, 2013) have shown increased local tissue strain during active lengthening compared to passive lengthening.

Limitations to the current modeling approach include the lack of force-velocity effects and viscoelasticity in the constitutive formulation. Adding these complexities might change the magnitude of local tissue strain and possibly the relative changes with variable musculotendon dimensions. However, the general trends with decreasing aponeurosis width and increasing muscle width would most likely remain, because the rationale behind higher muscle tissue strain near the proximal MTJ is unchanged by force-velocity and viscoelasticity. In other words, the phenomenon demonstrated here that the difference between longitudinal cross section in the middle of the muscle and near the proximal MTJ results in increased muscle tissue strain remains true. In addition, the modeling results of this study would be strengthened by additional *in vivo* imaging studies or cadaver specimen measurements that confirmed the BFlh musculotendon dimensions presented here.

The modeling results in the current study have a wide range of implications for the high injury rates observed in the BFlh. The idea that the muscle-tendon's architecture (i.e., the relative dimensions of the muscle and aponeuroses) influences its strain injury susceptibility provides a better understanding of why the BFlh is injured so often. Moreover, variability in musculotendon dimensions exerting an influence on muscle tissue strain during sprinting provides an additional factor to consider when addressing the BFlh's strain injury susceptibility. More investigation, including a prospective study, is required to ascertain the deterministic capability of measuring an individual's musculotendon dimensions. In the meantime, the modeling results of this study demonstrate the influence of the BFlh's musculotendon dimensions on internal muscle tissue strains during sprinting, and, as such, the BFlh's structure should be taken into consideration when trying to understand, explain and reduce the high injury rates observed in the BFlh muscle.

Chapter 6 Conclusions

Previous strain injury research had rarely studied muscle tissue directly with *in vivo* imaging and had not investigated how muscle deforms during high-speed running. The *in vivo* imaging results presented within this dissertation improve the understanding of how muscle deforms under loading conditions known to make muscle susceptible to injury (active lengthening). For higher loaded movements that could not be imaged with dynamic MR, finite element model simulations predicted muscle tissue deformation and local tissue strains. Simulations of sprinting provide insight into how muscle deforms during a potential injurious task and what are the functional effects of variation in musculotendon dimensions. These insights into acute strain injury obtained with *in vivo* imaging and FE modeling make valuable contributions to the field and will provide a better understanding of strain injury susceptibility in the BFlh muscle.

6.1 Contributions

The results of the research presented here will make important contributions to the scientific and clinical communities, as detailed in the sections below. While local strain concentration has been measured during active lengthening (Silder et al., 2010a), the results of this work suggest two possible factors, muscle activation and morphology, that contribute to increased localized muscle strain and therefore strain injury susceptibility. In general, the data collected during MR imaging describes muscle structure and function in ways that have not been published previously and will provide new insights into *in vivo* muscle anatomy and tissue motion. In fact, the insights gained by studying the morphology, structure and function of the BFlh can be extended to any number of

muscles in the body to contribute to a wide scope of musculoskeletal applications, such as adaptations to neuromuscular disease, surgical intervention and chronic injury. In addition, rigorous investigations provide a scientific, rather than anecdotal or empirical, basis for treatment, rehabilitation and return-to-sport criteria (Heiderscheit et al., 2010). Clinically, identifying factors that contribute to strain injury susceptibility will aid clinicians in selecting athletes for specialized strain injury prevention programs (Proske et al., 2004). Furthermore, with a better understanding of the influence of musculotendon architecture in strain injury, the results presented here can help physical therapists and doctors place athletes in injury-specific rehabilitation programs.

In vivo measurements of BFlh musculotendon dimensions

The results of this dissertation are the first to report detailed *in vivo* musculotendon measurements in the BFlh. Previous studies reported the BFlh's dimensions in cadaveric specimens, and these studies never reported the transverse dimensions of the aponeuroses (e.g., Kellis et al., 2012). *In vivo* studies often reported only one dimension or a small group of dimensions (e.g., Chleboun et al., 2001). The measurements in this dissertation cover 39 dimensions of width, thickness and length for connective tissues and muscle covering the entire MTU. Furthermore, measurements were reported for athletes, providing detailed information for a subject population that is often injured during sport. Interestingly, musculotendon dimensions were found to vary along the length of each structure and between dynamic MR imaging subjects and track and field athletes.

In vivo measurements of local tissue displacement and strain

We measured local tissue displacement and strain in the BFlh during knee joint motion. The work presented in this dissertation is the first to provide local tissue displacement and strain measurements during active and passive lengthening of the oft-injured BFlh muscle. This comparison is meaningful because the reason muscle is injured more often during active lengthening than passive lengthening has not yet been established. The results in Chapter 3 suggest that local muscle tissue strain increases with muscle activation are responsible for increased injury susceptibility during active lengthening. In addition, local muscle tissue strain measurements allow for comparison between subjects, and this work is the first to show that strain measurements differ between individuals with different musculotendon dimensions (wide vs. narrow proximal aponeurosis).

Local tissue strain predictions during sprinting

A framework was developed for predicting local tissue strains during sprinting, which have not been reported previously in the literature. This was accomplished by combining forward dynamic simulation output of muscle activation and length change (Chumanov et al., 2007) with FE modeling of internal tissue strains. This approach opens the door to address a number of questions about acute strain injury in the context of a task that's a known condition for injury—high-speed running. This framework was used to address why muscle is more susceptible to injury at faster sprinting speeds, showing that increased muscle activation at faster speeds is primarily responsible for larger local tissue strain and increased strain injury susceptibility.

Morphological variability influence during sprinting

Musculotendon variability between subjects has been well established by cadaveric studies and the *in vivo* results of this work; however, the impact of musculotendon variability had never been assessed in the context of high-speed running. The importance of musculotendon architecture was demonstrated by varying the dimensions of the BFlh over a physiological range and simulating internal tissue strains during running at maximum speed. This study was the first to show that the BFlh's architecture, namely the width of the proximal aponeurosis relative to the muscle, influences the muscle's strain injury susceptibility. The idea that musculotendon architecture can influence its strain injury susceptibility applies not only to the BFlh but potentially to every muscle-tendon unit in the body. For example, the rectus femoris on the anterior surface of thigh has a relatively narrow superficial aponeurosis and a wider deep aponeurosis. The rectus femoris also suffers injury frequently during high-speed sports (Kassarjian et al., 2012).

6.2 Future applications

The *in vivo* experimentation and computational modeling framework presented in this dissertation open up multiple new and exciting potential projects for exploration. Many unanswered questions remain that can be explored with new *in vivo* imaging techniques and advanced computational methods. A summary of these studies is included below, including preliminary data when available.

Prospective study

Prospective studies are the gold standard for confirming the role of an intrinsic factor on strain injury susceptibility. Drawing on our collaborations with the athletic training department, a prospective study would determine the predictive capability of measuring an athlete's musculotendon dimensions. This will determine whether the BFlh's proximal aponeurosis width can be used as the sole source of identifying athletes with an elevated risk for strain injury susceptibility. The proximal aponeurosis width should be studied in conjunction with other proposed factors, such that results will strengthen the overall knowledge of predictive factors in strain injury susceptibility instead of highlighting an isolated cause. Regardless of the outcome of the prospective study, the relative dimensions of the proximal aponeurosis has been shown to have an influential role on internal muscle tissue strains and hamstrings strain injury susceptibility.

Diffusion tensor imaging of the BFlh muscle

Diffusion tensor (DT) imaging provides an *in vivo* measurement of fiber direction (Heemskerk and Damon, 2007). Applications to skeletal muscle have traditionally suffered from low signal and image artifacts. A custom sequence was procured from the MR manufacturer, Siemens, to image the track and field athletes (Porter and Heidemann, 2009). Despite many attempts at troubleshooting the sequence, the custom sequence was not able to remove a fat shift artifact into the muscle and yield convincing results in the BFlh (Figure 6.1). Future investigation using DT imaging in muscle will work to remove this artifact and use fiber reconstructions to aid in musculotendon measurements and to compare DT results from different populations (e.g., athletes with and without injury).

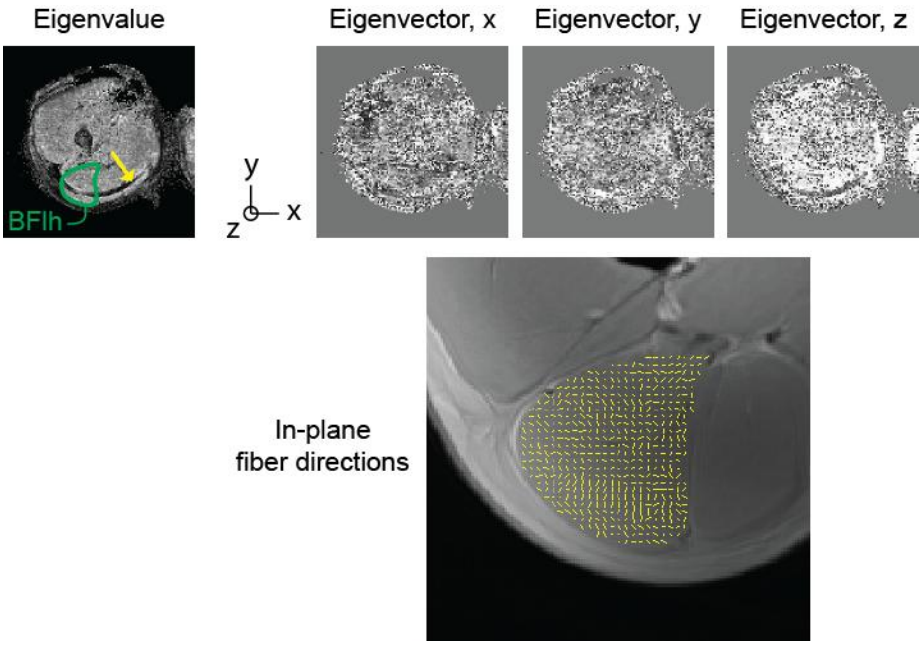

Figure 6.1. Diffusion tensor images and reconstructions

Diffusion tensor imaging measures water diffusion in a number of orthogonal directions (N = 10 in this data set). At each pixel, diffusion measurements are combined into a tensor. The tensor is diagonalized, and the 1st principal diffusion direction is assumed to be along the muscle fiber's axis (Eigenvalue, top left) (Basser et al., 1994). The Eigenvalue image demonstrates the large fat shift artifact (arrow). The eigenvector corresponding to the 1st principal diffusion direction (top, right) can be combined at each pixel for a measurement of fiber direction (bottom).

Three-dimensional dynamic imaging of the hamstrings complex

The fact that the BFlh is injured more often than the other two hamstrings muscles has yet to be explained on the local muscle tissue level. To test the feasibility of acquiring a three-dimensional DENSE data set in muscle tissue, a pilot data set was acquired covering a large volume (250 x 250 x 100 mm^3) of the thigh during dynamic knee motion. The data acquisition required over 20 minutes of exercise, but it yielded a three-dimensional data set where each pixel had x, y and z displacement defined over time (10 dimensions total). Furthermore, by simultaneously acquiring data from all three hamstrings, there will not be any errors associated with comparing measurements from

different trials. Three-dimensional data also rules out disadvantages from picking a single two-dimensional imaging plane.

The pilot measurements demonstrate the feasibility of the three-dimensional muscle tissue measurement approach; for example, the relative displacements in the hamstrings and quadriceps were consistent with their protagonist-antagonist muscle action (Figure 6.2) (Fiorentino et al., 2009). Further processing is required to yield three-dimensional strain distributions throughout the hamstring muscles. If the BFlh undergoes larger peak local strain than the other two hamstrings muscles, this will provide an explanation for its higher strain injury susceptibility than the other two hamstring muscles. If not, these data will point to a different mechanism for the BFlh's higher acute strain injury susceptibility during lengthening contractions.

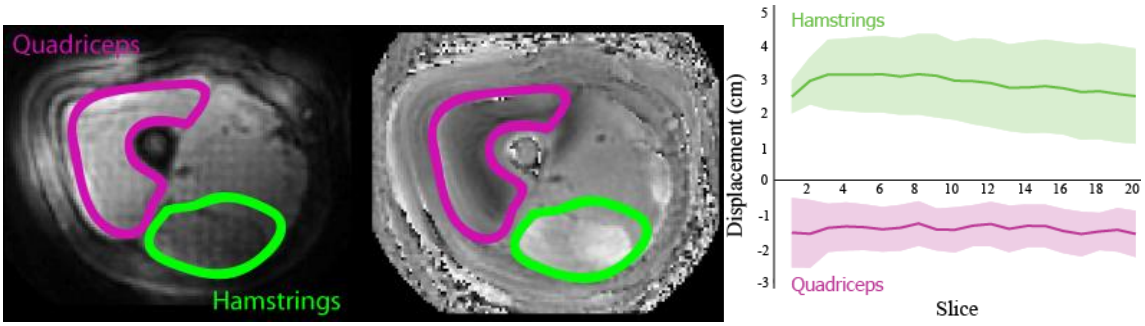

Figure 6.2. Three-dimensional displacements in the quadriceps and hamstrings
The quadriceps and hamstrings were imaged over a large volume (250 x 250 x 100 mm^3) in the thigh during dynamic knee joint motion. The image on the left is a magnitude image where pixel intensity is proportional to water content. The image on the right is a phase image where pixel intensity is proportional to through-plane displacement. Displacement measurements were averaged at each slice location over the imaging volume (graph), and the displacement measurements in opposing directions confirm that the imaging sequence is tracking muscle tissue displacements in a protagonist-antagonist muscle groups.

FE modeling of all three hamstring muscle-tendon units

The three-dimensional strain measurements discussed above provide a powerful means for comparing internal tissue strains during active lengthening and for validating FE model predictions of local tissue strains; however, dynamic imaging does not allow for investigation of higher loads such as those encountered during sprinting. Finite element models of the three hamstrings muscle-tendon units can predict the amount of muscle tissue strain experienced during sprinting. Furthermore, FE models can account for differences in musculotendon morphology by applying the same boundary condition to all three hamstrings muscle-tendon units. Applying the same activation and MTU strain would show how much of the difference in muscle tissue strains is accounted for by differences in morphology alone.

FE modeling of neuromuscular coordination patterns

Recent studies have pointed to neuromuscular coordination changes as the cause of increased strain injury susceptibility in injured athletes (Opar et al., 2012). The FE modeling framework presented in this dissertation has the potential to test this hypothesis. Finite element simulation boundary conditions incorporate changes in muscle activation and muscle-tendon length change that may accompany recovery from acute strain injury, though more experimental data are necessary to accurately simulate changes in neuromuscular coordination patterns following injury. Furthermore, the FE modeling framework presented here can test the effects of changing neuromuscular patterns after training on internal tissue strains during sprinting.

FE modeling of internal proximal aponeurosis projections

A number of imaging subjects exhibited a peculiarity that has not been reported by previous studies—the BFlh's proximal aponeurosis appears to have a projection into the muscle (6.3). Close inspection of excised BFlh muscle-tendon units in cadaver studies suggests that an internal connective tissue structure may be present (Chleboun et al., 2001; Kellis et al., 2012). The inclusion a projection into the muscle was not demonstrated, because only images of the surface or longitudinal cross sections were available. The influence of this projection on internal muscle tissue strains has yet to be determined. Finite element models can incorporate this structure into the morphology of the BFlh muscle-tendon unit and compare muscle tissue strains with and without the projection. The projection could reduce strain injuries in the BFlh by mitigating high tissue strains, or it might be an additional contributing factor to the BFlh's injury susceptibility by increasing tissue strain in the region adjacent to the proximal aponeurosis.

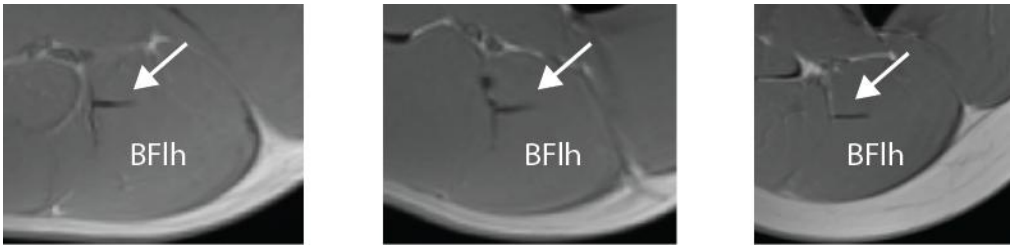

Figure 6.3. Proximal aponeurosis projection

Cropped images of the BFlh from three different athletes show a projection of the proximal aponeurosis into the muscle (arrow). The projection is identified as low intensity signal extending from the proximal aponeurosis into muscle tissue. In these images, the projection is oriented left to right, or medial to lateral.

6.3 Limitations

The methodology and analyses presented in this dissertation contain a few noteworthy limitations that should be taken into consideration when interpreting the data contained herein. The image acquisition in Chapter 3 produces measurements of two-dimensional Lagrangian strain. Three-dimensional tissue strain measurements could alter the relationships between local tissue strain and muscle activation / musculotendon morphology. However, a three-dimensional strain analysis requires three-dimensional image acquisition, and a three-dimensional image acquisition can take as long as 20 minutes of exercise in the scanner (Fiorentino et al., 2009). This amount of exercise could introduce effects of fatigue that would cause inconsistent repetitions and subsequent imaging artifacts. Future work is required to test the amount of variability that accompanies 20 minutes of exercise in a MR scanner.

The lack of time dependence in the constitutive formulation presents a potential limitation to the modeling framework. The force-velocity relationship of muscle would increase the amount of stress during lengthening contractions and modulate the strain magnitude experienced by muscle, but the increases with sprinting speed and variable musculotendon morphology would not necessarily change. Increases in local tissue strain with variable musculotendon morphology were caused by larger longitudinal cross-sectional area in the middle of the muscle compared to near the proximal MTJ, which would likely not change if force-velocity was included. To explore the effect of higher activation at faster sprinting speed, two stress-stretch curves were generated with different levels of activation (Figure 6.4). The plots show that the slope of the total length curve decreases with increasing activation, demonstrating that for a given stress

increase (σ') muscle stretches (λ') more (28%) at higher activation. Force-velocity would likely alter the relative increase; however, because force-velocity will change the stress at all levels of stress, the slope of the total length curve may or may not change substantial. Therefore, the increase of local tissue strain may or may not be affected.

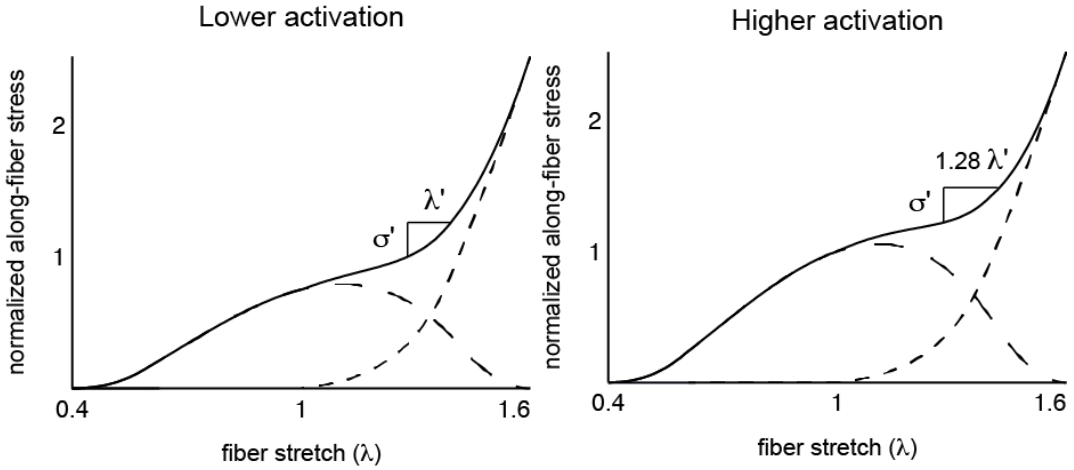

Figure 6.4. Activation level dependent stress-stretch plots

Stress-stretch plots were generated to help explain muscle tissue's increased stretch at higher activation levels. Force-velocity would alter the stress-stretch relationship by increasing stress at all levels of stretch, but the relative increase in stretch from an increase stress may or may not change. σ': stress. λ': stretch

In addition, the time-dependence, or strain rate, of connective tissue was not included in the formulation. A stiffer tendon at high strain rates would likely strengthen the arguments presented here, because tendon stiffness was shown to increase local tissue strain in the sensitivity analysis presented in Chapter 4. Moreover, the stiffness of tendon and aponeurosis was set to a value derived from experiments at 1.4 Hz, which was only slightly below the stride frequency of running at high-speeds (2.2 – 4.5 Hz, see A.2 below). Lastly, viscoelastic terms were not included in the constitutive formulation,

which would have required considerable changes to the material model and a new set of parameters that are not available in the literature for transversely isotropic materials.

The inability to compare strain values to an injury risk relationship in humans represents another source of limitation. The conclusions of the work presented in this dissertation utilize relationships that were derived based on animal models of injury, where increases in strain are directly related to increases in strain injury susceptibility. Animal models of injury established a direct connection between strain injury magnitude and resultant injury (Brooks and Faulkner, 2001; Lieber and Friden, 1993; Noonan et al., 1994). Furthermore, animal models of injury have measured tissue injury at the location of largest local tissue strain (Best et al., 1995). On the other hand, strain injury studies in humans have observed injury only twice during sprinting gait data acquisition, where one study speculated that excessive strain might have been the cause (based on increased knee extension earlier in the swing phase) without providing quantitative strain data (Schache et al., 2009), and the second study found that muscle-tendon unit length was not significantly longer compared to the preceding non-injurious strides (Heiderscheit et al., 2005).

The extension of strain injury measurements in animal models of injury to human injury risk is not necessarily straightforward. Difficulties exist due to differences in muscle-tendon architecture and the magnitude of muscle-tendon unit strain. The amount of muscle-tendon unit strain that was measured during the injurious sprinting gait study was 12% greater than the hamstring length relative to standing upright (Heiderscheit et al., 2005); however, the amount of strain necessary for injury during active muscle-tendon unit strain in animal models has been inconsistent and has generally required

larger amounts of strain (e.g., 15% in Hasselman et al. (1995) and 30% in Brooks et al. (1995)). For local strain measurements, the value for injury was measured at 61% (Best et al., 1995); however, this value was measured on the surface of a fusiform muscle-tendon unit (the tibialis anterior of rabbits) and, despite the claim of the authors, represents only linear strain along the direction of the fiber. Other studies have shown a direct dependence of strain injury on muscle-tendon architecture (Garrett et al., 1988), where fusiform (i.e., paralleled fiber geometry with no pennation angle) muscle-tendon units showed a lower strain injury threshold than pennate (i.e., fiber direction at an angle compared to the tendon) muscle-tendon units. This suggests that quantitative data from fusiform muscle-tendon units, such as the tibialis anterior, which dominate the strain injury literature due to the muscle-tendon unit's accessibility in animals and regular geometry, may not be directly applicable to the more complicated pennate-structured biceps femoris long head in humans.

To better connect the BFlh muscle's strain injury susceptibility in humans to animal studies, future studies should utilize more recent *in vivo* testing procedures incorporating active lengthening in animal models of injury (Butterfield and Herzog, 2005). Moreover, testing should be performed on pennate muscle-tendon units rather than parallel-fibered muscle tendon units, and protocols should mimic the amount of muscle-tendon unit strain observed during sprinting gait. With more direct, *in vivo* measurements of strain in animal models of injury, the amount of local strain experienced by muscle during running at high-speed, as predicted by the FE models in this dissertation, can be better placed in the context of strain injury risk.

6.4 Summary

Any athlete participating in a high-speed sport is at-risk for an acute muscle strain injury. Despite decades of in-depth research, strain injury remains a prevalent problem in athletics at all levels. Previous research has focused on associating extrinsic and intrinsic factors with injury; however, this approach has done little to provide insight into the factors that cause injury and what makes an individual more susceptible to injury. The impact of this work is that the muscle injured most often, the BFlh, is studied *in vivo* and in the context of when the muscle is most susceptible to injury, active lengthening. To study the BFlh during high-speed running, which is not possible with current *in vivo* imaging technology, finite element modeling predicted internal tissue strains allowing us to answer previously unaddressed questions about acute strain injury.

The insights gained with the work presented in this dissertation have a broad impact on the field of acute strain injury. Increased local tissue strain provides an explanation for why the BFlh muscle is more susceptible to injury during active lengthening. Moreover, increased tissue strain while running at faster speeds provides an explanation for why athletes are injured in high-speed sports. In addition, connecting the BFlh's architecture with its strain injury susceptibility provides insight into why this muscle is injured so often and why some individuals might be injured and not others. With a better understanding of the mechanics behind acute muscle strain injury, clinicians and trainers can design training and rehabilitation programs aimed at reducing acute strain injury.

Appendices

The purpose of these appendices is to expand on the description of the imaging methods, including image acquisition, image analysis and strain calculation, as well as to describe in more detail the process by which the models were generated and analyzed. In addition, limitations to the methodology, analyses and conclusions are discussed.

A.1 DENSE imaging and strain analysis

The displacement encoding with stimulated echoes (DENSE) technique measures tissue displacement at a pixel-wise spatial resolution during motion. The technique was originally developed to measure cardiac displacement and strain at a single point in time (e.g., end systole) (Aletras et al., 1999) and has been more recently extended to include multiple time frames (i.e., a cine acquisition) (Kim et al., 2004). The advanced developments of the DENSE sequence have been accomplished by Professor Epstein's lab at the University of Virginia, where recent developments have lowered the number of triggers necessary to acquire a set of images (by incorporated a spiral acquisition), improved the signal-to-noise, and reduced the amount of phase error (Zhong et al., 2009).

The theory behind the DENSE MR signal has been described previously and will be the basis for the description here (Kim et al., 2004). The DENSE image acquisition is initiated by an external trigger, which for cardiac imaging is an ECG and for the work presented here was a square-wave pulse from the LabView program mentioned in Chapter 3. After initiation, an encoding gradient modulates the magnetization by a cosine function, which, according Fourier transform rules, creates two echoes in the spatial-frequency domain. After allowing for tissue motion, an unencoding gradient (of

the same area as the encoding gradient) precedes the readout gradient (i.e., signal acquisition), such that the displacement is encoded directly into the phase of the MR signal of the first echo in the spatial-frequency domain (see derivation in the appendix of (Kim et al., 2004)). The output of the DENSE imaging sequence is the magnitude and phase of the signal at each pixel, where the magnitude reconstructed images show the anatomy and the phase reconstructed images are measures of displacement in each direction (Figure A.1).

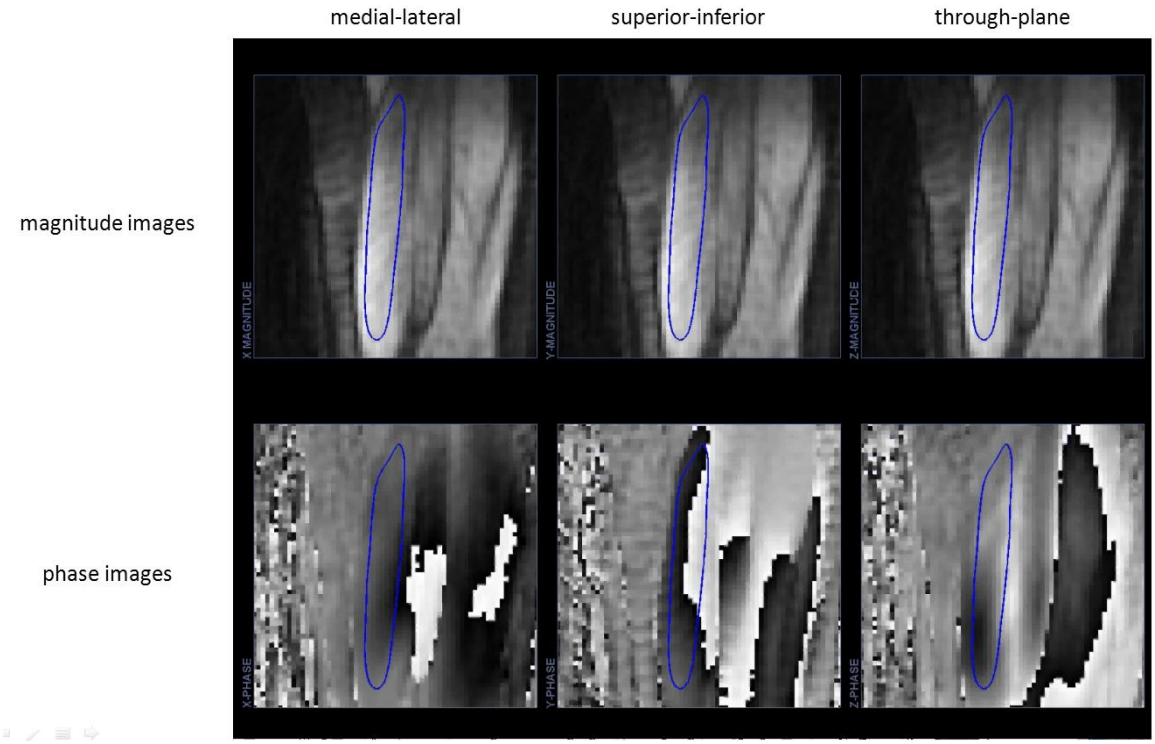

Figure A.1. DENSE images

The DENSE imaging sequence produces a magnitude image (top row) and phase image (bottom row) at each time point during the motion. The BFlh region-of-interest is indicated by a blue line outlining the muscle. The intensity of phase images is proportional to tissue displacement. Displacement measurements were acquired in three directions—i) medial lateral, or left-right in the image; ii) superior-inferior, or up-down; and iii) through-plane, or into and out of the page.

The DENSE images are analyzed for tissue displacement and strain with the methods of Spottiswoode et al. (2007). This was performed with in-house Matlab software DENSEanalysis. The first step in the image analysis process is to unwrap any pixels that have aliased from $2\pi^+$ to 0. Phase wrapping occurs because the displacement encoding gradient is set low enough to provide a high displacement resolution, which in turn means that a relatively lower amount of displacement is necessary to cover the range of phase values available before wrapping. Second, the unwrapped phase images are converted to displacement measurements, where displacement = phase / (2π k_e), and k_e = encoding frequency in radians per mm. At this point, all time frames have a pixel-wise measurement of displacement.

To isolate the biceps femoris long head, a region-of-interest (ROI) is drawn around the muscle on the magnitude image for the first time frame, and the points defining the ROI are displaced based on the tissue displacement measurements on later time frames. At this point in the analysis, the ROI is defined to enclose the BFlh on all time frames. To produce a material description of tissue position, which is necessary for Lagrangian strain calculation, the pixels inside the ROI on all frames are mapped back to the original time frame using the displacement measurements. The location of all the pixels within the BFlh ROI on the first time frame is found on later time frames by interpolating between all of the pixels displacements mapped from later time frames. After this process is complete, the location of all the pixels in the first time frame are known for all time frames, or a material description of tissue displacement is known (Figure 3.3).

The measurements of tissue displacement are used to define a deformation gradient at each pixel and subsequently calculate a Lagrangian strain tensor. The location of neighboring pixels is used to define a deformation gradient, F (Figure A.2). The deformation gradient is found by taking into account the relative position of neighboring pixels on the first time frame and at all later time frames. In the schematic in Figure A.2, the deformation gradient is calculated for a pixel, C, which is at the center of four nearest neighbors, U (upper), R (right), L (left) and D (down). Combining the x and y vectors components into a matrix yields a 2x2 matrix for the initial time frame (Time 0) and later times (Time t), and dividing the later time by the initial time yields a deformation gradient. Because the image analysis was restricted to a single imaging plane, only a two-dimensional strain analysis was possible. This process is repeated for all of the nearest neighbors that are present and averaged for a deformation gradient at that pixel's location. Lagrangian strain is then calculated with the standard definition, $E = \frac{1}{2}(F^{T}F–I)$, where I is the identity tensor. Lagrangian strain tensors were diagonalized for principal strains, and the first principal strain was defined as the most positive eigenvalue.

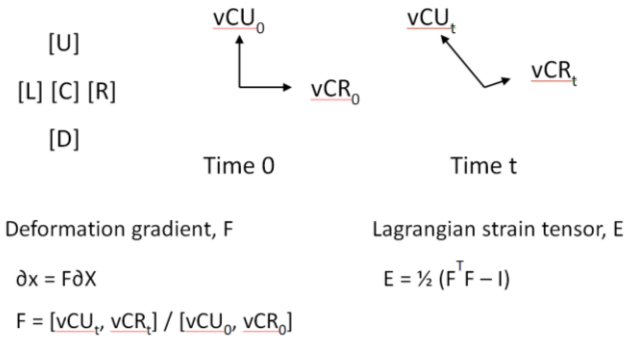

Figure A.2. Strain calculation schematic

A schematic for calculating strain shows how the deformation gradient, F, was found at each pixel, based on the relative position of neighboring pixels (U: upper, L: left, R: right, D: down). The deformation gradient was used to calculate Lagrangian strain tensor, E.

A.2 Computational model framework

The computational modeling framework presented in this dissertation permits internal tissue strain predictions during sprinting. As inputs, the modeling framework requires the geometry of the FE mesh, the fiber direction at each element throughout the mesh, the constitutive model (including material parameters), muscle activations and muscle-tendon length change (Figure A.3). The output of the modeling process is predictions of internal tissue strain. Given that animal models of injury have directly correlated strain magnitude and high local strain concentration with injury (Brooks and Faulkner, 2001; Lieber and Friden, 1993; Noonan et al., 1994), the amount of strain experienced with increasing sprinting speed and with varying musculotendon dimensions was associated with changes in strain injury susceptibility.

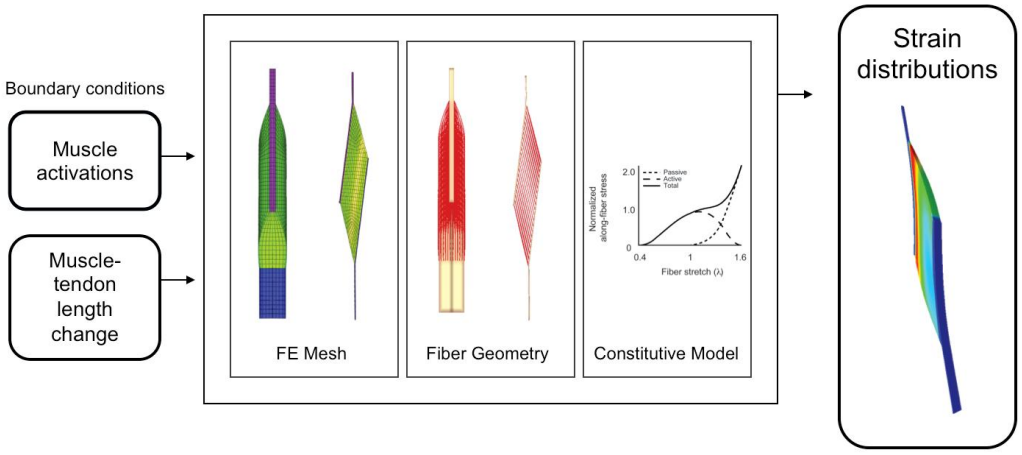

Figure A.3. Computational modeling framework

The computational modeling framework incorporated musculotendon dimensions measured on MR images, fiber directions determined from a fiber mapping procedure and a transversely isotropic, hyperelastic material model. Boundary conditions for the simulations were muscle activation and muscle-tendon length change. The output for the simulations was local strain distribution throughout the muscle.

The first step in this process is to define the geometry of the FE mesh, which was based on musculotendon measurements on high-resolution axial MR images. As explained in Chapters 4 and 5, measurements were acquired for three structures—the proximal tendon and aponeurosis (1), the muscle (2) and the distal tendon and aponeurosis (3). The tendon and aponeurosis were considered one structure, where the difference the two was that muscle fibers originated on aponeurosis and tendon was free of muscle fibers. Measurements of width and thickness were acquired directly on the axial images, while length measurements were derived from identifying the beginning and end of structures and the inter-slice distance between images.

The FE mesh was generated using TrueGrid software (XYZ Scientific Applications) and consisted of hexahedral elements. The exact number of elements was determined after a convergence study of element number. In addition, the mesh quality was used as a determining factor for the way in which the mesh was generated in TrueGrid. The technique used in the studies presented in this dissertation began with a long rectangular block, and the corners of the block were immediately removed to allow for a butterfly mesh in the tapering regions. The middle of the muscle in between the tapering regions remained rectilinear, which improved mesh quality relative to previous modeling procedures for the BFlh. The computational block in TrueGrid was projected to a series of splines defining the dimensions of the three BFlh structures, and, as a last step, was projected to a surface on the outer surface of the muscle.

A transversely isotropic, hyperelastic quasi-incompressible material model was used for muscle and connective tissue (including tendon and aponeurosis). The material

model requires a fiber direction as an input. For muscle, the fiber direction was defined using a previously published fiber mapping technique (Blemker and Delp, 2005). The fiber mapping procedure makes meshes of higher quality and more regular element shapes available for use even though the elements do not align with the direction of muscle fibers. The fiber mapping technique requires three files—the FE mesh with the desired element configuration (desired mesh), a FE mesh with same geometry as (1) but the element direction coincides with the fiber direction (overlay), and an undeformed computational block with the same number of elements as the FE mesh with the coincident element and fiber directions (computational block).

The mesh with the fiber directions along the element direction is overlaid onto the mesh with the desired dimensions. The computational block initially has a regular cubic geometry of unit size and fibers running from one face to the opposite face. The computational block is mapped onto the mesh with the coincident fiber and element directions (the overlay mesh). Given that the desired mesh and the overlay mesh have the same geometry, mapping the computational block onto the overlay mesh produces a mathematical relationship between the computational block with known fiber directions and the mesh with the desired element configuration. The mapping procedure produces a fiber direction defined at each element in the desired mesh, which is an input into the constitutive formulation.

The constitutive formulation for all materials was transversely isotropic, hyperelastic and quasi-incompressible. The formulation was originally developed by Weiss et al. (1996) for use with ligaments and was extended by Criscione et al. (2001) to include strain invariants with physiological relevance. Blemker et al. (2005) extended

this formulation by adding active muscle contraction and developing a framework for studying large three-dimensional deformations of complex three-dimensional musculotendon structures. In the strain energy density term for along-fiber extension, an active stress term was added to the formulation to account for the stress generated due to muscle activation. The amount of active muscle stress was based on muscle fiber's stress-strain relationship, which is based on the well-known force-length curve for muscle (Zajac, 1989). The active stress-strain curve is defined explicitly by the amount of peak isometric stress and the stretch at which peak isometric stress is achieved. The peak isometric stress value used in these studies was based on mechanical tests in isolated and permealized fibers from human vastus lateralis muscle biopsies (Shoepe et al., 2003). The active stress-stretch curve is linearly modulated by the amount of muscle activation and is added to the passive stress-stretch curve for the total amount of stress at different levels of stretch.

For connective tissues, including tendon and aponeurosis, the formulation is the same as muscle, but there is no muscle activation term and the material parameters are stiffer. The material properties for tendon were defined based on mechanical tests of patellar tendon specimens from cadavers (Chandrashekar et al., 2012). The tests consisted of many stretch-shorten cycles at 1.4 Hz. The numbers in these models were derived from stress-strain curves at steady-state, or after many stretch-shorten cycles. It should be noted that the subjects in the sprinting studies from which boundary conditions were derived were running at approximately 3.2-4.5 Hz, where the range represents variation in the maximum running speed of the subjects. The stride frequency of subjects in the sprinting studies was not explicitly reported (Chumanov et al., 2007), but was

instead derived from a study of Olympic athletes running at approximately 4-5 Hz at a speed of 10 m/s (Salo et al., 2011). The stride frequency of Olympic runners was modulated by the running speed of the subjects in the sprinting study divided by the running speed of the athletes. Subjects sprinting at sub-maximal speeds would have a lower stride frequency closer to the frequency used for mechanical tests (e.g., 2.2-3.2 Hz at 70% maximum speed).

A convergence analysis was performed to determine the optimal number of elements in the FE model. Element density was varied by two orders of magnitude, and the average amount of along-fiber strain near the proximal aponeurosis was used as the output parameter. A mesh with 2960 elements was chosen for further analysis, because it had the best mesh quality with regularly-shaped elements and it was close to the converged value for the output parameter (89%). Elements were added to the mesh in chapter 5 (3900 total elements) to accommodate the more complicated geometry, in that variation in the superior-inferior direction was included when assessing the influence of musculotendon variability. For all models and all materials, hexahedral elements were used. Mesh quality was assessed using TrueGrid's measure function, where elements with skewed aspect ratios or a volume far from than the median were addressed prior to simulation.

Simulations were performed with Nike3d on an 8-node Linux cluster (Puso et al., 2007). Simulations typically required two or three minutes to converge. For simulations that did not converge successfully, the reason was negative hex volume detection. Locking or hourglassing was never encountered. To improve convergence, the mesh quality was defined to include a butterfly mesh in the tapering regions and a rectilinear

block in between (as opposed to a block displaced inferiorly on one side to yield a pennate structure, which results in elements with a poor aspect ratio). Simulation convergence was also improved by incorporating recent mechanical tests of muscle tissue (Morrow et al., 2010). The relatively stiffer shear moduli prevented excessive strain and negative element volume, given that muscle-tendon unit lengthening in the pennate BFlh is predominantly a shearing deformation. Increasing the bulk modulus of muscle also had a significant improvement on simulation convergence.

The output of simulations was along-fiber stretch at each element, which was visualized and qualitatively analyzed with PostView software (Maas et al., 2010). Quantitative analysis of local strain was performed in Matlab after points along all representative fibers were tracked throughout the simulation. The fiber mapping procedure outlined above provides not only fiber direction at each element but also a set of representative muscle fibers throughout the BFlh. Points were evenly distributed along each representative fiber, and the points were tracked during the simulation using nodal displacements. Local strain was calculated with an engineering strain definition, where local strain was defined as the inter-point distance at each step in the simulation minus the original distance divided by the original distance. Local strains were used to generate all the results in Chapters 4 and 5 except the qualitative description of along-fiber strain and the comparison between imaging (which measured 1^{st} principal strain) and modeling.

References

Aletras, A. H., Ding, S. J., Balaban, R. S., Wen, H., 1999. DENSE: Displacement encoding with stimulated echoes in cardiac functional MRI. Journal of Magnetic Resonance 137, 247-252.

Alonso, J., Edouard, P., Fischetto, G., Adams, B., Depiesse, F., Mountjoy, M., 2012. Determination of future prevention strategies in elite track and field: analysis of Daegu 2011 IAAF Championships injuries and illnesses surveillance. British Journal of Sports Medicine 46, 505-514.

An, X. C., Lee, J. H., Im, S., Lee, M. S., Hwang, K., Kim, H. W., Han, S. H., 2010. Anatomic localization of motor entry points and intramuscular nerve endings in the hamstring muscles. Surgical and Radiologic Anatomy (English Ed.) 32, 529-537.

Arnason, A. A., Andersen, T. E., Holme, I., Engebretsen, L., Bahr, R., 2008. Prevention of hamstring strains in elite soccer: an intervention study Prevention of hamstring strains in soccer. Scandinavian Journal of Medicine & Science in Sports 18, 40-48.

Askling, C., Karlsson, J., Thorstensson, A., 2003. Hamstring injury occurrence in elite soccer players after preseason strength training with eccentric overload. Scandinavian Journal of Medicine & Science in Sports 13, 244-250.

Askling, C. M., Tengvar, M., Saartok, T., Thorstensson, A., 2007. Acute first-time hamstring strains during high-speed running: a longitudinal study including clinical and magnetic resonance imaging findings. The American Journal of Sports Medicine 35, 197-206.

Bahr, R., Holme, I., 2003. Risk factors for sports injuries -- a methodological approach. British Journal of Sports Medicine 37, 384-392.

Basser, P. J., Mattiello, J., LeBihan, D., 1994. MR diffusion tensor spectroscopy and imaging. Biophysical Journal 66, 259-267.

Bennell, K., Tully, E., Harvey, N., 1999. Does the toe-touch test predict hamstring injury in Australian Rules footballers? Australian Journal of Physiotherapy 45, 103-109.

Bennell, K. L., Crossley, K., 1996. Musculoskeletal injuries in track and field: incidence, distribution and risk factors. Australian Journal of Science and Medicine in Sport 28, 69-75.

Best, T. M., Shehadeh, S. E., Leverson, G., Michel, J. T., Corr, D. T., Aeschlimann, D., 2001. Analysis of changes in mRNA levels of myoblast- and fibroblast-derived gene products in healing skeletal muscle using quantitative reverse transcription-polymerase chain reaction. Journal of Orthopaedic Research 19, 565-572.

Best, T., McElhaney, J., Garrett, W., Myers, B., 1995. Axial strain measurements in skeletal muscle at various strain rates. Journal of Biomechanical Engineering 117, 262-265.

Blankenbaker, D. G., Tuite, M. J., 2010. Temporal changes of muscle injury. Seminars in Musculoskeletal Radiology 14, 176-193.

Blemker, S. S., Asakawa, D. S., Gold, G. E., Delp, S. L., 2007. Image-based musculoskeletal modeling: Applications, advances, and future opportunities. Journal of Magnetic Resonance Imaging 25, 441-451.

Blemker, S. S., Delp, S. L., 2005. Three-dimensional representation of complex muscle architectures and geometries. Annals of Biomedical Engineering 33, 661-673.

Blemker, S. S., Pinsky, P. M., Delp, S. L., 2005. A 3D model of muscle reveals the causes of nonuniform strains in the biceps brachii. Journal of Biomechanics 38, 657-665.

Brooks, J. H. M., Fuller, C. W., Kemp, S. P. T., Reddin, D. B., 2005. Epidemiology of injuries in English professional rugby union: part 1 match injuries. British Journal of Sports Medicine 39, 757-766.

Brooks, J. H. M., Fuller, C. W., Reddin, D. B., 2006. Incidence, risk, and prevention of hamstring muscle injuries in professional rugby union. American Journal of Sports Medicine 34, 1297-1306.

Brooks, S. V., Faulkner, J. A., 2001. Severity of contraction-induced injury is affected by velocity only during stretches of large strain. Journal of Applied Physiology 91, 661-666.

Brooks, S. V., Zerba, E., Faulkner, J. A., 1995. Injury to muscle fibers after single stretches of passive and maximally stimulated muscles in mice. Journal of Physiology 488, 459-469.

Butterfield, T. A., Herzog, W., 2005. Quantification of muscle fiber strain during in vivo repetitive stretch-shortening cycles. Journal of Applied Physiology 99, 593-602.

Butterfield, T. A., 2010. Eccentric exercise in vivo: strain-induced muscle damage and adaptation in a stable system. Exercise and Sport Sciences Reviews 38, 51-60.

Cameron, M., Adams, R., Maher, C., 2003. Motor control and strength as predictors of hamstring injury in elite players of Australian football. Physical Therapy in Sport 4, 159-166.

Carr, J. A., Ellerby, D. J., Marsh, R. L., 2011. Differential segmental strain during active lengthening in a large biarticular thigh muscle during running. Journal of Experimental Biology 214, 3386-3395.

Chandrashekar, N., Slauterbeck, J., Hashemi, J., 2012. Effects of cyclic loading on the tensile properties of human patellar tendon. Knee 19, 65-68.

Chleboun, G. S., France, A. R., Crill, M. T., Braddock, H. K., Howell, J. N., 2001. In vivo measurement of fascicle length and pennation angle of the human biceps femoris muscle. Cells Tissues Organs 169, 401-409.

Chumanov, E. S., Heiderscheit, B. C., Thelen, D. G., 2007. The effect of speed and influence of individual muscles on hamstring mechanics during the swing phase of sprinting. Journal of Biomechanics 40, 3555-3562.

Chumanov, E. S., Schache, A. G., Heiderscheit, B. C., Thelen, D. G., 2012. Hamstrings are most susceptible to injury during the late swing phase of sprinting. British Journal of Sports Medicine 46, 90.

Clanton, T. O., Coupe, K. J., 1998. Hamstring strains in athletes: diagnosis and treatment. Journal of the American Academy of Orthopaedic Surgeons 6, 237-248.

Conn, J. M., Annest, J. L., Gilchrist, J., 2003. Sports and recreation related injury episodes in the US population, 1997-99. Injury Prevention 9, 117-123.

Criscione, J. C., Douglas, A. S., Hunter, W. C., 2001. Physically based strain invariant set for materials exhibiting transversely isotropic behavior. Journal of the Mechanics and Physics of Solids 49, 871-897.

Croisier, J. L., 2004. Factors associated with recurrent hamstring injuries. Sports Medicine 34, 681-695.

Croisier, J. L., Ganteaume, S., Binet, J., Genty, M., Ferret, J. M., 2008. Strength Imbalances and Prevention of Hamstring Injury in Professional Soccer Players: A Prospective Study. The American Journal of Sports Medicine 36, 1469-1475.

Damon, B. M., Ding, Z., Anderson, A. W., Freyer, A. S., Gore, J. S., 2002. Validation of diffusion tensor MRI-based muscle fiber tracking. Magnetic Resonance in Medicine 48, 97-104.

De Smet, A. A., Best, T. M., 2000. MR imaging of the distribution and location of acute hamstring injuries in athletes. American Journal of Roentgenology 174, 393-399.

Dixon, W., 1984. Simple Proton Spectroscopic Imaging. Radiology 153, 189-194.

Ekstrand, J., Hagglund, M., Walden, M., 2009. Injury incidence and injury patterns in professional football: the UEFA injury study. British Journal of Sports Medicine.

Ekstrand, J., Hagglund, M., Walden, M., 2011. Epidemiology of Muscle Injuries in Professional Football (Soccer). American Journal of Sports Medicine 39, 1226-1232.

Elliott, M. C. C. W., Zarins, B., Powell, J. W., Kenyon, C. D., 2011. Hamstring muscle strains in professional football players a 10-year review. American Journal of Sports Medicine 39, 843-850.

Englund, E. K., Elder, C. P., Xu, Q., Ding, Z., Damon, B. M., 2011. Combined Diffusion and Strain Tensor MRI Reveals a Heterogeneous, Planar Pattern of Strain Development during Isometric Muscle Contraction. American Journal of Physiology Regulatory, Integrative and Comparative Physiology.

Feeley, B. T., Kennelly, S., Barnes, R. P., Muller, M. S., Kelly, B. T., Rodeo, S. A., Warren, R. F., 2008. Epidemiology of National Football League training camp injuries from 1998 to 2007. American Journal of Sports Medicine 36, 1597-1603.

Fernandez, J. W., Hunter, P. J., 2005. An anatomically based patient-specific finite element model of patella articulation: towards a diagnostic tool. Biomechanics and Modeling in Mechanobiology 4, 20-38.

Fiorentino, N. M., Blemker, S. S., 2013. Computation models predict larger muscle tissue strains at faster sprinting speeds. Medicine & Science in Sports & Exercise, In review.

Fiorentino, N. M., Zhong, X., Rehorn, M. R., Epstein, F., Blemker, S. S., 2009. Characterizing 3D hamstrings strains using cine DENSE imaging. In International Society of Magnetic Resonance in Medicine. Honolulu, HI.

Fiorentino, N. M., Epstein, F. H., Blemker, S. S., 2012. Activation and aponeurosis morphology affect in vivo muscle tissue strains near the myotendinous junction. Journal of Biomechanics 45, 647-652.

Foreman, T. K., Addy, T., Baker, S., Burns, J., Hill, N., Madden, T., 2006. Prospective studies into the causation of hamstring injuries in sport: A systematic review. Physical Therapy in Sport 7, 101-109.

Fregly, B. J., 2008. Computational Assessment of Combinations of Gait Modifications for Knee Osteoarthritis Rehabilitation. IEEE Transactions on Biomedical Engineering 55, 2104-2106.

Friederich, J. A., Brand, R. A., 1990. Muscle-Fiber Architecture in the Human Lower-Limb. Journal of Biomechanics 23, 91-95.

Fyfe, J. J., Opar, D. A., Williams, M. D., Shield, A. J., 2013. The role of neuromuscular inhibition in hamstring strain injury recurrence. Journal of Electromyography and Kinesiology In press.

Garrett, W. E., 1996. Muscle strain injuries. American Journal of Sports Medicine 24, S2-S8.

Garrett, W. E., Nikolaou, P. K., Ribbeck, B. M., Glisson, R. R., Seaber, A. V., 1988. The effect of muscle architecture on the biomechanical failure properties of skeletal muscle under passive extension. American Journal of Sports Medicine 16, 7-12.

Garrett, W. E., Safran, M. R., Seaber, A. V., Glisson, R. R., Ribbeck, B. M., 1987. Biomechanical comparison of stimulated and nonstimulated skeletal muscle pulled to failure. American Journal of Sports Medicine 15, 448-454.

Hagglund, M., Walden, M., Ekstrand, J., 2013. Risk Factors for Lower Extremity Muscle Injury in Professional Soccer The UEFA Injury Study. American Journal of Sports Medicine 41, 327-335.

Hasselman, C. T., Best, T. M., Seaber, A. V., Garrett, W. E., 1995. A threshold and continuum of injury during active stretch of rabbit skeletal muscle. American Journal of Sports Medicine 23, 65-73.

Heemskerk, A. M., Damon, B. M., 2007. Diffusion tensor MRI assessment of skeletal muscle architecture. Current Medical Imaging Reviews 3, 152-160.

Heiderscheit, B. C., Hoerth, D. M., Chumanov, E. S., Swanson, S. C., Thelen, B. J., Thelen, D. G., 2005. Identifying the time of occurrence of a hamstring strain injury during treadmill running: a case study. Clinical Biomechanics 20, 1072-1078.

Heiderscheit, B. C., Sherry, M. A., Silder, A., Chumanov, E. S., Thelen, D. G., 2010. Hamstring Strain Injuries: Recommendations for Diagnosis, Rehabilitation, and Injury Prevention. The Journal of Orthopaedic and Sports Physical Therapy 40, 67-81.

Higashihara, A., Ono, T., Kubota, J., Okuwaki, T., Fukubayashi, T., 2010. Functional differences in the activity of the hamstring muscles with increasing running speed. Journal of Sports Sciences 28, 1085-1092.

Hoang, P. D., Herbert, R. D., Todd, G., Gorman, R. B., Gandevia, S. C., 2007. Passive mechanical properties of human gastrocnemius muscle-tendon units, muscle fascicles and tendons in vivo. Journal of Experimental Biology 210, 4159-4168.

Hootman, J. M., Macera, C. A., Ainsworth, B. E., Addy, C. L., Martin, M., Blair, S. N., 2002. Epidemiology of musculoskeletal injuries among sedentary and physically active adults. Medicine and Science in Sports and Exercise 34, 838-844.

Hoskins, W., Pollard, H., 2005a. Hamstring injury management--Part 2: Treatment. Manual Therapy 10, 180-190.

Hoskins, W., Pollard, H., 2005b. The management of hamstring injury--Part 1: Issues in diagnosis. Manual Therapy 10, 96-107.

Hunter, D. G., Speed, C. A., 2007. The assessment and management of chronic hamstring/posterior thigh pain. Best Practice & Research.Clinical Rheumatology 21, 261-277.

Jarvinen, T. A. H. J., Jarvinen, T. L. N., Kaariainen, M., Kalimo, A., Jarvinen, M., 2005. Muscle injuries - Biology and treatment. American Journal of Sports Medicine 33, 745-764.

Kassarjian, A., Rodrigo, R. M., Santisteban, J. M., 2012. Current concepts in MRI of rectus femoris musculotendinous (myotendinous) and myofascial injuries in elite athletes. European Journal of Radiology 81, 3763-3771.

Kellis, E., Galanis, N., Natsis, K., Kapetanos, G., 2010. Muscle architecture variations along the human semitendinosus and biceps femoris (long head) length. Journal of Electromyography and Kinesiology : Official Journal of the International Society of Electrophysiological Kinesiology 20, 1237-1243.

Kellis, E., Galanis, N., Kapetanos, G., Natsis, K., 2012. Architectural differences between the hamstring muscles. Journal of Electromyography and Kinesiology 22, 520-526.

Kibler, W. B., 1990. Clinical aspects of muscle injury. Medicine and Science in Sports and Exercise 22, 450-452.

Kim, D., Gilson, W. D., Kramer, C. M., Epstein, F. H., 2004. Myocardial Tissue Tracking with Two-dimensional Cine Displacement-encoded MR Imaging: Development and Initial Evaluation. Radiology 230, 862-871.

Koulouris, G., Connell, D., 2003. Evaluation of the hamstring muscle complex following acute injury. Skeletal Radiology 32, 582-589.

Lansdown, D. A., Ding, Z., Wadington, M., Hornberger, J. L., Damon, B. M., 2007. Quantitative diffusion tensor MRI-based fiber tracking of human skeletal muscle. Journal of Applied Physiology (1985) 103, 673-681.

Leonard, T. R., Herzog, W., 2010. Regulation of muscle force in the absence of actin-myosin-based cross-bridge interaction. American Journal of Physiology-Cell Physiology 43, 3063-3066.

Lieber, R. L., Friden, J., 1993. Muscle damage is not a function of muscle force but active muscle strain. Journal of Applied Physiology 74, 520-526.

Lieber, R. L., Woodburn, T. M., Friden, J., 1991. Muscle damage induced by eccentric contractions of 25% strain. Journal of Applied Physiology 70, 2498-2507.

Lysholm, J., Wiklander, J., 1987. Injuries in Runners. American Journal of Sports Medicine 15, 168-171.

Maas, S., Rawlins, D., Weiss, J., 2010. PostView Finite Element Post Processing. Musculoskeletal Research Laboratories http://mrl.sci.utah.edu/software/postview.

Marshall, S. W., Hamstra-Wright, K. L., Dick, R., Grove, K. A., Agel, J., 2007. Descriptive epidemiology of collegiate women's softball injuries: National Collegiate Athletic Association Injury Surveillance System, 1988-1989 through 2003-2004. Journal of Athletic Training 42, 286-294.

Mendiguchia, J., Brughelli, M., 2011. A return-to-sport algorithm for acute hamstring injuries. Physical Therapy in Sport 12, 2-14.

Morrow, D. A., Donahue, T. L. H., Odegard, G. M., Kaufman, K. R., 2010. Transversely isotropic tensile material properties of skeletal muscle tissue. Journal of the Mechanical Behavior of Biomedical Materials 3, 124-129.

Noonan, T. J., Best, T. M., Seaber, A. V., Garrett, W. E., 1994. Identification of a threshold for skeletal muscle injury. American Journal of Sports Medicine 22, 257-261.

Noonan, T. J., Garrett, W. E., 1999. Muscle strain injury: diagnosis and treatment. Journal of the American Academy of Orthopaedic Surgeons 7, 262-269.

Noonan, T. J., Garrett, W. E., 1992. Injuries at the myotendinous junction. Clinical Sports Medicine 11, 783-806.

Noseworthy, M. D., Davis, A. D., Elzibak, A. H., 2010. Advanced MR Imaging Techniques for Skeletal Muscle Evaluation. Seminars in Musculoskeletal Radiology 14, 257-268.

Opar, D. A., Williams, M. D., Shield, A. J., 2012. Hamstring Strain Injuries Factors that Lead to Injury and Re-Injury. Sports Medicine 42, 209-226.

Orchard, J., Best, T. M., 2002. The management of muscle strain injuries: An early return versus the risk of recurrence. Clinical Journal of Sport Medicine 12, 3-5.

Orchard, J., Marsden, J., Lord, S., Garlick, D., 1997. Preseason Hamstring Muscle Weakness Associated with Hamstring Muscle Injury in Australian Footballers. The American Journal of Sports Medicine 25, 81-85.

Orchard, J., Seward, H., 2002. Epidemiology of injuries in the Australian Football League, seasons 1997-2000. British Journal of Sports Medicine 36, 39-45.

Pappas, G. P., Asakawa, D. S., Delp, S. L., Zajac, F. E., Drace, J. E., 2002. Nonuniform shortening in the biceps brachii during elbow flexion. Journal of Applied Physiology 92, 2381-2389.

Pelc, N. J., Herfkens, R. J., Shimakawa, A., Enzmann, D. R., 1991. Phase Contrast Cine Magnetic Resonance Imaging. Magnetic Resonance Quarterly 7, 229-254.

Pena, E., Calvo, B., Martinez, M. A., Doblare, M., 2006. A three-dimensional finite element analysis of the combined behavior of ligaments and menisci in the healthy human knee joint. Journal of Biomechanics 39, 1686-1701.

Porter, D. A., Heidemann, R. M., 2009. High Resolution Diffusion-Weighted Imaging Using Readout-Segmented Echo-Planar Imaging, Parallel Imaging and a Two-Dimensional Navigator-Based Reacquisition. Magnetic Resonance in Medicine 62, 468-475.

Proske, U., Morgan, D. L., Brockett, C. L., Percival, P., 2004. Identifying athletes at risk of hamstring strains and how to protect them. Clinical and Experimental Pharmacology & Physiology 31, 546-550.

Puso, M. A., Maker, B. N., Ferencz, R. M., Hallquist, J. O., 2007. NIKE3D: A nonlinear, implicit, three-dimensional finite element code for solid and structural mechanics. User's Manual.

Puso, M. A., Maker, B. N., Ferencz, R. M., Hallquist, J. O., 2002. Nike3d: a nonlinear, implicit, three-dimensional finite element code for solid and structural mechanics. UCRL-MA-105268.

Reeder, S., Pineda, A., Wen, Z., Shimakawa, A., Yu, H., Brittain, J., Gold, G., Beaulieu, C., Pelc, N., 2005. Iterative decomposition of water and fat with echo asymmetry and least-squares estimation (IDEAL): Application with fast spin-echo imaging. Magnetic Resonance in Medicine 54, 636-644.

Rehorn, M. R., Blemker, S. S., 2010. The effects of aponeurosis geometry on strain injury susceptibility explored with a 3D muscle model. Journal of Biomechanics 43, 2574-2581.

Rosset, A., Spadola, L., Ratib, O., 2004. OsiriX: An open-source software for navigating in multidimensional DICOM images. Journal of Digital Imaging 17, 205-216.

Salo, A. I. T., Bezodis, I. N., Batterham, A. M., Kerwin, D. G., 2011. Elite Sprinting: Are Athletes Individually Step-Frequency or Step-Length Reliant? Medicine and Science in Sports and Exercise 43, 1055-1062.

Sanfilippo, J. L., Silder, A., Sherry, M. A., Tuite, M. J., Heiderscheit, B. C., 2013. Hamstring strength and morphology progression after return to sport from injury. Medicine and Science in Sports and Exercise 45, 448-54.

Schache, A. G., Ackland, D. C., Laurence, F., Koulouris, G., Pandy, M. G., 2013. Three-dimensional geometry of the human biceps femoris long head measured in vivo using magnetic resonance imaging. Clinical Biomechanics In press.

Schache, A. G., Wrigley, T. V., Baker, R., Pandy, M. G., 2009. Biomechanical response to hamstring muscle strain injury. Gait & Posture 29, 332-338.

Schache, A. G., Blanch, P. D., Dorn, T. W., Brown, N. A. T., Rosemond, D., Pandy, M. G., 2011. Effect of running speed on lower limb joint kinetics. Medicine and Science in Sports and Exercise 43, 1260-1271.

Schache, A. G., Dorn, T. W., Blanch, P. D., Brown, N. A. T., Pandy, M. G., 2012. Mechanics of the human hamstring muscles during sprinting. Medicine and Science in Sports and Exercise 44, 647-658.

Sharafi, B., Ames, E. G., Holmes, J. W., Blemker, S. S., 2011. Strains at the myotendinous junction predicted by a micromechanical model. Journal of Biomechanics 44, 2795-2801.

Sherry, M. A., Best, T. M., 2004. A comparison of 2 rehabilitation programs in the treatment of acute hamstring strains. Journal of Orthopaedic & Sports Physical Therapy 34, 116-125.

Shoepe, T. C., Stelzer, J. E., Garner, D. P., Widrick, J. J., 2003. Functional adaptability of muscle fibers to long-term resistance exercise. Medicine and Science in Sports and Exercise 35, 944-951.

Silder, A., Heiderscheit, B. C., Thelen, D. G., Enright, T., Tuite, M. J., 2008. MR observations of long-term musculotendon remodeling following a hamstring strain injury. Skeletal Radiology 37, 1101-1109.

Silder, A., Reeder, S. B., Thelen, D. G., 2010a. The influence of prior hamstring injury on lengthening muscle tissue mechanics. Journal of Biomechanics 43, 2254-2260.

Silder, A., Thelen, D. G., Heiderscheit, B. C., 2010b. Effects of prior hamstring strain injury on strength, flexibility, and running mechanics. Clinical Biomechanics 25, 681-686.

Silder, A., Westphal, C. J., Thelen, D. G., 2009. A magnetic resonance-compatible loading device for dynamically imaging shortening and lengthening muscle contraction mechanics. Journal of Medical Devices 3, 1-5.

Spottiswoode, B. S., Zhong, X., Hess, A. T., Kramer, C. M., Meintjes, E. M., Mayosi, B. A., Epstein, F. H., 2007. Tracking myocardial motion from cine DENSE images using spatiotemporal phase unwrapping and temporal fitting. IEEE Transactions on Medical Imaging 26, 15-30.

Thelen, D. G., Anderson, F. C., 2006. Using computed muscle control to generate forward dynamic simulations of human walking from experimental data. Journal of Biomechanics 39, 1107-1115.

Thelen, D. G., Chumanov, E. S., Best, T. M., Swanson, S. C., Heiderscheit, B. C., 2005. Simulation of biceps femoris musculotendon mechanics during the swing phase of sprinting. Medicine and Science in Sports and Exercise 37, 1931-1938.

Verrall, G. M., Slavotinek, J. P., Barnes, P. G., Fon, G. T., 2003. Diagnostic and prognostic value of clinical findings in 83 athletes with posterior thigh injury: Comparison of Clinical Findings with Magnetic Resonance Imaging Documentation of Hamstring Muscle Strain. The American Journal of Sports Medicine 31, 969-973.

Verrall, G. M., Slavotinek, J. P., Barnes, P. G., Fon, G. T., Spriggins, A. J., 2001. Clinical risk factors for hamstring muscle strain injury: a prospective study with correlation of injury by magnetic resonance imaging. British Journal of Sports Medicine 35, 435-440.

Ward, S. R., Eng, C. M., Smallwood, L. H., Lieber, R. L., 2009. Are Current Measurements of Lower Extremity Muscle Architecture Accurate? Clinical Orthopaedics and Related Research 467, 1074-1082.

Weiss, J. A., Maker, B. N., Govindjee, S., 1996. Finite element implementation of incompressible, transversely isotropic hyperelasticity. Computer Methods in Applied Mechanics and Engineering 135, 107-128.

Woodley, S. J., Mercer, S., 2005. Hamstring muscles: architecture and innervation. Cells Tissues Organs 179, 125-141.

Woods, C., Hawkins, R., Hulse, M., Hodson, A., 2002. The Football Association Medical Research Programme: an audit of injuries in professional football - analysis of preseason injuries. British Journal of Sports Medicine 36, 436-441.

Woods, C., Hawkins, R. D., Maltby, S., Hulse, M., Thomas, A., Hodson, A., 2004. The Football Association Medical Research Programme: an audit of injuries in professional football--analysis of hamstring injuries. British Journal of Sports Medicine 38, 36-41.

Worrell, T. W., 1994. Factors associated with hamstring injuries. An approach to treatment and preventative measures. Sports Medicine 17, 338-345.

Yu, B., Queen, R. M., Abbey, A. N., Liu, Y., Moorman, C. T., Garrett, W. E., 2008. Hamstring muscle kinematics and activation during overground sprinting. Journal of Biomechanics 41, 3121-3126.

Zajac, F. E., 1989. Muscle and tendon: properties, models, scaling, and application to biomechanics and motor control. Critical Reviews in Biomedical Engineering 17, 359-411.

Zaraiskaya, T., Kumbhare, D., Noseworthy, M. D., 2006. Diffusion tensor imaging in evaluation of human skeletal muscle injury. Journal of Magnetic Resonance Imaging 24, 402-408.

Zerhouni, E. A., Parish, D. M., Rogers, W. J., Yang, A., Shapiro, E. P., 1988. Human heart: tagging with MR imaging--a method for noninvasive assessment of myocardial motion. Radiology 169, 59-63.

Zhong, X., Epstein, F. H., Spottiswoode, B. S., Helm, P. A., Blemker, S. S., 2008. Imaging two-dimensional displacements and strains in skeletal muscle during joint motion by cine DENSE MR. Journal of Biomechanics 41, 532-540.

Zhong, X., Helm, P. A., Epstein, F. H., 2009. Balanced Multipoint Displacement Encoding for DENSE MRI. Magnetic Resonance in Medicine 61, 981-988.

Zhong, X., Spottiswoode, B. S., Meyer, C. H., Kramer, C. M., Epstein, F. H., 2010. Imaging three-dimensional myocardial mechanics using navigator-gated volumetric spiral cine DENSE MRI. Magnetic Resonance in Medicine 64, 1089-1097.